

Observations of wildfire volatile organic compound emissions and urban ozone  
precursors

A Dissertation Presented to  
The Academic Faculty

by

Asher P. Mouat

In Partial Fulfillment  
of the Requirements for the Degree Doctor of Philosophy in Environmental  
Engineering  
School of Civil and Environmental Engineering

Georgia Institute of Technology  
August 2024

Observations of wildfire volatile organic compound emissions and urban ozone precursors

Approved by:

Dr. Jennifer Kaiser, Advisor  
School of Civil and Environmental  
Engineering  
School of Earth and Atmospheric  
Sciences  
*Georgia Institute of Technology*

Dr. Armistead G. Russell  
School of Civil and Environmental  
Engineering  
*Georgia Institute of Technology*

Dr. Greg Huey  
School of Earth and Atmospheric  
Sciences  
*Georgia Institute of Technology*

Dr. Pengfei Liu  
School of Earth and Atmospheric  
Sciences  
*Georgia Institute of Technology*

Dr. Talat Odman  
School of Civil and Environmental  
Engineering  
*Georgia Institute of Technology*

Date Approved: July 19, 2024

*To my mother, the cornerstone upon whom my life has been built.*

## ACKNOWLEDGEMENTS

I pursued this Ph.D. out of an insatiable interest in understanding how our world physically worked coupled with a long-standing, almost innate sense for environmentalism. My time in this program was challenging, but I believe that at every step it has rewarded both these sensibilities. Importantly, the work I've done would not have been possible without the collaboration and support of many people.

First, I want to give special thanks to my advisor, Dr. Jennifer Kaiser, who gave me this research opportunity, and who provided constant, fast, and poignant feedback on my work and was a true driving force in helping me develop as a researcher. As I go forward, I carry with me a certain confidence knowing such a mentor is on my side. I also want to thank all the other members of the Kaiser group for their input and support over the years. Thanks to Nidhi and Aryiana for being consistent sources of humor (I will always appreciate our casual office conversations).

I'd like to extend my gratitude to David Tanner, who was effectively my second mentor and provided a vast wealth of information regarding anything electronic, pneumatic, instrumental or otherwise, and is now someone I consider a friend. I'd also like to thank the COALA-2020 science team, who were a pleasure to work with and gave me so much guidance on my first field campaign.

A special thank you to the members of my committee: Dr. Ted Russell, Dr. Greg Huey, Dr. Pengfei Liu, and Dr. Talat Odman, whose insights and comments have improved the work presented in this thesis.

Finally, I would be remiss to not thank my friends and family who have provided endless support, company, and comfort throughout my Ph.D. Thank you to my mother, my aunts, my uncles, and my grandparents. Special thanks to my grandfather Richard and my uncle Darren, who set me on the path of being an engineer and taught me most of my knowledge about craftsmanship. Thank you to my brother Aidan and late father Ricardo, who set me on the academic path and who I now join as the third doctor in our family. Thank you to my fellow grad school commiserates: Elliot, who entered this program with me, and Dr. Josh Pughe, who I've known since undergrad. Both are close friends, researchers I respect, and motivated me to stay the course. Last, thank you to Colby, Ryan, Al, Natasha, Landon, Will, Paula, Kelly, JC, and all my other beloved friends.

# TABLE OF CONTENTS

ACKNOWLEDGEMENTS.....	iii
LIST OF TABLES.....	viii
LIST OF FIGURES.....	ix
SUMMARY.....	xii
CHAPTER 1: INTRODUCTION	
1.1 Oxidation of volatile organic compounds.....	1
1.2 Using field observations to assess models and satellite retrievals.....	3
CHAPTER 2: OBSERVATIONS OF LONG-LIVED VOLATILE ORGANIC COMPOUNDS FROM THE 2019-2020 AUSTRALIAN WILDFIRES DURING THE COALA CAMPAIGN	
2.1 Introduction.....	8
2.2 Field site and instrument description.....	12
2.2.1 Field site and active fires.....	12
2.2.2 PTR-ToF-MS and supporting observations.....	14
2.3 Observed CO, VOC, and OVOC enhancements.....	15
2.4 Plume origin and transport time.....	20
2.5 O <sub>3</sub> and NO <sub>2</sub> time series.....	22
2.6 Emission factors.....	26
2.6.1 Species selection.....	26
2.6.2 Calculating emission ratios.....	27
2.6.3 Calculating emission factors.....	29
2.7 OH reactivity.....	34
2.8 Conclusions.....	37
CHAPTER 3: EVALUATION OF AERIS MID-INFRARED ABSORPTION, PICARRO CAVITY RINGDOWN SPECTROSCOPY G2307, AND DINITROPHENYLHYDRAZINE- BASED SAMPLING FOR LONG TERM FORMALDEHYDE MONITORING EFFORTS	
3.1 Introduction.....	41
3.2 Instrument description.....	46
3.2.1 Picarro G2307.....	46
3.2.1.1 CRDS operating principles.....	46
3.2.1.2 Determining instrument baseline.....	47
3.2.1.3 Humidity dependence.....	47
3.2.1.4 Data processing.....	49
3.2.1.5 Impact of scrubber choice – DNPH, DR, and DR+MS.....	50
3.2.1.6 Instrument calibration.....	52
3.2.2 Aeris MIRA.....	53
3.2.2.1 MIRA operating principles.....	53

3.2.2.2 Instrument baseline.....	54
3.2.2.3 Impact of scrubber choice – heated HO and DNPH for Aeris MIRA.....	55
3.2.2.4 Data processing.....	56
3.2.2.5 Instrument calibration.....	56
3.2.3 DNPH (TO-11A).....	59
3.3 Instrument precision and baseline drift.....	61
3.4 Intercomparison.....	65
3.4.1 Field site descriptions.....	65
3.4.1.1 South DeKalb.....	65
3.4.1.2 Georgia Tech.....	67
3.4.2 Instrument intercomparisons.....	68
3.4.2.1 Continuous HCHO monitor comparison.....	68
3.4.2.2 Picarro G2307 and TO-11A DNPH comparison.....	70
3.5 Suitability for long-term deployment.....	72
3.6 Conclusions.....	77
<b>CHAPTER 4: INFORMING NEAR-AIRPORT- SATELLITE NO<sub>2</sub> RETRIEVALS USING PANDORA SKY-SCANNING OBSERVATIONS</b>	
4.1 Introduction.....	79
4.2 Materials and methods.....	83
4.2.1 Pandora observations.....	83
4.2.2 TROPOMI retrievals.....	87
4.2.3 AMFs from GEOS-CF and fused GEOS-CF/Pandora profiles.....	88
4.2.4 Pandora DS troposphere/stratosphere separation.....	91
4.2.5 Pandora-TROPOMI comparison approach.....	92
4.2.6 Separation of high and low travel periods.....	93
4.3 Results and discussion.....	96
4.3.1 NO <sub>2</sub> VCD variability.....	96
4.3.2 Impact of Pandora viewing geometry on sky columns.....	99
4.3.3 Impact of aviation on NO <sub>2</sub> tropospheric VCDs and vertical profiles.....	102
4.3.4 TROPOMI NO <sub>2</sub> tropospheric VCDs: impact of modeled and fused AMF.....	106
4.3.5 Implications.....	112
<b>CHAPTER 5: SUMMARY AND FUTURE WORK</b>	
5.1 Summary of current work.....	115
5.2 Future directions.....	119
<b>APPENDIX A: SUPPORTING INFORMATION FOR CHAPTER 2</b>	
A.1 Supplemental information for PTR-ToF-MS and supporting observations.....	122
A.2 Supplemental analysis of plume origin and transport time.....	125
A.3 Supplemental information for emission ratios.....	132
A.4 Supplementary analysis of emission factors.....	134

APPENDIX B: SUPPORTING INFORMATION FOR CHAPTER 4

B.1 Comparison with California airport NO <sub>2</sub> vertical profiles.....	140
BIBLIOGRAPHY.....	143

## LIST OF TABLES

<b>Table 2.1</b>	Emission factors from Australian and U.S.-based wildfire studies.....	31
<b>Table A.1</b>	Standards used to calibrate PTR-ToF-MS, to determine instrument transmission, and limits of detection.....	122
<b>Table A.2</b>	All species in calibration standards or for which an emission factor was derived and their respective uncertainties.....	124
<b>Table A.3</b>	Emission ratios derived from averaging over nighttime wildfire plume sampling period.....	133
<b>Table A.4</b>	Emission factors from Australian, U.S.-based, and globally averages for temperate biomes.....	138

## LIST OF FIGURES

<b>Figure 2.1</b>	Active fires from 1-5 Feb 2020 and their proximity to the COALA-2020 field site with HYSPLIT back-trajectories.....	13
<b>Figure 2.2</b>	Wildfire VOCs and CO time series on 3 – 4 Feb 2020.....	18
<b>Figure 2.3</b>	Product-to-reactant ratio time series for furan oxidation products.....	19
<b>Figure 2.4</b>	Time series for O <sub>3</sub> , NO <sub>2</sub> , CO, and wind direction.....	23
<b>Figure 2.5</b>	Example emission ratio analysis using acrolein.....	28
<b>Figure 2.6</b>	OH reactivity time series.....	36
<b>Figure 3.1</b>	Picarro G2307 HCHO concentrations as a function of measured H <sub>2</sub> O concentrations.....	49
<b>Figure 3.2</b>	Picarro G2307 baselines determined using the DR, DR+MS, or DNPH scrubbing methods.....	51
<b>Figure 3.3</b>	Aeris standard addition calibrations.....	58
<b>Figure 3.4</b>	Allan-Werle curves for Picarro G2307, Aeris Ultra and Aeris Pico instruments...	62
<b>Figure 3.5</b>	Instrument baseline time series for Picarro G2307, Aeris Ultra and Aeris Pico....	64
<b>Figure 3.6</b>	Field site locations of HCHO instruments in Atlanta, GA.....	66
<b>Figure 3.7</b>	Intercomparison deployment configurations of HCHO instruments.....	67
<b>Figure 3.8</b>	Ambient observation intercomparison of three HCHO monitors.....	69
<b>Figure 3.9</b>	8 h TO-11A DNPH observations compared to Picarro G2307 observations.....	71
<b>Figure 3.10</b>	1 h averaged ambient HCHO time series from Picarro G2307, Aeris Ultra, and Aeris Pico from Aug. 2022 through Jan 2023.....	73

<b>Figure 3.11</b>	HCHO concentrations from 1999 and 2022.....	75
<b>Figure 4.1</b>	Pandora DS and sky scanning azimuth viewing directions.....	85
<b>Figure 4.2</b>	Example of vertical profiles measured over the ATL runways on 22 Mar 2021....	91
<b>Figure 4.3</b>	Time series of daily departures from ATL.....	95
<b>Figure 4.4</b>	TROPOMI tropospheric NO <sub>2</sub> VCDs for periods of low and high aircraft departures from ATL.....	96
<b>Figure 4.5</b>	DS and TROPOMI tropospheric NO <sub>2</sub> VCDs for the full deployment period.....	97
<b>Figure 4.6</b>	Correlation and regression of DS and tropospheric VCDs from entire deployment period.....	100
<b>Figure 4.7</b>	Midday enhancement of Pandora sky VCDs over the ATL terminal as a function of windspeed and wind direction.....	102
<b>Figure 4.8</b>	Median modeled and observed NO <sub>2</sub> profiles for periods of low and high air traffic.....	104
<b>Figure 4.9</b>	Ratio of AMFs calculated from fused and GEOS-CF vertical profiles for each Pandora viewing direction.....	108
<b>Figure 4.10</b>	Correlation plot of TROPOMI (AMF <sub>GEOS-CF</sub> and AMF <sub>Fused</sub> ) and Pandora DS NO <sub>2</sub> tropospheric VCDs.....	110
<b>Figure 4.11</b>	Hourly averaged Pandora sky VCDs overlooking background or ATL runways during periods of low and high aviation.....	111
<b>Figure A.1</b>	Altitudes corresponding by color to trajectories plotted in Figure 2.1.....	126
<b>Figure A.2</b>	HYSPLIT forward trajectories for the fire cluster to the south of Canberra, AU.....	127
<b>Figure A.3</b>	HYSPLIT forward trajectories for southern fire cluster in the southeast corner of the Australia.....	128

<b>Figure A.4</b>	NASA Worldview imagery with fire counts from Suomi VIIRS satellite imaging.....	129
<b>Figure A.5</b>	Averaged wind speed for the fire clusters in the southeast corner of Australia....	130
<b>Figure A.6</b>	Daily total precipitation for New South Wales, AU averaged over the month of January 2020.....	131
<b>Figure A.7</b>	Comparison of emission ratios derived from period D and from average of all periods.....	132
<b>Figure A.8</b>	Emission factors from Table 2.1 displayed in scatter plot.....	134
<b>Figure A.9</b>	Comparison of emission factors to lab-based emission factors.....	135
<b>Figure A.10</b>	Emission factors from Australian-based, U.S.-based, and global averages.....	138
<b>Figure B.1</b>	Pandora and aircraft NO <sub>2</sub> vertical profiles at ATL, LAX, and SBA airports.....	141

## SUMMARY

Anthropogenic emissions have and continue to degrade air quality and alter chemical regimes in the atmosphere. Emissions of greenhouse gases have increased global temperatures, contributed to increasingly arid conditions, and exacerbated wildfire seasonal lengths and intensities. Wildfires emit a wide array of carcinogenic, highly reactive volatile organic compounds (VOCs). Urban emissions of oxides of nitrogen leads to the formation of secondary pollutants like ozone and organic aerosols. Prediction and mitigation of pollution events requires the understanding of complex VOC oxidation pathways. This work employs ground observations to further constrain VOC emissions from wildfires, assess the accuracy of ground-monitoring network HCHO measurements and determine temporal changes in urban HCHO concentrations, and evaluate the accuracy of satellite products when monitoring NO<sub>2</sub> over airports.

We use measurements from a proton transfer reaction time-of-flight mass spectrometer to develop emission factors (EFs) for 15 species for an understudied temperate forest biome in New South Wales, Australia. We conclude that EFs are applicable across geographically different but analogous biomes for modeling purposes. We then evaluate the precision and accuracy of three fast measurement, in-situ HCHO monitors and compare with observations from the TO-11A methodology at a photochemical assessment monitoring station in Atlanta. We find that TO-11A measurements are biased low, and that decreases in HCHO concentrations since 1999 are small. Finally, we use NO<sub>2</sub> vertical profile measurements from a Pandora spectrometer and profile estimates from chemistry transport model to recalculate satellite retrievals. We find the recalculated quantities are biased low relative to independent ground observations.

# CHAPTER 1

## INTRODUCTION

### 1.1 Oxidation of volatile organic compounds

The atmosphere is a complex and globally interconnected part of our environment. Industrialization and urbanization have and continue to produce anthropogenic emissions that lead to the degradation of air quality, are detrimental to human health, and progressively alter atmospheric composition. These emissions are comprised of particulate- and various gas-phase constituents like volatile organic compounds (VOCs), oxides of nitrogen ( $\text{NO}_x = \text{NO} + \text{NO}_2$ ), carbon monoxide and dioxide (CO and  $\text{CO}_2$ ), methane ( $\text{CH}_4$ ), and more. They result from evaporation and combustion of fossil fuels, factory processes like those using paints or solvents, or human activities like the burning of biomass. CO,  $\text{CO}_2$ , and  $\text{CH}_4$  are the greenhouse gases (GHGs) primarily responsible for the warming of the earth. VOCs are a class of gas species that have anthropogenic (AVOC) and biogenic (BVOC) origins and exhibit varying degrees of carcinogenicity and reactivity. BVOC emissions comprise the majority of total global VOC emissions for which the most prominent species by mass is isoprene (Wennberg et al., 2018). Their emissions are from the biosphere (e.g. plants and trees).

Emissions from wildfires also constitute a significant biogenic source of VOCs, GHGs, and  $\text{NO}_x$  (Knorr et al., 2016; Sekimoto et al., 2018; Bray et al., 2021). Wildfire smoke affects atmospheric composition from local to global scales as well as the radiative balance of the earth (Chang et al., 2021). The seasonal length and intensity of wildfires has increased globally (Jones

et al., 2022). This is typically attributed to climate warming, spurred on by anthropogenic emissions of GHGs, leading to more arid conditions and is predicted to increase in the future (Abatzglou et al. 2019). Chemical speciation of wildfire smoke has revealed chemically complex profiles composed of hundreds of biomass burning VOCs (BBVOCs) largely composed of alkanes, alkenes, aromatics, carbonyls, phenols, and oxygenates (Hatch et al., 2015; Koss et al., 2018a; Sekimoto et al., 2018).

VOCs are an integral part of the chemistry governing the troposphere and lead to the formation of pollutants like secondary organic aerosols (SOA) and ozone ( $O_3$ ) when oxidized (Jaffe and Wigder, 2012; He et al., 2024). These pollutants are of particular interest to researchers and policymakers as exposure causes respiratory and cardiovascular distress and increases the rate of premature mortalities.

As SOA and  $O_3$  are secondarily formed, their concentrations are primarily dependent on the emissions of  $NO_x$  and VOCs. The pathways that govern how VOC oxidation reactions proceed, and subsequently the products that are formed, are determined largely by local  $NO_x$  concentrations. While  $NO_x$  has its biogenic sources (lightning, soil nitrification processes, and biomass burning), the majority of it is emitted from anthropogenic activities (vehicle emissions and fossil fuel combustion) (Lamsal et al., 2011). Urban areas then have higher  $NO_x$  concentrations.  $O_3$  achieves its highest concentrations in populous urban centers making its mitigation of significant importance. Oxidation of VOCs almost ubiquitously leads to the formation of formaldehyde (HCHO), which is chemically important as it can be used as a proxy for total VOC and OH concentration, and ratios of HCHO-to- $NO_2$  can be used to assess  $O_3$

production sensitivity to changes in VOCs and NO<sub>x</sub> (Palmer et al., 2006; Zhu et al., 2017a; Wolfe et al., 2019). Furthermore, photolysis and oxidation of HCHO are significant sources of HO<sub>x</sub> (= OH + HO<sub>2</sub>) radicals, which are the dominant atmospheric oxidants in the daytime. Enhancing production of HCHO can then further propagate oxidative chemistry. Oxidized VOCs generally have lower volatility and more readily partition into SOA.

Implementing controls on NO<sub>x</sub> emissions then influences the secondary production of tropospheric pollutants. O<sub>3</sub> production has a complicated, non-linear response to changes in NO<sub>x</sub> concentration. Prediction and mitigation of pollutant formation requires understanding atmospheric composition and the mechanisms governing VOC oxidation.

## **1.2 Using field observations to assess models and satellite retrievals**

Determining atmospheric composition and verifying our understanding of VOC oxidation requires field observations. To this end, sophisticated networks of ground monitors, retrievals from satellites, and collaborative campaigns taking chemically comprehensive measurements have been devised. Ideally, observations have high precision and accuracy, fine spatiotemporal resolution, cover large areas, and consume few resources. However, this historically has not been possible. Field measurements frequently exhibit high precision, accuracy, and time resolution but are spatially limited. Chemically comprehensive VOC measurements are typically resource intensive as well.

Chemical transport models (CTM) are effectively simplifications of atmospheric processes that provide spatially and temporally complete estimates of pollutant and VOC concentrations. They are computational simulations and have been developed by combining observations with our assumptions of atmospheric chemistry. Models can provide insight as to where our hypotheses are inaccurate.

Satellite instruments provide retrievals for myriad gas and particulate phase variables (e.g. O<sub>3</sub>, NO<sub>2</sub>, HCHO, aerosol optical thickness) with high spatial resolution and land coverage but have historically been limited in their temporal resolution. Instruments like the Tropospheric Ozone Monitoring Instrument (TROPOMI) chart a sun-synchronous orbit, providing observations once a day. The recently launched Tropospheric Emissions: Monitoring of Pollution (TEMPO) instrument has a geostationary orbit and will provide hourly observations. However, satellite instruments utilize back-scattered solar radiation for measurements and are limited to daytime observations.

CTMs and satellite products can fill spatial or temporal gaps that observations may lack, which can occur even in areas with dense ground networks. However, both exhibit biases and require validation through comparisons with field observations. Models, retrievals, and field observations can be synergistically combined to overcome their respective limitations. Their fusion may allow for the monitoring of pollutants at finer spatiotemporal resolution and with greater accuracy and precision than that of each individual method. The objective of this thesis is to utilize ground-based observations for the improvement of existing model and ground network

infrastructures and to explore how these observations can be used to complement satellite and CTM products for future research efforts.

In chapter 2, we use measurements from a proton transfer reaction time-of-flight mass spectrometer (PTR-ToF-MS) to develop emission factors (EFs) for 15 VOCs for a temperate forest biome in New South Wales, Australia and quantify smoke-related OH reactivity. Chemical profiles of wildfire smoke vary greatly in speciation and emission. This variability is typically attributed to combustion phase and fuel characteristics (Hatch et al. 2015, Sekimoto et al. 2018). Australia is understudied with only two previous studies reporting VOC EFs (Lawson et al., 2015, Guerette et al., 2018). After comparing EFs with those from Australian-based, U.S.-based, and global studies, we suggest that EFs can be used across analogous biomes and that plume sampling approach may significantly affect inter-study EF agreement.

As the smoke plume sampled in this work was transported overnight, we use a child-to-parent ratio of furan and its  $\text{NO}_3$ -oxidation products as a nighttime chemical age marker. Nighttime oxidation of wildfire plumes is relatively understudied (Decker et al., 2019, Kodros et al., 2020). We show that the chemically youngest portion of the smoke plume coincides with the shortest HYSPLIT trajectories when the plume travelled entirely in the night giving confidence to this age marker.

Last, the chemical evolution of transported plumes is complex. Depending on the atmospheric regime and chemical age,  $\text{NO}_x$ -availability and subsequently  $\text{O}_3$  concentrations are highly variable (Jaffe and Widger, 2012, Liang et al., 2022). We use  $\text{NO}_x$ ,  $\text{O}_3$ , and maleic

anhydride time series to assess the  $\text{NO}_x$  regime and determine the excess  $\text{O}_3$  concentration from the smoke plume. We find that maleic anhydride and  $\text{NO}_2$  produce an anti-correlation which is opposite of the trend reported in Liang et al. (2022) and attribute this to the difference in settings (forest versus city). We determine a 5.5 ppb increase in  $\text{O}_3$  over the daytime average.

In chapter 3, we focus on three commercially new, fast measurement, in situ instruments (Aeris Ultra, Aeris Pico, and the Picarro G2307) to demonstrate the advantages they offer over the TO-11A sampling technique, which the U.S. Environmental Protection Agency employs in their ground-networks for HCHO monitoring. HCHO exists in trace amounts, has a short lifetime, a heterogenous spatial distribution, and exhibits significant diurnal variability (Zhu et al., 2017, Wang et al., 2022). The TO-11A sampling methodology has low temporal resolution (hours-scale) and known biases dependent on relative humidity (Ho et al., 2014).

We devise an optimal deployment strategy for each instrument, specifically focusing on mitigating known humidity dependencies (Shutter et al. 2019, Glowania et al., 2021). We quantify their respective accuracies and precisions, and intercompare their ambient measurements over a one-year deployment period in Atlanta, GA, finding that these monitors provide sufficiently high-quality observations and are robust to seasonal ambient conditions. We compare observations from the Picarro G2307 with those from the TO-11A method and determine the relative decrease in HCHO concentration between 1999 and 2022 in the metropolitan area. TO-11A measurements were biased low by 52 % relative to the Picarro G2307, which is the largest disparity reported in literature. TO-11A HCHO observations exhibit

a 53% decrease in southeast Atlanta from 1999 to 2022, but Picarro G2307 observations indicate only a 2 % decrease.

In chapter 4, we evaluate the accuracy of NO<sub>2</sub> retrievals from TROPOMI over the Hartsfield-Jackson International airport (ATL) using tropospheric vertical column density (VCD) and profile observations from a Pandora spectrometer. Airports appear as “hot-spots” in satellite measurements (Judd et al., 2019) and aviation-related NO<sub>2</sub> emissions are anticipated to increase in the future (ICAO, 2019). Airports are officially unmonitored, but satellite retrievals may offer the means for long-term tracking of NO<sub>2</sub> VCDs. Satellite retrievals exhibit biases when measuring in polluted areas (Judd et al., 2019, Judd, et al., 2020, Verhoeslt et al., 2021, Goldberg et al., 2022). This is often attributed to the coarse resolution of CTMs used to generate a priori vertical profiles for air mass factors (AMF). We recalculate AMFs using vertical profiles from the Global Earth Observing System Compositional Forecasts (AMF<sub>GEOS-CF</sub>) and a model/measurement fusion approach (AMF<sub>Fused</sub>) and evaluate TROPOMI VCDs.

Observed profiles show a higher mixing height than GEOS-CF estimates, suggesting meteorology as a source of uncertainty in future retrievals. Additionally, near-surface NO<sub>2</sub> is greatest from 07:00-11:00 LT, indicating that TROPOMI-based NO<sub>2</sub> estimates likely underpredict absolute emissions and that future satellite-based observations during this time may more clearly reflect the impact of aviation on near-airport emissions. We find that the new TROPOMI VCDs are biased low by -22% (AMF<sub>GEOS-CF</sub>) to -29 % (AMF<sub>Fused</sub>) relative to Pandora ground observations. Results from this work indicate the ability to improve satellite retrieval accuracy by combining observed and modeled vertical profiles.

## CHAPTER 2

### OBSERVATIONS OF LONG-LIVED VOLATILE ORGANIC COMPOUNDS FROM THE 2019-2020 AUSTRALIAN WILDFIRES DURING THE COALA CAMPAIGN

#### 2.1 Introduction

Wildfire smoke significantly affects atmospheric composition, chemistry, human health, and radiative balance (Yokelson et al., 2008; Akagi et al., 2011a; Ford et al., 2018; Wentworth et al., 2018; Andreae, 2019; Sokolik et al., 2019; Macsween et al., 2020). Wildfire season duration and intensity are predicted to increase in the future, suggesting a growing influence of biomass burning in coming decades (Fairman et al., 2015; Donovan et al., 2017; Abatzoglou et al., 2019). Volatile organic compounds (VOCs) emitted from biomass burning (BBVOCs) are directly harmful to human health and can contribute to the formation of ozone and secondary organic aerosol (SOA) (Akagi et al., 2012; Keywood et al., 2013; Lawson et al., 2015a; Sekimoto et al., 2017). Predictions of BBVOC emissions are complicated by the complexity of combustion and fuel characteristics, and model parametrizations are based on a limited number of field observations (Hatch et al., 2015; Sekimoto et al., 2018).

Australia wildfires emit 7 %–8% of global biomass burning emissions, producing more volatilized carbon than the United States and Europe, with smoke plumes significantly influencing local and even global air quality (Ito and Penner, 2004; Van Der Werf et al., 2010; Keywood et al., 2013; Lawson et al., 2015a). In 2019–2020, Australia experienced its worst wildfire season on record with an estimated 19 million hectares of land destroyed (Filkov et al.,

2020). This particular season is now colloquially known as the Black Summer, due to its prolonged intensity and length (October 2019–February 2020). Many of Australia’s major cities were blanketed in smoke for weeks at a time, leading to long term exposure to excessive concentrations of harmful atmospheric compounds (Borchers Arriagada et al., 2020). These fires predominantly affected the temperate forests of the state of New South Wales (NSW), burning the largest land area of anywhere in the country (Davey and Sarre, 2020). Despite the impact on atmospheric composition from Australian fires, its biomes remain understudied, particularly these same NSW forests (Lawson et al., 2015a). Given the complexity and variability in biomass burning scenarios and the use of emission factors (EFs, in units of kilograms of VOC emitted per kilogram fuel burnt) to inform air quality models, this can lead to issues in effectively constraining emissions. For example, Lawson et al. (2017) reported a strongly non-linear response in simulated ozone ( $O_3$ ) when varying biomass burning (BB) EFs, showing the resulting sensitivity from chemical transport models (CTMs). This sparseness of measurements leads to the use of North American EFs (such as those from Akagi et al. (2011b) or Burling et al. (2011)) to inform CTMs, simulating emissions of geographically separate biomes. Even among similar biomes (for instance, the temperate forests of the US), fuel types differ and thus can influence the speciation of VOCs emitted (Hatch et al., 2017; Guérette et al., 2018a; Coggon et al., 2021). Further evidence of this is found in a study by Guérette et al. (2018a) showing that EFs of some VOCs (e.g., formic acid, ethane, monoterpenes, acetonitrile) can be 3–5 times higher than those measured in the US, and attributing this to fuel type.

A complicating factor in deriving EFs from field observations is accounting for the influence of chemical processing. EFs are ideally based on observations close to the fire. When

this is not possible, indicators of plume chemical age, such as oxidized VOC (OVOC) to VOC ratios, can be used to diagnose the relative age of a plume. During the day, downwind VOC concentrations are primarily influenced by OH-initiated oxidation. At night, NO<sub>3</sub>-initiated oxidation can significantly influence observed VOC concentrations (Kodros et al., 2020; Decker et al., 2021). There are several methods in existence for assessing daytime oxidation, but fewer are known for the night (Liu et al., 2016; De Gouw et al., 2018; Wentworth et al., 2018; Decker et al., 2021). In this work, we use the maleic anhydride-to-furan ratio introduced in Gkatzelis et al. (2024) to assess OH oxidation. We examine the use of a new OVOC=VOC ratio, cis-2-butenediol/furanone-to-furan, as an indicator of nighttime oxidation.

To further assess the effects of nighttime transport on biomass burning emissions, we look at the magnitude of OH reactivity measured that results from the compounds which most substantially contribute to it and determine the relative contributions of the resulting chemical groups. Certain categories of BBVOCs like furans or phenols, which are emitted in the combustion process, are important as they enhance OH reactivity and resultingly have high O<sub>3</sub> and SOA forming potential, and are considered to be understudied (Gilman et al., 2015; Hatch et al., 2017). Most wildfire studies are conducted during the daytime, with plume oxidation focused on interactions with the OH radical and O<sub>3</sub> (Liu et al., 2016; Palm et al., 2020; Coggon et al., 2021; Decker et al., 2021; Permar et al., 2021a). However, the plume studied here spent a significant amount of time transported under nighttime conditions.

Additionally, we use time series to observe chemical trends in ozone (O<sub>3</sub>) and nitrogen dioxide (NO<sub>2</sub>) as their emissions and chemical behavior are intimately linked with biomass

burning chemistry. O<sub>3</sub> production in wildfire plumes is contingent on initial emissions, local environment, and atmospheric processing during transportation. Wildfire plumes emit significant precursors of O<sub>3</sub>, but there is not a general consensus towards generation or depletion, with various campaigns reporting measurements in either case, especially in the instance of processed, downwind plumes (Verma et al., 2009; Alvarado et al., 2010; Jaffe and Wigder, 2012; Lawson et al., 2015a; Brey and Fischer, 2016; Müller et al., 2016). NO<sub>2</sub> is emitted during the combustion process and has a nonlinear relationship to O<sub>3</sub> production via reactions with these VOC precursors. However, the NO<sub>2</sub> radical has additional chemical pathways with OH, NO<sub>3</sub>, and phenolic compounds leading to a general NO<sub>x</sub>-limited regime (Jaffe and Wigder, 2012; Robinson et al., 2021; Liang et al., 2022). Furthermore, there are again fewer observations for the effect of nighttime oxidation processes on O<sub>3</sub> production with a recent modeling study conducted by Decker et al. (2019). O<sub>3</sub> production in wildfire smoke remains a significant source of uncertainty in its contribution to the tropospheric O<sub>3</sub> budget (Jaffe and Wigder, 2012; Young et al., 2018; Xu et al., 2021).

Here, we use observations from a proton-transfer-reaction time-of-flight mass spectrometer (PTR-ToF-MS) during the 2019–2020 Australian wildfire season to derive EFs of 15 compounds, including 6 compounds for which there are no previous observations. We examine a subset of smoke influenced nighttime observations made by a PTR-ToF-MS during the COALA-2020 field campaign. NO<sub>3</sub>-initiated oxidation dominated the chemical processing late in the night, as the plume traveled 8 h to the field site from large, highly active fires to the south. We also use co-located Fourier transform infrared (FTIR) measurements of CO<sub>2</sub>, CO and CH<sub>4</sub> to derive these EFs for nighttime longer-lived VOCs (BB<sub>VOC+NO<sub>3</sub></sub> average transport time).

We compare these results with five related studies, two focused on Australian temperate forests, two focused on US temperate forests, and one reporting EFs used to represent temperate biomes across the globe. We find generally good agreement across several of these studies and discuss potential reasons for discrepancies seen in EFs for selected compounds.

## **2.2 Field site and instrument description**

### **2.2.1 Field site and active fires**

The COALA-2020 field site was located in Cataract Scout Park (34.247° S, 150.825° E) at 400 m above sea level, 15 km inland, and 30 km to the northwest of the nearest urban area (Wollongong, NSW). Figure 2.1 shows the field site relative to the fires active during 1-5 Feb 2020. We use the Suomi VIIRS thermal anomalies product, filtering for points at high confidence levels to avoid counting any reflective false positives from plains or urban centers. Also plotted is the normalized difference vegetative index (NDVI) which is determined from measurements aboard the MODIS Terra satellite (Didan, 2021). The fires are primarily located in temperate forests along the southeastern coast, with a small inland group near Canberra. These forests consist of open, tall woodlands made up of Eucalyptus species grouped generally as dry sclerophyll.

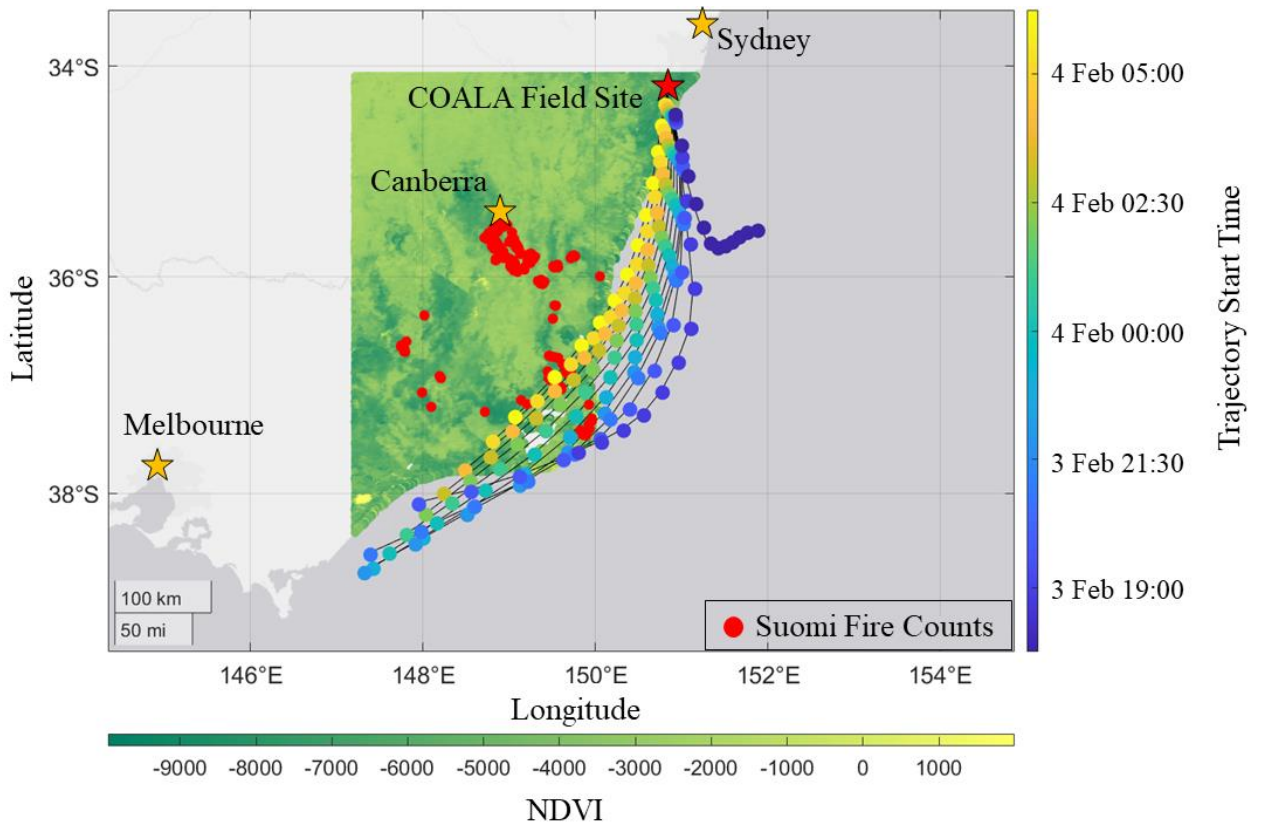


**Figure 2.1** Active fires from 1-5 Feb 2020 and their proximity to the COALA-2020 field site.

NDVI is plotted at 250 m resolution from the MOD13A1 dataset acquired by measurements via the MODIS Terra satellite. Pixels have been filtered to contain cloud coverage less than 30% and VI Usefulness bits indicating top two tiers of data quality. Fire counts are plotted using the VNP14IMGTDL\_NRT data from Suomi VIIRS satellite imaging overlaid with HYSPLIT back trajectories. Each tail represents a trajectory 12 h prior to reaching the site and is colored by its starting time. Circles indicate 1 h intervals moving backwards from the start time.

### 2.2.2 PTR-ToF-MS and supporting observations

VOCs were measured using an Ionicon PTR-ToF-MS 4000 which operated with a mass resolution between 2000-3000 FWHM  $m/\Delta m$  and at a mass range spanning  $m/z = 18-256$ . The drift tube was held at a temperature of  $70^\circ\text{C}$ , pressure at 2.60 mbar, and an  $E/N = 120\text{ Td}$  (electric field to molecular number density ratio). The instrument was housed in a climate-controlled unit, connected to a 15 m long PTFE insulated line (0.635 cm OD) attached to a 10 m tall mast, placing inlet height 0.5 m above the canopy height. Sample flowed through the inlet at 3 SLPM for a residence time of 2.5 s. Peak separation of 1 min averaged spectra was conducted in Ionicon's PTR-Viewer 3 software.

Calibrations were performed using two VOC cylinders designed by Airgas on 31 Jan 2020, three days before measuring the smoke event discussed here. A second calibration was performed in the following week with little change in instrument sensitivity. The cylinders contained 17 compounds spanning a mass range of 33-154 Da and are shown in Table A.1. Many of these compounds are reported in the final EFs list – methanol, acetonitrile, acetaldehyde, acrolein, acetone, MVK+MACR, benzene, C<sub>8</sub>- and C<sub>9</sub>-aromatics. All compounds used either do not fragment under these drift tube conditions or have known fragmentary peaks. Instrument zeros were determined using ultra-zero air. Limits of detection ( $3\sigma$ ) for calibrated species are also given in Table A.1 and range between 5-165 ppt. The raw counts per second (cps) were corrected for instrument transmission, which was determined using a subset of the species in the calibration standards. Corrected cps (ccps) are then normalized to the reagent ion signal ( $\text{H}_3\text{O}^+$  ccps  $\times 10^6$ , ncps) using the methodology described by Sekimoto et al. (2017). For compounds of

interest not included in the calibration standards, sensitivity was determined using the method described in Sekimoto et al. (2017), which yields uncertainties at 100 %. Table A.2 shows all compounds presented in this study alongside whether they were included in the calibration standards and their respective uncertainty.

In addition to the PTR-ToF-MS measurements, we use observations of CO, CO<sub>2</sub>, and CH<sub>4</sub> obtained from the collocated FTIR system. Information of this instrument and its setup is provided in Griffith et al. (2012).

### **2.3 Observed CO, VOC, and OVOC enhancements**

Figure 2.2 shows the observations of CO and VOCs during a smoky period on 3 – 4 Feb 2020. CO and acetonitrile – long-lived tracers associated with wildfires (Coggon et al., 2016) – were used to identify the total period of time during which observations were impacted by smoke. Enhancements in both species started at 17:30 local time on 3 Feb and lasted until 19:00 on 4 Feb, when wind direction shifted.

We used furan, a short-lived smoke tracer, and its oxidation products to determine which periods of the smoke event represent the least oxidized plume. Furan is highly reactive with OH ( $k_{\text{furan}+\text{OH}} = 4.04 \times 10^{-11} \text{ cm}^3 \text{ molec}^{-1} \text{ s}^{-1}$  at 298 K and 1 atm) and NO<sub>3</sub> ( $k_{\text{furan}+\text{NO}_3} = 1.36 \times 10^{-12} \text{ cm}^3 \text{ molec}^{-1} \text{ s}^{-1}$  at 298 K and 1 atm). OH-initiated oxidation produces maleic anhydride (C<sub>4</sub>H<sub>2</sub>O<sub>3</sub>), which has little or no direct emissions from wildfires and low reactivity with both OH

and  $\text{NO}_3$ .  $\tau_{\text{C}_4\text{H}_2\text{O}_3+\text{OH}}$  and  $\tau_{\text{C}_4\text{H}_2\text{O}_3+\text{NO}_3}$  were determined to be 3.99 days and 1.42 days, respectively, assuming  $[\text{OH}]_{\text{Avg}} = 2 \times 10^6 \text{ molec cm}^{-3}$  and  $[\text{NO}_3]_{\text{Avg}} = 8 \times 10^7 \text{ molec cm}^{-3}$  (O'dell et al., 2020). Reaction rate constants were taken from two studies (Grosjean and Williams II, 1992; Bierbach et al., 1994). The ratio of maleic anhydride-to-furan therefore provides a relative measure of the plume photochemical age. Using aircraft-based observations of wildfire plumes in the Western US, Gkatzelis et al. (2024) determined the photochemical age of plumes with maleic anhydride-to-furan ratios below 0.13 to be  $\leq 2 \text{ h}$ .

Nighttime in-plume furan oxidation is dominated by  $\text{NO}_3$ , with contributions from  $\text{O}_3$  (Decker et al., 2019). While many BBVOCs are highly reactive with  $\text{NO}_3$ , there is less research on indicators of  $\text{NO}_3$  oxidation. Decker et al. (2019) track  $\text{NO}_3$  chemistry using the ratio of total reactive nitrogen ( $\text{NO}_y$ ) to  $\text{NO}_x$ , and Kodros et al. (2020) examined  $\text{NO}_3$ -reacted products such as nitrocatechol and nitrophenol of phenolic compounds (e.g. phenol, catechol, cresol).  $\text{NO}_y$  was not measured during this field campaign, and measurements of  $\text{NO}_3$ -oxidized phenols were highly uncertain as they fragmented given the high E/N the PTR-ToF-MS operated with. We therefore examined a new indicator of  $\text{NO}_3$  oxidation using furan's dominant  $\text{NO}_3$  products – cis-2-butenediol and furanone (Berndt et al., 1997). Both products are relatively long lived, with lifetimes estimated at  $\tau_{\text{cis-2-butenediol}+\text{NO}_3} = 9 \text{ days}$  and  $\tau_{\text{furanone}+\text{NO}_3} = 8 \text{ h}$ . Lab based studies and field campaigns conducted in the US and Australia suggest that furan and furanone EFs are comparable with study-averaged values for furan ranging from  $0.132 - 0.51 \text{ g kg}^{-1}$  and  $0.27 - 0.57$  for furanone (Akagi et al., 2011a; Hatch et al., 2015; Stockwell et al., 2015a; Selimovic et al., 2018; Liu et al., 2017a; Koss et al., 2018a; Andreae, 2019; Prichard et al., 2020; Permar et al., 2021a; Gkatzelis et al., 2024). No furan EFs have been reported for Australian temperate

forests and only one furanone EF is reported from Lawson et al. (2015) at a comparable value of  $0.57 \text{ g kg}^{-1}$ . Additionally, emissions modeled in Decker et al. (2019) from wildfires suggest that furan and furanone are emitted in roughly equal proportions. As such, we operate not on the assumption of negligible OVOC emissions, but that variability in OVOC/VOC ratios are driven by chemical aging.

Figure 2.2 shows furan enhancements, which begin later on 3 Feb than enhancements of acetonitrile, maleic anhydride, and furanone/cis-2-butenediol (which are both measured at  $m/z$  85 and from here on are identified as such), indicating a less oxidized plume was being sampled. Maleic anhydride concentrations are high during the initial period of the smoke event, suggesting significant OH-initiated processing throughout the day before the plume reached the site. After sunrise on 4 Feb, furan decays faster than CO, and maleic anhydride concentrations begin to rise, indicating the OH-oxidation of furan. Enhancements in  $m/z$  85 are seen when the smoke arrives and vary throughout the night.

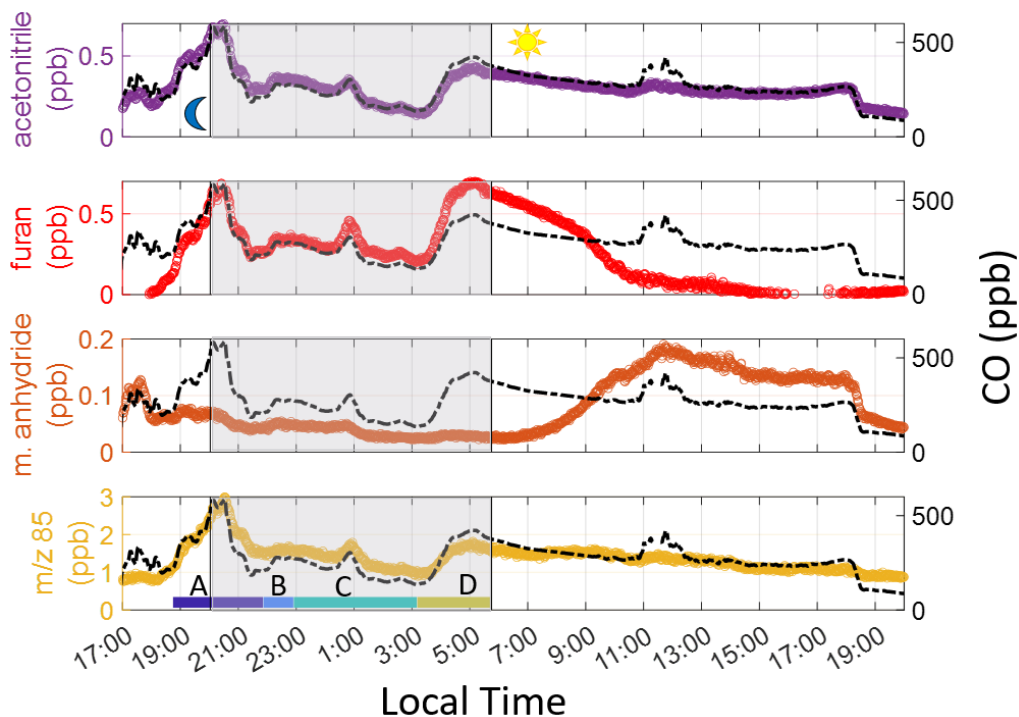


**Figure 2.2** VOCs and CO on 3 – 4 Feb 2020. The shaded area represents sunset to sunrise. The peak in CO after sunset (start of gray-shaded area) is used to denote the beginning of the smoke event. We limit our analysis to sunrise on the following day (06:15 LT). The color labels A-D indicate individual times used to calculate ERs (see section 2.6.2). m/z 85 in the bottom time series indicates the sum of furanone and cis-2-butenediol.

Figure 2.3 shows the child-to-parent oxidation ratios for maleic anhydride and m/z 85 relative to furan during the night of 3-4 Feb. Just prior to sunrise (04:00 – 06:15 LT), both OVOC/VOC ratios rapidly decreased, corresponding with increases in furan, CO, and acetonitrile (Figure 2.2). Maleic anhydride/furan dropped to 0.05, indicating little OH-oxidation which is anticipated as sunset occurred approximately 8 h beforehand. The ratio of m/z 85-to-furan reduces to an average of 2.5. While we cannot use this to quantify plume age since the two products are measured as a sum, this period produces the lowest ratio throughout the event, and

is therefore the “freshest” measured during the campaign, with prior periods having ratios 1.6 – 2.8 times greater. We note that at a value of 2.5, this plume has likely undergone significant aging. Further corroboration of these results, determined via particulate matter (PM) composition, can be found in Simmons et al. (2022). In their study, a time-of-flight aerosol chemical speciation monitor was employed and observed the ratio of PM<sub>1</sub> mass fraction at  $m/z = 44$  ( $f_{44}$ ), where a lower mass fraction indicated a less oxidized plume. A decrease at  $f_{44}$  in the PM<sub>1</sub> mass fraction was observed in the same timeframe as the  $m/z$  85 and maleic anhydride tracers.

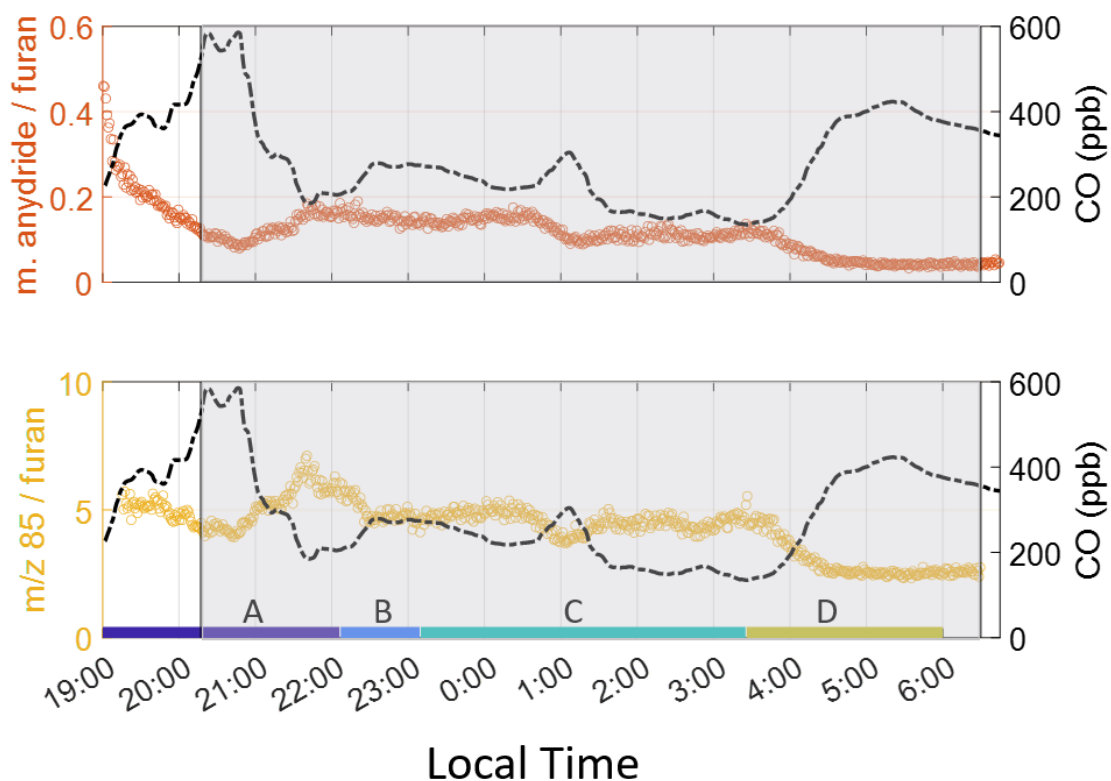


**Figure 2.3** Product-to-reactant ratio for furan oxidation products. Both ratios indicate the period just before sunrise is least oxidized. Again, the color labels A-D indicate individual times used to calculate ERs.  $m/z$  85 indicates the sum of furanone and cis-2-butenediol.

The rapid decreases in OVOC/VOC ratios are unlikely to result from shifts in chemistry alone. Instead, this suggests a shift in meteorological conditions which brings in smoke from a closer source, in agreement with measured wind direction, which shifted from flowing northeast to north at this time. We further investigate plume transport using a back-trajectory model.

#### **2.4 Plume origin and transport time**

We used a HYSPLIT back-trajectory model (Stein et al., 2015) to determine the origin and transport time of the smoke arriving at the site throughout the smoke event. The meteorological input used is the Global Data Assimilation (GDAS) dataset. The model used the field site as the terminal point and was set to assess trajectories at three different altitudes at 10 m, 500 m, and 1500 m above ground level (agl) to capture plume height. Our period of interest spans from 17:00 LT Feb 3, just before CO enhancements are seen at the site, to 06:00 LT 4 Feb when furan concentrations rapidly decrease. The model was set to calculate the trajectory of an air mass up to 12 h backwards in time for every hour in the period of interest (shown in Figure 2.1, colored by time).

A shift in trajectories occurred between 17:00 and 18:00 3 Feb, where airmasses came from the southwest rather than from the east. This corresponded with the arrival of the smoke plume as indicated by observed CO enhancements. Subsequent trajectories originated near two clusters of fires approximately 315-360 km to the southwest, located on the southeast (SE) coast of the continent (denoted as the SE fire clusters from here on). The model showed that the

airmasses initially kept at low altitudes ( $< 50$  m agl) and were lofted up to 563 m agl when passing over the SE fire clusters (shown in Figure A.1). The plumes descended to 10 m agl as they reached the coast and finally the field site. The model showed smoke sampled between 04:00 – 06:00 4 Feb saw slower transportation, travelled less distance, and spent more time over land compared to the previous hours.

Fires just to the south of Canberra (236 km southwest of the field site) were extremely intense during the period of study. Plume mixing increases the uncertainty of the OVOC/VOC ratios and any derived EFs as different plumes are likely to vary in their combustion conditions, chemical processing, and level of dilution. Further investigation is conducted via HYSPLIT forward trajectories (Figures A.2 and A.3). In short, during this period, plumes from the Canberra fires were lofted to  $>1800$  m agl well before crossing with the SE-fires plume, which attained a maximum altitude up to 560 m agl. This indicates little influence from the Canberra fires on our measurements. Additionally, the Canberra forward trajectories shift to the northwest after local midnight 4 Feb and no longer intersect with the plumes coming from the SE fire cluster.

The SE fire clusters are approximately 70 km apart in the SE, the influence of precipitation and wind speed (Figures A.4-A.6) is considered to determine whether combustion conditions were comparable. Both fires experienced similar total precipitation in the month prior and experienced similar wind speeds during this smoke plume event. As a result, we conclude that combustion conditions are similar and that EFs derived from this plume would be representative of a biome average. Over the entire course of the event, HYSPLIT analysis

suggests transport time from the fires to the field site is around 8 h (>200 km), but potentially shorter for the time frame immediately prior to sunrise.

## **2.5 O<sub>3</sub> and NO<sub>2</sub> time series**

Detailed time series of O<sub>3</sub> and NO<sub>2</sub> are presented in this section in Figure 2.4. Information regarding instrumentation and corresponding setups can be found in section 2.1 of Simmons et al. (2022). Like Figure 2.2, a CO time series is provided to outline the general trend of smoke during the event.

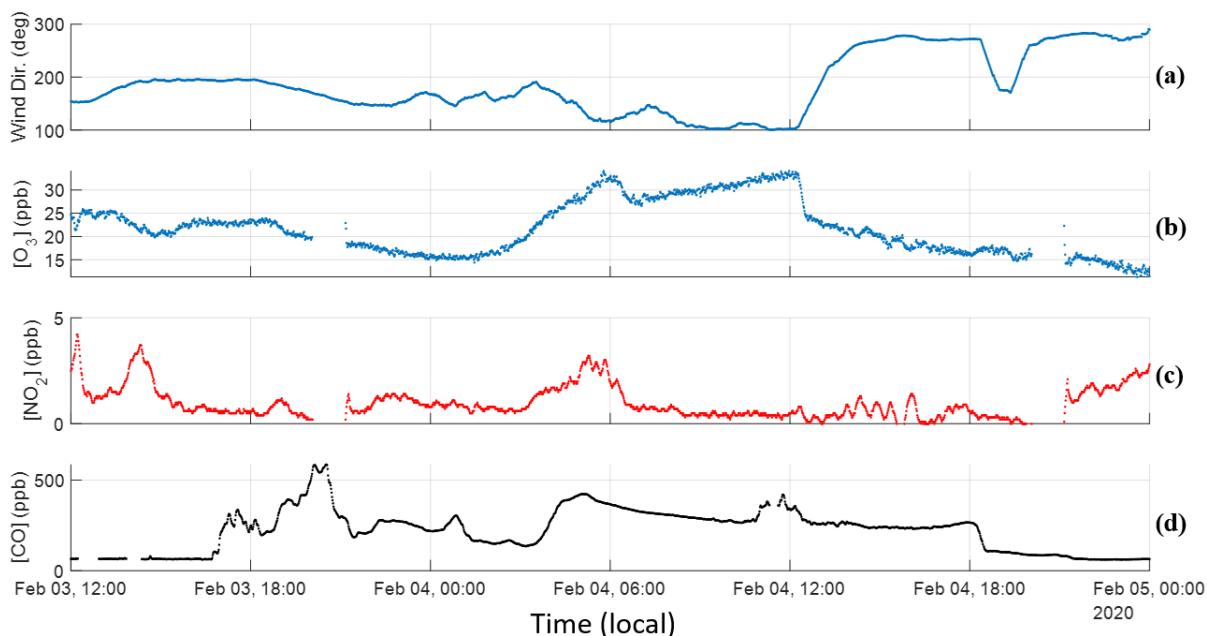


**Figure 2.4** Time series for  $O_3$ ,  $NO_2$ ,  $CO$ , and wind direction. (a) Wind direction, read as true north being  $0^\circ$  and continues clockwise. (b)  $O_3$  trends well with  $CO$  until sunrise occurs, wherein  $BBVOC+OH$  oxidation combined with biogenic  $VOC$  emissions led to daily production. The close trend with  $CO$  over the nighttime indicates transport rather than local formation. (c)  $NO_2$  also shows a similar trend but upon sunrise begins to negatively correlate with  $CO$  and  $O_3$ . (d)  $CO$  smoke tracer provide as time series reference.

A non-smoke influenced daytime and nighttime average (composed of 8 h averages) was calculated for  $O_3$  and  $NO_2$  concentrations using data from the month of March. Smoke around the continent had been either transported or removed by rain by this time.  $O_3$  was calculated to have a daytime concentration of 24.6 ppb and a nighttime concentration of 19.5 ppb. Respective concentrations were calculated for  $NO_2$  at 2.2 ppb in the day and 3.3 ppb in the evening. Additionally, averages for a larger suite of gas and aerosol phase variables over all smoke events sampled during the COALA-2020 campaign can be found in Simmons et al. (2022).

As stated before, smoke-related enhancements were visible around 17:30 LT (Figure 2.4d), with the hours prior being virtually devoid of tracers. Enhancements pick up without a shift in wind direction, with winds at this time travelling to the northwest, consistent with the HYSPLIT trajectories presented in Figure 2.1. As the wind approaches a more easterly direction, enhancements in CO are maintained and concentrations of more reactive BBVOCs begin to increase. O<sub>3</sub> concentration on 3 Feb reaches a maximum of approximately 25 ppb around 14:00 local time and maintains this level until sunset where it decreases as biogenic sources are no longer emitting and photolysis is halted. O<sub>3</sub> concentration reduces to a minimum 15.6 ppb and NO<sub>2</sub> decreases down to 0.8 ppb both around midnight and both below the nighttime monthly average despite enhancements in CO. O<sub>3</sub> has a  $R^2 = 0.48$  with CO and, when considering the known transport time of this smoke, indicates transportation rather than local production. Given the comparatively low concentrations of both compounds at this time, it is likely that this plume is depleting these species. This is compounded with the low concentrations of NO<sub>2</sub> in this temperate forest setting and, despite emitting NO<sub>x</sub>, wildfire plumes being generally NO<sub>x</sub>-limited (Jaffe and Wigder, 2012; Robinson et al., 2021).

Around 03:30 LT, the wind shifts from traveling northwest to west, significantly enhancing O<sub>3</sub>, NO<sub>2</sub>, CO, and total VOC concentrations, corresponding to the least aged portion discussed in section 3. Sunrise occurs around 06:30 coinciding with a steady decline in highly reactive VOC enhancements (Figure 2.2) and NO<sub>2</sub> (Figure 2.4c). Liang et al. (2022) found a significant correlation of  $R^2 = 0.86$  between NO<sub>2</sub> and maleic anhydride for a transported plume of similar age oxidized in the daytime. The opposite trend is observed in our scenario despite our

measurements exhibiting comparable trends from maleic anhydride. The  $\text{NO}_x$ -limited environment and differences in biogenic VOC (BVOC) quantities arising from the forest setting in this study and the urban setting in theirs are likely responsible for the opposing trends in the  $\text{NO}_2$  time series. Maleic anhydride similarly peaks around noon on the 4th, and both its production and the fast depletion of furan indicate that OH chemical pathways generally oxidize this plume faster than  $\text{NO}_3$  reaction pathways. While  $\text{O}_3$  concentration continues to increase after sunrise, it cannot be stated that this is dominantly due to BBVOC oxidation given the strong source of BVOC emissions from the surrounding forest. Isoprene nitrates sequester  $\text{NO}_2$ , ultimately leading to  $\text{O}_3$  production. The diel cycle of  $\text{O}_3$  and isoprene on a non-smoke affected day strongly correlate to temperature and photoactive radiation.  $\text{O}_3$  does achieve a max concentration of 30 ppb at 12:00 4 Feb, which is approximately 5.5 ppb above the daytime average and higher than the prior day despite similar temperatures (23.6 C on the 3rd, and 24.5 C on the 4th). This most likely results from the combination of transported  $\text{O}_3$  compounded with enhanced reactivity from the plume plus local, biogenic-related production. The plume is diluted at a consistent rate until 18:00 4 Feb when a shift in wind direction significantly reduces CO enhancements and concludes the smoke event.

## **2.6 Emission factors**

### **2.6.1 Species selection**

To identify compounds suitable for EF derivation, we compared our list of measured ions with compounds identified in previous literature (Brilli et al., 2014; Gilman et al., 2015; Hatch et al., 2015; Stockwell et al., 2015a; Bruns et al., 2017; Koss et al., 2018a; Pagonis et al., 2019). To corroborate species assignment, we examined correlations of identifiable compounds with CO, acetonitrile, furans, and phenolic compounds which are well-established smoke tracers. We also examined tracer-tracer relationships, for instance the anti-trend between maleic anhydride and furan resulting from OH oxidation (Gkatzelis et al. 2024). We excluded compounds with low proton affinities ( $< 170 \text{ kJ mol}^{-1}$ ) that are known to have humidity-dependent calibration factors (e.g., HCHO, HCN). This resulted in 150 VOCs species measured and identified during the smoke event.

We further filtered our VOC list by two criteria. First, VOC + NO<sub>3</sub> reaction rates must be available either in the NIST Chemical Kinetics Database (Manion, 2015) or Master Chemical Mechanism (v3.3.1) (Jenkin et al., 1997; Jenkin et al., 2003; Saunders et al., 2003; Bloss et al., 2005). Second, the VOC must have a sufficiently long lifetime against NO<sub>3</sub> oxidation to be minimally impacted over the 8 h transit time from the active fires to the field site ( $\tau_{\text{BVOC}+\text{NO}_3} < 8 \text{ h}$ , again assuming  $[\text{NO}_3] = 8 \times 10^7 \text{ molec cm}^{-3}$ ). This limited subsequent analysis to 15 nighttime long-lived VOCs

## 2.6.2 Calculating emission ratios

An ER is defined here as the slope of a linear regression of a given VOC to CO (both in units of ppb). Following Guérette et al. (2018), ERs are reported if correlation between a given VOC and CO are sufficiently well correlated ( $R_2 \geq 0.5$ ). High correlation minimizes the impact of the choice of regression method (e.g. orthogonal, York) on calculated slopes (Wu and Yu, 2018), and removes the need to account for background corrections. Analysis of surrounding influential sources can be found in Simmons et al. (2022). We use a reduced major axis regression to determine emission ratios. Given the time component that affects our measurements, it should be noted that compounds with low emission factors and high reactivity are likely to be excluded as they have been reacted away before reaching the site, thus exhibiting an insufficient CO correlation.

We first derive ERs using all data from the “freshest” portion of the plume as determined from OVOC/VOC ratios (Marked “D” in Figure 2.2). This produces 15 ERs that meet our criteria. We expect this period to provide the most accurate representation of original VOC emissions. We then calculate ERs for more aged portions of the smoke event (Periods A-C, Figure 2.2), performing regression analysis on the chemically distinct time periods. The start and end time of each period is determined by visual inspection of VOC/CO behaviors, which all exhibit similar distinct periods. Figure 2.5 provides an example of the analysis using acrolein. We average the slopes from each of these lines to derive an average ER for the full smoke event and compare to just the freshest portion of the plume (Period D). We find that using only the freshest smoke compared to using all the data generates very similar results for 9 of the 15

compounds (of which these 9 all have multiple ERs over the evening). Relative differences of the resultant ERs are within 1.5 – 47 % with two outliers: C8-aromatics (88%) and C3-benzenes (212 %). Three compounds have only 1 ER from all 4 periods (maleic anhydride, benzaldehyde, and creosol) so there is no standard deviation, but the remaining compounds from period D are captured within  $1\sigma$  of ERs from periods A-D (shown in Figure A.7).

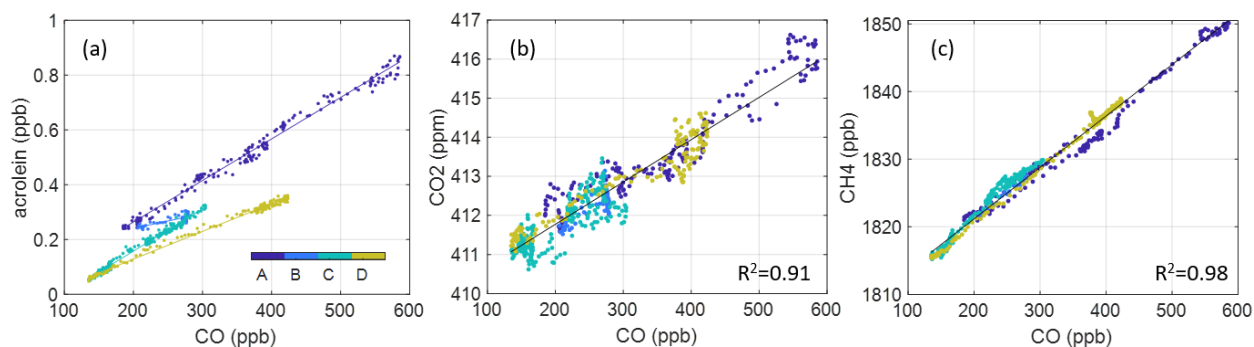


**Figure 2.5** Example ER analysis (a) using acrolein, wherein the smoke event is partitioned into 4 periods over the evening. Average ERs (slopes) from periods A-C agree closely with those in the freshest portion of the plume (D). Panels (b) and (c) show the singular ERs derived for CO<sub>2</sub> and CH<sub>4</sub> using the entire nighttime dataset (A-D).

Good agreement between methods allows us to extend our analysis beyond the freshest part of the plume, and therefore allows us to report ERs for a larger number of compounds. When focusing only on the freshest part of the plume, maleic anhydride, and benzaldehyde must be excluded due to insufficient  $R^2$  with CO. All ERs reported here and used in EF calculation use the “average over evening” method and include these compounds. Additionally, only one ER for CO<sub>2</sub> and CH<sub>4</sub> have been calculated using the dataset from periods A-D. Both these compounds

are long-lived, and from visual inspection, they do not form distinct time periods like the VOC ERs (shown in Figure 2.5b and c). A table with the resultant VOC ERs is also provided in the supplement (Table A.3). We use the CO<sub>2</sub> ER to determine an average modified combustion efficiency with the following equation:

$$MCE = \frac{ER_{CO_2}}{ER_{CO_2} + ER_{CO}} \quad (1)$$

where the ER<sub>CO</sub> is just unity and ER<sub>CO<sub>2</sub>/CO</sub> is 10.82 ppbCO<sub>2</sub> ppbCO<sup>-1</sup>. This results in an MCE calculation of 0.92, indicating a less efficient, even mixture of smoldering and flaming (Akagi et al., 2011).

### 2.6.3 Calculating emission factors

Emission factors are defined as the mass of some trace gas emitted per mass of dry biomass burnt. The most direct way of calculating this quantity is capturing total emissions released from a fire as well as knowing the quantity of fuel burnt. Unless experiments are conducted in a laboratory setting, these quantities are not known. As such, emission factors are calculated according to the carbon mass balance method (Akagi et al., 2011; Selimovic et al., 2018), using CO as the reference gas for the 15 reported species which produces the following equation:

$$EF_X = F_{carbon} * 1000 * \frac{MM_X}{MM_C} * \frac{ER_{X/CO}}{ER_{Y/CO}} \quad (2)$$

where  $F_{\text{carbon}} = 0.5$  and is the assumed carbon fractional content of the fuel as used in previous studies (Akagi et al., 2011a; Paton-Walsh et al., 2014).  $MM_X$  is the molar mass of compound X,  $MM_C$  is the molar mass of carbon,  $ER_{X/CO}$  is the CO ER of X, and  $\sum ER_{Y/CO}$  is the sum of  $ER_{CO_2/CO}$ ,  $ER_{CH_4/CO}$ , and  $ER_{CO/CO}$ . These ERs constitute the major volatilized carbon components of the plume, but the resulting EFs may be overestimated by 1-2% (Andreae, 2019) as this method assumes all volatilized carbon is detected including particulate carbon, VOCs, CO, and  $CO_2$ .

EFs derived in this work are presented in Table 2.1 alongside results from 2 eastern Australia-based studies by Lawson et al. (2015) and Guérette et al. (2018), 2 western US-based studies sampling emissions from corresponding temperate fuel types by Liu et al. (2017a) and Permar et al. (2021), and 1 study by Akagi et al. (2011) that provides EFs for general temperate zones. Additionally, Figure A.8 displays these results via scatter plot.

**Table 2.1** EFs ( $\text{g kg}^{-1}$ ) derived in this work compared to 2 studies conducted in the same or near temperate Australian forests, 2 US-based aircraft campaigns sampling western temperate US fuels, and 1 study reporting EFs across geographically distant temperate forests.\* Again, m/z 85 indicates the sum of furanone and cis-2-butenediol.

				<b>Biome Location</b>				
			AU	AU	AU	US	US	Temperate Forests
<b>Compound</b>	<b>Formula</b>	<b>m/z</b>	<b>This work</b>	<b>Guérette et al. (2018b)</b>	<b>Lawson et al. (2015b)</b>	<b>Liu et al. (2017b)</b>	<b>Permar et al. (2021b)</b>	<b>(Akagi et al., 2011b)</b>
Methanol	CH <sub>4</sub> O	33.00	2.01±0.58	3.0±0.5	2.07±--	2.45±1.43	1.50±0.39	1.93±1.38
Acetonitrile	C <sub>2</sub> H <sub>3</sub> N	42.03	0.16±0.03	0.70±0.10	0.25±--	0.25±0.13	0.31±0.15	--
Acetaldehyde	C <sub>2</sub> H <sub>4</sub> O	45.03	0.57±0.20	1.20±0.30	0.92±--	1.64±0.52	1.70±0.43	--
Acrolein	C <sub>3</sub> H <sub>4</sub> O	57.03	0.23±0.08	--	--	--	0.40±0.18	--
Acetone	C <sub>3</sub> H <sub>6</sub> O	59.05	0.55±0.28	0.80±0.20	0.54±--	1.13±0.82	0.84±0.22	--
MVK+MACR	C <sub>4</sub> H <sub>6</sub> O	71.05	0.18±0.03	1.0±0.30	0.38±--	0.33±0.06	0.39±0.15	--
Benzene	C <sub>6</sub> H <sub>6</sub>	79.05	0.25±0.08	0.39±0.07	0.69±--	0.43±0.12	0.50±0.14	--
m/z 85	C <sub>4</sub> H <sub>4</sub> O <sub>2</sub>	85.03	0.83±0.27	--	0.57±--	0.39±--	0.32±0.11	--
Methyl propanoate	C <sub>4</sub> H <sub>8</sub> O <sub>2</sub>	89.06	0.07±0.03	--	--	--	0.081±0.036	--
Maleic Anhydride	C <sub>4</sub> H <sub>2</sub> O <sub>3</sub>	99.00	0.05±--	--	--	--	0.14±0.072	--
Methyl methacrylate	C <sub>5</sub> H <sub>8</sub> O <sub>2</sub>	101.06	0.07±.04	--	--	--	0.11±0.045	--
Benzaldehyde	C <sub>7</sub> H <sub>6</sub> O	107.05	0.05±--	--	--	--	0.04±0.026	--
C8-aromatics	C <sub>8</sub> H <sub>10</sub>	107.09	0.08±0.05	0.11±0.03	0.26±--	0.15±0.004	0.21±0.08	--
C3-benzenes	C <sub>9</sub> H <sub>12</sub>	121.10	0.07±0.06	--	0.27±--	--	0.069±0.031	--
Creosol	C <sub>8</sub> H <sub>10</sub> O <sub>2</sub>	139.08	0.05±--	--	--	--	0.14±0.11	--

\* Dashes indicate either EF or EF variability not reported in study.

First, in comparison with the Australia-based studies, Guérette et al. (2018) reports EFs notably larger than those presented in this work, with only benzene and C<sub>8</sub>-aromatics showing good agreement. Except for these two compounds and C<sub>3</sub>-benzenes, Guérette et al. (2018) reports larger EFs than Lawson et al. (2015) and none within agreement. Our results more

closely agree with Lawson et al (2015) with methanol, acetone, and furanone EFs within  $1\sigma$ , and acetonitrile and acetaldehyde falling within a factor of 2. This agreement is likely due to both this work and Lawson et al. (2015) examining opportunistically intercepted smoke plumes that experienced some processing whereas Guérette et al. (2018) sampled near-source, controlled ground burns. Guérette et al. (2018) reports an acetonitrile EF  $\sim 4.5$  times higher than this work and  $\sim 3$  times greater than Lawson et al. (2015) constituting one of the largest disparities. This is attributed to the native and abundant Acacias which are N-fixing species located mainly in forest understories. Their measurements likely had a higher proportion of this foliage constituting the total fuel load due to both proximity to the forest floor and resulting leaf litter. Another of the largest differences is MVK+MACR, which shows a disparity of  $\sim 6$  times this work and 3 times that of Lawson et al. (2015). This is also most likely explained by differences in sampling approach in that proportional contributions of vegetation vary and plumes in Guérette et al. (2018) did not undergo any dilution or photochemical processing.

In comparison with US-based studies, methanol, acetonitrile, acetone, and benzene agree across both studies within  $1\sigma$ , with acrolein, methyl propanoate, methyl methacrylate, C<sub>3</sub>-benzenes, and creosol agreeing very well with values reported by Permar et al. (2021). It should be noted that though within the estimated uncertainties, the value for creosol reported by Permar et al. (2021) is  $\sim 3.5$  times greater than the value in this work, which constitutes another of the largest disparities in this dataset. Additionally, methanol agrees well with the value from Akagi et al. (2011). The EF for m/z 85 in this work is also expectedly larger than both other values presented here at  $\sim 3$  times greater than Permar et al. (2021). This is likely due to the plume sampled in this work undergoing the longest transport of any plumes measured in other studies.

Perhaps an unexpected finding is that EFs derived in this work agree better with observations in the US than the Guerette et al. (2018) study, which was in the same region as the COALA-2020 measurements. It should be noted that all studies except Guerette et al. (2018) are from plumes sampled several km downwind. Differences previously characterized as arising from varying fuel types may actually result from measurement approaches to deriving EFs and proximity to emission source. Agreement across results from this work and from the US-based studies lends credence to the use of newly presented EFs for modeling purposes in temperate Australian forests. Additional analysis is conducted in Appendix A (section A.4) and compares this work's EFs with wildfire EFs from two more U.S.-based studies (Prichard et al., 2020; Gkatzelis et al., 2024) and one more global study (Andreae, 2019), as well as EFs from two U.S.-based laboratory studies (Stockwell et al. 2015, Koss et al. 2018).

The laboratory studies show extremely good agreement with all EFs from the three studies within uncertainty (Figure A.9). For the wildfire studies, EFs ( $\pm 1\sigma$ ) from this work are all within EFs ( $\pm 1\sigma$ ) from Andreae (2019), two-thirds are within EFs ( $\pm 1\sigma$ ) and from Gkatzelis et al. (2024), and one-half are within EFs ( $\pm \sigma$ ) (all are within a factor of 2) from Prichard et al. (2020) (Figure A.10). These results further corroborate the use of U.S. temperate EFs for modeling wildfire emissions in temperate Australian biomes.

## **2.7 OH reactivity**

As this plume has been shown to oxidize faster when exposed to the OH radical as opposed to the NO<sub>3</sub> radical, this indicates that the nighttime transport of this plume would be able to comparably preserve OH reactivity. We investigate this by first determining which compounds were most significant in their enhancements, and then determine their corresponding OH reactivity.

First, a subset of the PTR-ToF-MS data was created by calculating ERs using the methodology described in section 2.6.2 over the same nighttime period. However, we did not filter out compounds by their atmospheric lifetime, and any unidentified species were not considered regardless of correlation strength. This means the resulting OH reactivity is likely to be slightly low, but this method ensures reactivity solely from compounds attributable to BB emissions is being gauged. Then, an average for each compound was calculated using the same period for ERs. These nighttime averages were then compared with their diurnal cycles calculated using data from 1 – 19 Mar 2020 (ending date of PTR-ToF-MS sampling ambient air). If a compound's mean over the smokey period is greater than the mean of its diel cycle plus 1σ over the same timeframe, this compound is considered in the transported OH reactivity. Finally, we background correct the nighttime concentrations using the March diurnal cycles and convert to reactivity using equation 3:

$$R_{OH} = \sum[VOC_i] * A * k_{VOC_i+OH} \quad (3)$$

where  $[\text{VOC}_i]$  is the concentration of the  $i$ th VOC in units of parts-per-billion,  $A$  is the conversion factor to  $\text{molec}_i \text{ cm}^{-3}$  ( $A = 2.46 \times 10^{10}$  in units of  $\text{molec}_{\text{air}} \text{ cm}^{-3} \text{ ppb}^{-1}$  at 1 atm and  $25^\circ \text{C}$ ), and  $k_{\text{VOC}_i + \text{OH}}$  is the OH rate constant for the corresponding  $\text{VOC}_i$ . Rate constants were again sourced from the same databases as the  $\text{NO}_3$  rate constants. The OH rate constant used for  $m/z$  85 was determined as an average of the constant provided in Koss et al. (2018) ( $k_{\text{OH}} = 44.2 \times 10^{-12} \text{ cm}^3 \text{ molec}^{-1} \text{ s}^{-1}$ ) and Bierbach et al. (1994) ( $k_{\text{OH}} = 52.1 \times 10^{-12} \text{ cm}^3 \text{ molec}^{-1} \text{ s}^{-1}$ ) assuming both compounds contributed equally to signal at this mass peak.

Ultimately, 26 compounds were determined to have the most significant contributions, transporting an average OH reactivity of  $7.5 \text{ s}^{-1}$ , with a minimum of  $5.85 \text{ s}^{-1}$  occurring around 03:00 4 Feb and a maximum of  $13.2 \text{ s}^{-1}$  around 20:00 3 Feb, shown in Figure 2.6. These values are well within range of those seen in nighttime and aged, daytime transported plumes by Liang et al. (2022), who measured a total OH reactivity range from approximately  $4\text{-}26 \text{ s}^{-1}$ . We calculate an OH reactivity from the primary biogenic VOCs (isoprene plus monoterpenes) for further comparison. The maximum biogenic value, achieved around 12:00 4 Feb, is  $6.35 \text{ s}^{-1}$  and the average biogenic reactivity over the course of the campaign is  $5.90 \text{ s}^{-1}$ , indicating that the nighttime conditions allowed for the transport of a reactivity quantity that approximately doubled OH reactivity at the COALA-2020 field site. Additionally, there is little variability in the relative contributions to reactivity across these different groups over the course of the smoke event, indicating the plume experienced a consistent oxidation over the course of its travel.

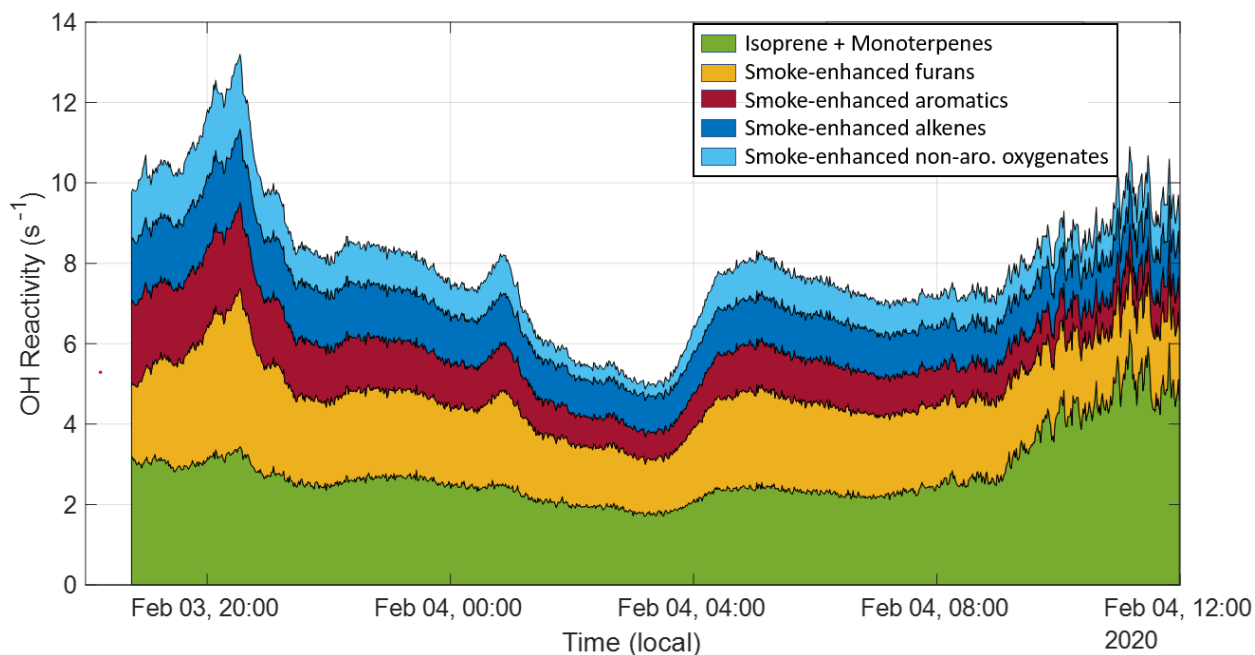


**Figure 2.6** Selected compounds with significantly high smoke-related enhancements are grouped into categories of varying reactivity based on known reactivity groups, except for the “isoprene + monoterpenes” group which is the sum of isoprene (m/z 69) and monoterpene (m/z 137) reactivities. This captures every compound included in this OH reactivity calculation.

Compounds from the plume have been grouped into four categories to capture their diversity. Expectedly, biogenic emissions contribute the most to total reactivity (attributable dominantly to isoprene), but the furans group is the most reactive with values from 1.24-3.93 s<sup>-1</sup>. This group contains various furans (furan, 2-methylfuran, m/z 85, and furfural alcohol) wherein m/z 85 is by far the most significant, contributing up to 69% of the group total. This high m/z 85 presence explains why this group is also the most OH reactive as most furans were oxidized by NO<sub>3</sub> during this transport timeframe, except m/z 85 which has a long  $\tau_{\text{NO}_3}$  but a comparatively shorter  $\tau_{\text{OH}}$ . The furan reactivity range is comparable to lab-based values measured in Gilman et al. (2015) which ranged from 1.3 – 5.5 s<sup>-1</sup>. Both these studies find lower furan reactivities than

lab measurements made in Koss et al. (2018) at an average reactivity of  $14.2 \text{ s}^{-1}$ , where furans constitute the third highest reactivity group. Aromatics make up the second most reactive group (range of  $0.66\text{-}2.14 \text{ s}^{-1}$ ) in this study, with dominant contributions from phenol (39%), styrene (33%), and catechol (32%). Catechol's contribution is likely less than this as other studies have revealed that it shares a significant portion of its mass peak with 5-methyl furfural (Stockwell et al., 2015; Koss et al., 2018). Despite their high  $\text{NO}_3$  reactivity, phenolic compounds still dominate the overall OH reactivity contributions in this category. These compounds appear across other studies as primary contributors to OH reactivity (Gilman et al., 2015; Hatch et al., 2017; Koss et al., 2018; Sekimoto et al., 2018; Decker et al., 2019; Liang et al., 2022). Alkenes (range of  $0.86 - 1.83 \text{ s}^{-1}$ ) are on par with aromatics, for which their reactivity is largely attributable to propene and butene, followed last by non-aromatic oxygenates (range of  $0.28\text{-}1.87 \text{ s}^{-1}$ ), which contain compounds like methanol, acetaldehyde, and acetic acid. The comparably low reactivity from this group is unexpected as other studies have shown that the dominant contributions to reactivity come from this group (Gilman et al., 2015; Koss et al., 2018; Liang et al., 2022).

## **2.8 Conclusions**

EFs were derived for a total of 15 trace gas species via measurements from a PTR-ToF-MS and an FTIR spectrometer, the resulting OH reactivity of the transported plume quantified, and  $\text{O}_3$  and  $\text{NO}_2$  time series investigated. The COALA-2020 ground-based field campaign opportunistically sampled a sustained biomass burning plume from 3 – 4 Feb 2020 during the

2019-2020 wildfire season in New South Wales, Australia. We determined via HYSPLIT trajectories that the most likely pathway traveled by the plume was from a distance ranging from ~230-375 km south from fires along the temperate forests of the east coast with negligible contributions from more inland fires near Canberra, Australia. This plume lofted to an altitude of 563 m agl as it passed over active fires ~8 h out from the field site, before descending to 10 m agl while traveling over the ocean and reaching the site at 17:30 LT 3 Feb. All data used in the derivation of EFs was limited from sunset on 3 Feb to sunrise on 4 Feb as this period showed the greatest enhancements of reactive BB tracers like furan. Through visual inspection, we partitioned this plume event into 4 portions, and calculated and averaged the individual ERs. We used two age marker ratios derived from furan radical oxidation to determine the freshest portion of the plume and found that ERs from this portion corresponded well with the averaged ERs (within  $1\sigma$ ). Using EFs from the entire evening allowed for the inclusion of three more VOC EFs into this analysis which, for the freshest portion of the plume, did not meet the selection criteria for ERs.

We have further characterized wildfire emissions in Australia's temperate region by providing a more comprehensive suite of biome-averaged VOC EFs. This suite introduces new EFs for acrolein, methyl propanoate, methyl methacrylate, maleic anhydride, benzaldehyde, and creosol. Of particular note is acrolein, which has been shown to be a gas-phase variable posing significant harm to human health (O'dell et al., 2020; Simmons, 2022). When compared with values reported from 2 Australian studies located in the same or nearby temperate forests, we find mixed agreement with results from Guérette et al. (2018) as only two values are captured within our EF variability, with acetonitrile differing by a factor of ~4.5 times and MVK+MACR

differing by ~6 times. However, 2 compounds are within the range of variability for Lawson et al. (2015) and 2 others are well within a factor of 2, which indicates reasonable agreement. Furthermore, comparison with two recent US studies that report data on analogous temperate zones, as well as one report covering global temperate regions, show generally good agreement for 9 of the 15 compounds, with several others within a factor of 2, indicating very good agreement. This closer agreement with these studies, as well as that of Lawson et al. (2015), is likely due to the measurement approach when deriving EFs as both US-based studies were aircraft campaigns, and the Australia-based study intercepted a transported plume much like this work. Guérette et al. (2018) sampled controlled burns on a ground campaign virtually at the emission source. This indicates that variability previously ascribed to differing fuel types may be overshadowed by sampling approach and that comprehensive measurements from US-based studies may be useful for studying Australian biomes. Agreement with both Lawson et al. (2015) and the US-based studies indicates that results here are valid for future use in Australian, biome-specific biomass burning studies. Compounding this is the excellent agreement found between EFs in this study and a comparison of two laboratory, U.S.-based, temperate fuel studies, indicating the potential for lab-based results to be similarly applicable. Chemically comprehensive near-source observations of Australian fuel types are needed to evaluate the importance delineating temperate forest EFs in different regions across the globe.

Probing the OH reactivity of the plume revealed that the nighttime conditions, despite the long transport time, transported a quantity that effectively doubled OH reactivity at the COALA-2020 field site, with contributions arising from expected classes of compounds such as furans (most contribution), aromatics (second), and alkenes (third).  $m/z$  85 contributed most

significantly of the furans measured, which is due to its long  $\text{NO}_3$ -lifetime but short OH-lifetime. Other furans had largely been reacted away before reaching the COALA-2020 field site. Phenol had the largest contribution of the measurable phenolic compounds despite its high  $\text{NO}_3$  reactivity. Alkenes and aromatics were found to have on par reactivities and, unexpectedly, non-aromatic oxygenates contributed the least.

## CHAPTER 3

### EVALUATION OF AERIS MID-INFRARED ABSORPTION (MIRA), PICARRO CRDS (CAVITY RING-DOWN SPECTROSCOPY) G2307, AND DINITROPHENYLHYDRAZINE (DNPH)-BASED SAMPLING FOR LONG-TERM FORMALDEHYDE MONITORING EFFORTS

#### 3.1 Introduction

Observations of formaldehyde (HCHO) provide useful insight into the photochemical formation of secondary pollutants and the sources and fate of volatile organic compounds (VOCs). While direct emissions of HCHO from wildfires, the biosphere, and anthropogenic activities can contribute to ambient mixing ratios (Parrish et al., 2012; Lui et al., 2017; Luecken et al., 2018; Alvarado et al., 2020; Wu et al., 2021), regional HCHO abundance is generally governed by secondary production (Parrish et al., 2012; Zhang et al., 2013; Zhu et al., 2014; Luecken et al., 2018; Zeng et al., 2019). Because HCHO photolysis and oxidation are sources of HO<sub>x</sub> radicals, HCHO loss can further propagate oxidative chemistry (Tonnesen and Dennis, 2000; Lin et al., 2012; Valin et al., 2016; Wolfe et al., 2019; Yang et al., 2021). Additionally, HCHO is a known carcinogen ranking highest in health risks among the 187 hazardous air pollutants listed by the US Environmental Protection Agency (EPA) in the Clean Air Act (Scheffe et al., 2016; Strum and Scheffe, 2016; Zhu et al., 2017b). Due to its central role in atmospheric chemistry, HCHO is a target molecule at EPA Photochemical Assessment Monitoring Station (PAMS) and National Air Toxics Trends Station (NATTS) network sites for which observations are typically included in chemically comprehensive field intensives.

Since 1990, the standard EPA approach for HCHO measurements is collection on 2,4-dinitrophenylhydrazine (DNPH)-coated cartridges followed by offline derivative detection via high-performance liquid chromatography (HPLC), known as the TO-11A method (U.S. Epa, 1999). Sample collection and analysis are resource and labor intensive with measurements typically reported over sampling times that are on the order of hours. EPA TO-11A measurements in the PAMS and NATTS are 8 or 24 h integrated samples collected every 3 or 6 d, respectively. The low time resolution limits the usefulness of observations for studies of both photochemistry and air toxics exposure. Previous approaches have used modeled diel cycles or satellite-based observations in combination with the TO-11A method to infer ground-based diel cycles (Zhu et al., 2017a; Wang et al., 2022). However, this DNPH method of capturing HCHO has known interferences from NO<sub>2</sub> and O<sub>3</sub> (Karst et al., 1993; Achatz et al., 1999; Tang et al., 2004), can be impacted by relative humidity (RH) (Wisthaler et al., 2008; Uchiyama et al., 2009; Ho et al., 2014), and has had mixed results in comparison to research-grade observations (Hak et al., 2005; Wisthaler et al., 2008; Dunne et al., 2018), making the accuracy of these inferred diel cycles difficult to determine. While other studies have demonstrated the feasibility for continuous measurements via various spectroscopy-based methods (Yokelson et al., 1999; Cardenas et al., 2000; Dasgupta et al., 2005; Hak et al., 2005; Spinei et al., 2018; St Clair et al., 2019; Dugheri et al., 2021), the number of multi-month, ground-based, continuous, in situ HCHO measurements is limited to a handful of studies, all of which employ a proton-transfer-reaction mass spectrometer (Warneke et al., 2013; Hansen et al., 2014; Coggon et al., 2021).

A HCHO monitoring instrument more suitable for long-term deployment would reduce manual labor and provide continuous observations, experience little or correctable drift in

instrument baseline and sensitivity, and have low uncertainty and sufficient precision at typical ambient concentrations. In recent years, several commercially available instruments have been developed towards that goal, including a cavity ring-down spectroscopy (CRDS) instrument from Picarro, a photoacoustic gas analyzer from Gasesera, and tunable diode laser spectroscopy (TDLS) instruments from Aeris Technologies and Aerodyne Research, Inc. Here, we focus on the Aeris mid-infrared absorption (MIRA) and Picarro CRDS G2307 instruments, which have been compared against other instruments in a small number of informal (Whitehill et al., 2018; Furdyna, 2020) and peer-reviewed (Shutter et al., 2019; Glowania et al., 2021) intercomparison efforts. Glowania et al. (2021) is the only peer-reviewed work to employ a G2307 using the current spectral fitting algorithm (version 1.6.015), which updates the procedure for fitting at low humidity. The Aeris Ultra, which offers improved thermal stabilization over the Aeris Pico, has not previously been examined in literature. Whereas previous comparisons were conducted either in controlled chamber studies or through the analysis of short-term ambient observations, a full characterization of instrument suitability in measurement networks requires multi-month deployment.

Previous intercomparisons involving either Aeris MIRA or Picarro CRDS instruments have highlighted concerns with measurement accuracy as a function of ambient humidity. The Aeris MIRA technique relies on a HDO (deuterated water) line (located at  $2831.8413 \text{ cm}^{-1}$ ) for spectral referencing. At low humidity ( $< 0.2 \text{ \% H}_2\text{O}$ ), the Aeris Real-Time (ART) fitting algorithm cannot reliably reference its HDO spectral feature, and the instrument fails to produce measurements (Shutter et al., 2019). Including  $\text{CH}_4$  as a secondary spectral reference in data post-processing extends the range of conditions under which the Aeris instruments work, though

the instrument's precision decreases by a factor of  $1.2 \pm 0.3$ . While the G2307 fitting algorithm uses both H<sub>2</sub>O and CH<sub>4</sub> spectral references, CH<sub>4</sub> fitting currently remains a research approach for ART. Whitehill et al. (2018) found an inverse correlation between Picarro HCHO measurements and instrument-reported water mixing ratios at typical ambient concentrations and, along with Furdyna (2020), observed that the G2307's measurements were lower by 1–2 ppb HCHO compared to DNPH-based measurements. Glowania et al. (2021) found that variable humidity can decrease reported HCHO concentrations by as much as 1.75 ppb with the most significant offsets at  $\leq 0.2\%$  H<sub>2</sub>O where the H<sub>2</sub>O spectral feature is not clearly observed.

Both the Picarro and Aeris instruments periodically sample HCHO-free air to determine an instrument baseline. Several scrubbers are capable of removing HCHO, the most common of which are DNPH-coated cartridges (DNPH), heated catalytic hydrocarbon scrubbers like oxides of copper and manganese (Hopcalite, HO), calcium sulfate (Drierite, DR), and molecular sieves (MS) (Herndon et al., 2007; Cazorla et al., 2015; Pei et al., 2015; Shutter et al., 2019; St Clair et al., 2019; Fried et al., 2020). These methods differ in removal mechanism, molecular selectivity, and desiccation efficiency. DNPH-coated cartridges are recommended by Aeris Technologies and are chemically selective for carbonyls, thus allowing the majority of H<sub>2</sub>O to pass through. Heated HO is expected to oxidize HCHO to CO, forming H<sub>2</sub>O as a by-product and providing a humidified airstream that may also be suitable for baseline determination. Picarro Inc. recommends instrument zeroing via adsorption by DR. A column of MS is often plumbed in the upstream area of a DR column (DR+MS) as it both desiccates the gas flowing through it and, with the right pore size, removes molecules with kinetic diameters greater than that of HCHO. This both prevents the DR from becoming saturated and prolongs its HCHO-removal efficiency

as only smaller organic compounds can adsorb to it. HO and DR+MS may be less cost-intensive and longer-lasting and have a comparable HCHO-removal efficiency to DNPH-coated cartridges. However, since humidity is known to impact HCHO concentrations, the impact of scrubber choice on overall measurement accuracy is unclear.

We use HCHO measurements taken over 1 year in Atlanta, GA, from the Picarro G2307 and the Aeris instruments with aims to determine the best calibration procedures and optimal measurement configurations and to assess the suitability for remote, continuous operation. We compare co-located observations from all three monitors as well as observations from the Picarro G2307 and TO-11A DNPH analysis. For each continuous monitor, we assess the performance over a range of zeroing methods and ambient humidities. Finally, we demonstrate the use of Picarro G2307 and Aeris Ultra and Pico measurements for long-term, continuous observations of HCHO spatial gradients in an urban environment and discuss the feasibility of deploying these instruments to form a spatiotemporally comprehensive network.

## **3.2 Instrument description**

### **3.2.1 Picarro G2307**

#### **3.2.1.1 CRDS operating principles**

The operating principle of cavity ring-down spectroscopy as used by the G2307 is described fully in Glowania et al. (2021) and briefly summarized here. Air is pulled through a temperature- and pressure-controlled cavity at a rate of 0.4 standard liters per minute (SLPM). Laser light is directed into the resonance cavity, where three high-reflectivity mirrors create effective path lengths on the kilometer scale. After the laser is shut off, the small amount of light transmitted through one mirror is monitored via photodetector. Detected light exponentially decays, with faster decay rates corresponding to higher absorption of light in the cavity. An on-board wavelength monitor measures the absolute laser wavelength with a precision that is 3 orders of magnitude narrower than the HCHO spectral linewidth. The instrument can change the voltage applied to the laser and tune it to wavelengths that HCHO is known to either minimally or maximally absorb at, producing closely clustered spectral features at and around the HCHO absorption peak. The laser scans the 5625.5 to 5626.5  $\text{cm}^{-1}$  wavelength range at a 100 Hz repetition rate, while the length of the cavity is adjusted to achieve resonance. On-board spectral fitting and signal averaging results in measurements of HCHO, CH<sub>4</sub>, and H<sub>2</sub>O reported at 1 Hz. The unit assessed in this work utilizes the same spectral fitting algorithm as described in Glowania et al. (2021).

### 3.2.1.2 Determining instrument baseline

The G2307 measurements reported here differ from prior studies primarily in that we employed an external zeroing system. The system is equipped to sample from either DNPH (Supelco LpDNPH S10L), DR (Drierite, 8 mesh, > 98 % CaSO<sub>4</sub>, < 2 % CoCl<sub>2</sub>), or DR+MS (Sigma Aldrich molecular sieve, 3 A pore size zeolite beads) to regularly monitor and correct the instrument's baseline. The baseline is defined throughout this work as the signal reported by the instrument when sampling from a HCHO-free source and drift as the rate of change in the baseline. This setup was accomplished by connecting the G2307 inlet to a three-way perfluoroalkoxy (PFA) solenoid valve which alternated between an ambient sampling line and a zeroing line. The zeroing line was then connected to another three-way PFA solenoid valve to which the scrubbers were attached. The instrument sampled from DR or DR+MS for 5 min of every hour. Every fourth hour, the instrument sampled for 5 min through DNPH either directly before or after sampling from DR. The relative order of DR/DNPH sampling was found to have no impact on reported instrument baselines.

### 3.2.1.3 Humidity dependence

Two trials were performed to quantify the impact of humidity on G2307 measurements. HCHO-free air was provided by either a zero-air (ZA) generator (Tofwerk) with a DR column (trial 1) or an Airgas ultra zero grade air cylinder (trial 2). The ZA generator uses a platinum catalyst heated to 400 °C and requires the DR column as it does not remove water vapor. A

portion of the ZA stream was humidified by using a bubbler containing high-purity water (Barnstead GenPure Pro, 18.2 MΩ cm resistivity, < 5 ppb total organic carbon). The fraction of ZA humidified was varied using a mass flow controller such that the measured water vapor mole fraction ranged from 0.05–1.7 %.

Figure 3.1 shows the reported HCHO concentrations in HCHO-free air as a function of measured % H<sub>2</sub>O. As reported in Glowania et al. (2021), data fell into two linear regimes with a demarcation at 0.2 % H<sub>2</sub>O. Data were averaged to 5 min and each regime fitted using a York regression (York et al., 2004) with standard deviations of the measurements used as uncertainty. We find significantly smaller slopes (lower H<sub>2</sub>O influence) than Glowania et al. (2021), indicating that humidity dependencies may be instrument specific. The HCHO offset is defined in Eq. (1):

$$[HCHO]_{offset} = \begin{cases} (-5.67 \pm 0.47) * [H_2O] + (0.13 \pm 0.02), \% H_2O < 0.2 \\ (-0.40 \pm 0.02) * [H_2O] - (0.01 \pm 0.02), \% H_2O \geq 0.2 \end{cases} \quad (1)$$

where  $[HCHO]_{offset}$  (ppb) accounts for the HCHO signal lost at some % H<sub>2</sub>O and  $[H_2O]$  is the corresponding instrument-reported % H<sub>2</sub>O mole fraction.

Depending on the instrument zeroing method, ambient and baseline humidities may be very different. These differences could lead to significant biases in reported HCHO differential measurements. For example, Figure 1 suggests the use of a desiccant, such as DR, for sampling ambient air at 1 % H<sub>2</sub>O would generate a bias of –0.4 ppb if the humidity dependence is not

corrected. We emphasize the importance of experimentally determining a correction factor for humidity effects before deployment.

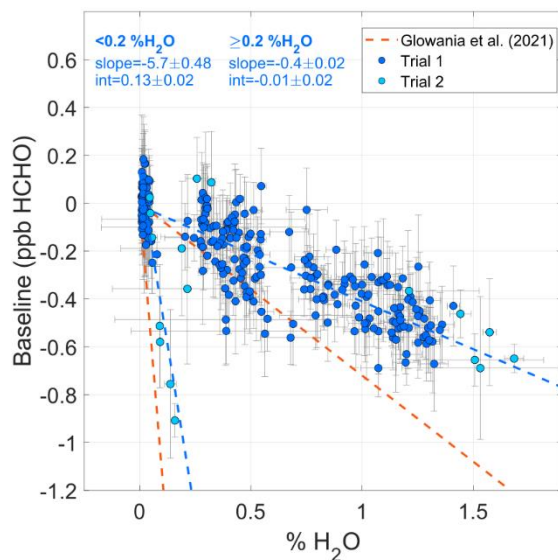


**Figure 3.1** Picarro G2307 HCHO concentrations as a function of measured H<sub>2</sub>O concentrations. Regressions for the two H<sub>2</sub>O spectral fitting regimes are plotted alongside the slopes from Glowania et al. (2021). Error bars are the standard deviation in instrument baseline or % H<sub>2</sub>O for each 5 min averaged point.

#### 3.2.1.4 Data processing

Averaged HCHO datasets at variable time resolutions (1– 60 min) were created from the 1 Hz data using the following procedure: first, all 1 Hz data were corrected for humidity effects by subtracting the [HCHO]offset from Eq. (1). Observations made within 30 s of a valve change were removed and baseline measurements were then averaged to 4.5 min points and linearly

interpolated to create an instrument background on the same time basis as ambient data. The interpolated baseline was subtracted from the 1 Hz ambient measurements. Baseline-corrected ambient data were averaged to the desired time resolution with any periods having < 50 % data completeness discarded. Data were further screened to exclude points where scrubbers were exhausted and therefore unreliable.

#### 3.2.1.5 Impact of scrubber choice – DNPH, DR, and DR+MS

Before comparing scrubbers, we first examine the HCHO removal efficiency of DNPH compared to a ZA generator. We find instrument baselines were on average 14 ppt larger than those measured using a ZA generator. This difference was consistent whether sampling the indoor conditions or ambient air. This difference is not statistically significant given the instrument precision and accuracy determined later in section 3.3. We note DNPH initially off-gases material that produces spectral interferences that subside after a “burn-in” period of ~ 2 h. It is possible that off-gassing material could have negative effects on instrument performance if used the long term (e.g., mirror degradation). These impacts were not seen in our study and would require further investigation.

The impact of DR and DR + MS on the Picarro G2307’s baseline was then assessed using ambient measurements taken from the consecutive sampling of DNPH and DR/DR + MS in the ambient sequencer schedule. We combine the DR and DR + MS measurements as we find the two methods produce baselines with a relative difference that is within instrument

measurement uncertainty. The 4.5 min averaged baselines are shown in Figure 3.2. Both scrubbing methods produced normally distributed baseline measurements with means and standard deviations of  $-0.39 \pm 0.14$  ppb (DNPH) and  $-0.38 \pm 0.15$  ppb (DR/DR+MS) and an average absolute difference of  $< 0.03$  ppb HCHO. This difference is finer than the 5 min precision of the instrument and demonstrates a comparable performance between the two scrubbing methods.

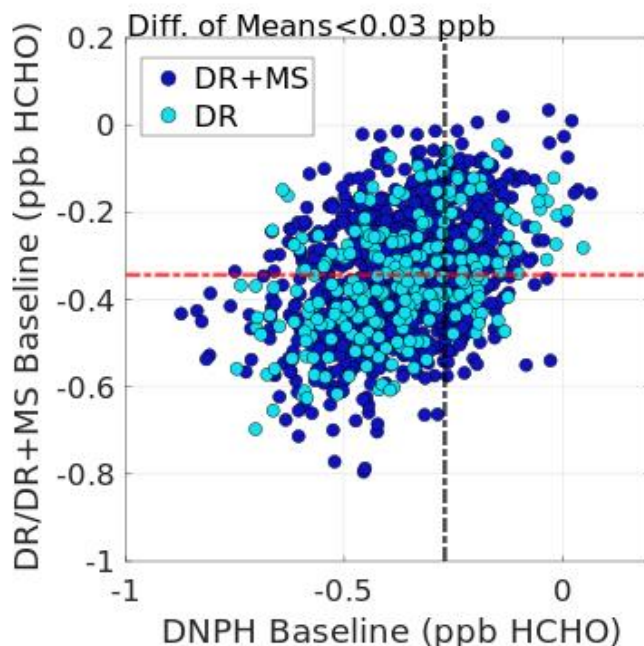


**Figure 3.2** Picarro G2307 baselines determined using the DR, DR+MS, or DNPH scrubbing methods. Each data point represents a consecutive, 4.5-min averaged DNPH and DR baseline measurement while sampling ambient air.

Previous studies have noted that derivatization of hydrazine to hydrazone, which is the reaction that functionally captures HCHO in the DNPH-coated cartridge, is slowed or stopped at

RH < 15 % (Wisthaler et al., 2008; Uchiyama et al., 2009). Few days throughout the G2307's deployment fell below this threshold, and RH (converted from instrument-reported % H<sub>2</sub>O using indoor conditions) was always  $\geq$  25 %. While low RH likely did not affect our measurements, we note this is a limitation on DNPH as deployment in arid locations could hamper performance, whereas DR/DR+MS would operate unaffected.

Ho et al. (2014) found that high temperatures (> 22 °C) and RH (> 50 %) led to DNPH-HPLC analysis underestimating ambient HCHO by 35–80 %. This could inflate instrument baselines as summer 2022 in Atlanta regularly exceeded these values, with DNPH-derived baselines in Figure 3.2 having RH values in the range of 7–87 %. As DR baselines are determined using desiccated air and the average baseline difference with DNPH is within instrument precision, we conclude measurements are not significantly affected at high RH. These results lead us to conclude that either DR/DR+MS or DNPH usage with the G2307 is advisable so long as humidity corrections are applied.

#### 3.2.1.6 Instrument calibration

Single-point and dynamic dilution calibrations were conducted at the beginning, middle, and end of the G2307's deployment. Single-point calibrations were performed by flowing a concentrated standard (Apel Riemer: 1015 ppb  $\pm$  5 %; Airgas: 1031 ppb  $\pm$  10 %; or Airgas: 1044  $\pm$  10 %) through a SilcoNert-coated stainless-steel (SS) regulator and directly into the instrument. This configuration avoids interaction between the calibration gas and stainless-steel

surfaces, thereby reducing passivation times to sub-hour lengths. However, this technique relies on the assumption that observations are linear from 0–1 ppm HCHO. The single-point measured concentration was determined as the instrument-reported concentration multiplied by an N<sub>2</sub>–air matrix conversion factor of 1.0625 (Bent, 2023). Dynamic dilution calibrations were performed by diluting the HCHO standards with ZA from either a Toftwerk ZA generator or an ultra-ZA cylinder. After a 5 h passivation time at ~ 200 ppb HCHO, concentrations were varied in the 0–40 ppb range. Each concentration step was 3 h in duration with 5 min zeroing periods conducted hourly. Slopes from all calibrations (single-point, dynamic dilution, and original factory calibration) agreed within 10 %, with no systematic bias between calibration methods. This indicates both that G2307 measurements are linear up to a ppm range and that sensitivity remained stable during the 2021–2023 period. Ambient measurements are processed according to the temporally closest calibration. We determine the uncertainty in ambient measurements to be 10 % as per the uncertainty associated with the standards used for calibration.

### **3.2.2 Aeris MIRA**

#### 3.2.2.1 MIRA operating principles

The operating principle of the Aeris MIRA instruments is described fully in Shutter et al. (2019). Air is pulled at a rate of 0.45–0.75 SLPM into a folded Herriott detection cell, which achieves a path length of 13 m. The laser scans over the HCHO feature at 2831.6413 cm<sup>-1</sup> and HDO spectral feature at 2831.8413 cm<sup>-1</sup>. The ART algorithm corrects for broad slope in the raw

signal of the instrument baseline and then calculates measured HCHO and H<sub>2</sub>O concentrations based on absorption features. We use the two commercial Aeris MIRA models in this work: the Pico and the Ultra model. The Ultra is identical in operation but offers higher optical cell temperature stability and is designed for longer-term, low-drift measurements.

### 3.2.2.2 Instrument baseline

The Aeris instruments have a two-inlet design allowing for the determination of instrument baseline throughout the data collection process. We run the instruments in the “programmed” mode, which allows the user to select the duration of sampling through each inlet. The instruments also have a “differential” mode, which produces ambient HCHO concentrations using on-board baseline subtractions. The zero inlet was connected to either a DNPH-coated cartridge or a heated HO (United Filtration) scrubber and teed with the ambient inlet to the main sampling line as per the manufacturer’s recommendation. We sample ambient air for 180 s and scrubbed air for 30 s. This sequence was determined through visual inspection of Aeris time series with the intention of minimizing DNPH-sampling time while maintaining sufficient precision for ambient monitoring. We found 180 s to be the longest length of time between zeroes that either unit achieved where the instrument-reported HCHO signal remained consistently stable. Both units were then set to the same schedule. This led to DNPH-coated cartridges lasting 5-8 d, corresponding to a breakthrough time of 17-27 h. Variability in breakthrough time is dependent on ambient conditions and atmospheric chemical composition

### 3.2.2.3 Impact of scrubber choice – heated HO and DNPH for Aeris MIRA

As stated previously, the Aeris ART fitting algorithm requires the presence of H<sub>2</sub>O as a spectral reference for finding the HCHO absorption peak. We therefore do not consider desiccating scrubbers as an option. Throughout deployment, the Aeris instruments reported an ambient range of 0.18 – 3.3 % H<sub>2</sub>O while sampling through DNPH with only a few days in winter falling below the 0.2 % H<sub>2</sub>O threshold. The heated HO airstream produced humidities in a similar range to DNPH.

Ambient measurements of HCHO-scrubbed air from the Pico were used to assess the HCHO-removal efficiency of heated HO as compared to DNPH. The zeroing inlet on the Pico was teed to a DNPH-coated cartridge and a stainless-steel column (length of 20.3 cm, radius of 2 cm) containing 215 cm<sup>3</sup> of HO. The HO column was wrapped in high-temperature heat tape, insulated in a fiberglass sleeve, and heated to 180 °C. Pei et al. (2015) found that HO at this temperature achieved nearly 100 % HCHO removal and preserved the scrubber bed from H<sub>2</sub>O poisoning. A condensation trap and second particulate filter (PF) were placed downstream of the HO column to protect the instrument against potential liquid H<sub>2</sub>O and particulate matter. Two mass flow controllers were placed upstream of the scrubbers and used as valves. The Pico sampled from its zeroing inlet while the incoming flow alternated between scrubbers in 40 s intervals. The first 10 s of data after every switch was removed to preclude any effects from valve switching. This removal period was determined experimentally.

DNPH-scrubbed baselines exhibited a normal distribution centered around a mean and standard deviation of  $-13.63 \pm 0.54$  ppb. HO-scrubbed baselines exhibited a normal distribution with a larger mean of  $-12.92 \pm 0.34$  ppb resulting in an absolute difference of 0.71 ppb, which falls outside of the instrument's precision (discussed in section 3.3) and indicates less efficient HCHO removal. Since ambient humidity perennially remained sufficiently high in the Atlanta area, we recommend the use of DNPH for zeroing the Aeris instruments.

#### 3.2.2.4 Data processing

We generated temporally averaged datasets with variable time resolutions (1–60 min) using a data handling scheme like that of the Picarro G2307 observations. Zeroes are averaged to single points and interpolated to a 1 Hz resolution and subtracted from the 1 Hz ambient data, and  $\geq 50$  % data completeness is required for any averaging interval. We discard the first 5 s of measurements after a valve switch.

#### 3.2.2.5 Instrument calibration

In September 2023, both Aeris instruments were calibrated using dilutions of a HCHO gas standard (Apel Riemer:  $1015 \text{ ppb} \pm 5 \%$ ; Airgas:  $1044 \text{ ppb} \pm 10 \%$ ) with humidified ultra-ZA. The configurations for humidifying air and diluting the gas standard were as described in sections 3.2.1.3 and 3.2.1.6. Both instrument calibrations produced slopes within 5 % of the

original factory calibration, which occurred in February 2021. Intercepts were in the range of  $-0.03$ – $0.12$  ppb. These results indicate that the calibration throughout the instruments' respective deployments remained stable. In October 2022 and September 2023, standard addition calibrations were performed by adding small amounts of the gas standard to the ambient line. Expected concentrations are calculated as the flow-weighted average of the gas standard concentration and the ambient concentration. Ambient concentration is measured by a co-located reference instrument. In October 2022, the two Aeris units were co-located and informed one another. In September 2023, Picarro G2307 measurements were used as the reference.

Results for the standard addition calibrations are shown in Figure 3.3. York regressions (not plotted) incorporated the 1 min standard deviation of the measured concentrations, cylinder concentration uncertainty, and, for the standard addition calibrations, the measurement uncertainty associated with the corresponding reference instrument.

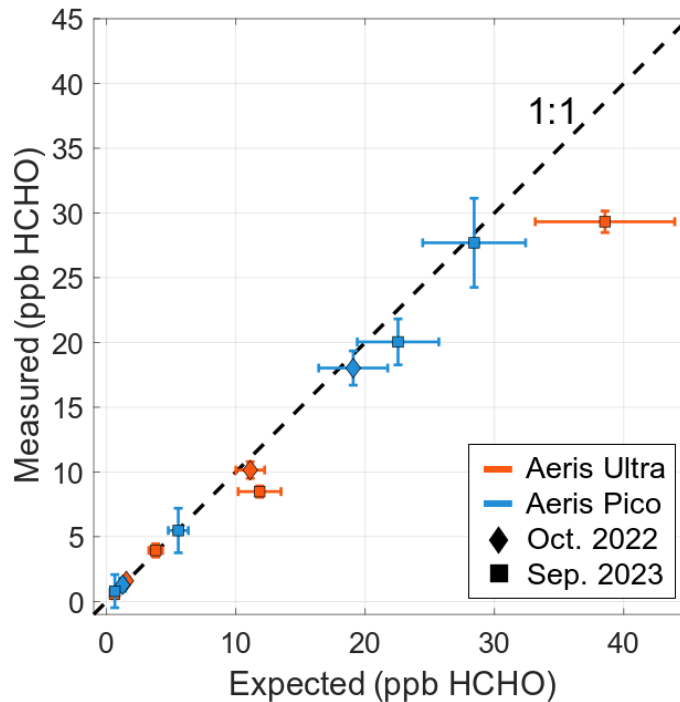


**Figure 3.3** Results from Aeris standard addition calibrations. Error bars are the uncertainty in each data point, with measured concentrations using the standard deviation of each averaged concentration step and expected concentrations using the cylinder uncertainty. For the standard addition, the measurement uncertainty of the reference instrument is also incorporated.

The Pico’s standard addition calibrations agreed closely with the ZA dynamic dilution calibration and produced slopes of  $0.94 \pm 0.16$  and  $0.97 \pm 0.16$ , intercepts of  $0.13 \pm 0.61$  and  $0.16 \pm 1.18$ , and normalized mean biases (NMBs) between measured and expected concentrations of  $-4.9\%$  and  $-5.5\%$  in 2022 and 2023, respectively. The high uncertainty with the 2023 intercept is attributed to issues with the instrument’s thermoelectric cooler which began in August 2023. All Pico data were processed according to the standard addition calibration closest in time.

The Ultra's 2022 standard addition calibration produced a slope of  $0.86 \pm 0.16$  and a NMB of  $-13.2\%$  between measured and expected concentrations. This calibration and the Ultra's 2023 dynamic dilution calibration agree within the uncertainties of both techniques. However, the 2023 standard addition calibration produced a slope of  $0.77 \pm 0.08$ , which has relative decreases of  $10.5\%$  from 2022 and  $19\%$  from the dynamic dilution calibration and a NMB of  $-22.8\%$  between measured and expected concentrations. This NMB persisted in the Ultra's ambient observations and could not be related to any measured instrument parameters.

These results suggest that standard addition calibrations are useful as a secondary check on instrument sensitivity once in the field. All ambient data for the Ultra data were processed using the 2023 standard addition calibration. This decision is owed to the intercomparison results presented in section 3.5, wherein application of this calibration most effectively reduces the NMB relative to the G2307 and Pico. Correspondingly, a  $14\%$  relative uncertainty from propagating the measurement uncertainties of the G2307 and Ultra in quadrature. A  $0.3$  ppb offset is added as per the Pico-FILIF (Fiber Laser Induced Fluorescence) comparison in Shutter et al. (2019), which falls within the range of calibration offsets seen in this work.

### **3.2.3 DNPH (TO-11A)**

Method TO-11A outlines in detail the EPA guidance on the preparation of DNPH-coated cartridges and subsequent analysis through HPLC (U.S. Epa, 1999). Formaldehyde was measured using an ATEC Model 8000 Toxic Air Sampler over three consecutive 8 h periods

spanning a full 24 h with samples collected every 3 d. Ambient air was drawn at a rate of 0.9–1.1 L min<sup>-1</sup> through a potassium-iodide-coated copper inlet heated to 50 °C to remove O<sub>3</sub> before passing through a DNPH-coated cartridge (Supelco LpDNPH S10) which collected carbonyls in their non-volatile, carbonyl-hydrazone derivative form. The denuder is necessary as it minimizes potential O<sub>3</sub>-related interferences in the resultant HPLC chromatograms (Vairavamurthy et al., 1992). At the end of the sampling period, the cartridges were capped and stored in a refrigeration unit at ≤ 4 °C until analysis. The cartridges were then eluted with 10 mL of acetonitrile and the eluent analyzed via a Waters HPLC-UV system with a temperature stabilized (25 ± 1 °C), reversed-phase C18-coated silica gel (1.7 μm particle size) column (bridged ethyl hybrid, 2.1 mm × 50 mm i.d.) at 360 nm wavelength. The eluents used in the HPLC process were deionized H<sub>2</sub>O and acetonitrile. The HPLC system was calibrated before each use with known concentrations of HCHO, and field samples are analyzed in comparison to blank cartridges.

Method TO-11A requires that collocated DNPH samples produce observations within 20 %, which is vindicated through EPA historical data (U.S. Epa, 1999). As such, an uncertainty of 20 % is assumed for TO-11A observations in this work. We note that this may not account for any biases caused by interfering species such as NO<sub>2</sub> or issues brought on by variable sample flow rates or ambient RH (Karst et al., 1993; Herrington and Hays, 2012; Ho et al., 2014; Souza et al., 2020).

### **3.3 Instrument precision and baseline drift**

The precisions of the three analyzers were characterized in two ways. First, the instruments' inlets were overflowed using a ZA source for 24 h and precision was calculated via an Allan–Werle curve (Allan, 1966), as in prior instrument characterization studies (Shutter et al., 2019; Glowania et al., 2021). Results are shown as the solid lines in Figure 3.4. The G2307 achieves precisions of 0.09, 0.05, and 0.03 ppb for integration times of 5, 20, and 60 min. This performance is similar to the 5 min 0.06 ppb precision reported by the manufacturer and results determined in Glowania et al. (2021). The Ultra achieves precisions of 0.20, 0.20, and 0.28 ppb for the same periods. The best precision achieved by the Pico is 0.66 ppb at a 30 s integration time. At longer integration times, fluctuations in concentrations reported by the Pico instrument can be attributed to thermal instability. Internal instrument temperatures varied by  $\pm 0.3$ – $0.4$  °C over the course of 7 h and were well-correlated ( $r > 0.85$ ) with the instrument baseline. Resultingly, precisions past 40 s integration times quickly became unsuitable for ambient monitoring. During deployment, the Pico's internal temperature was more stable compared to the ZA tests performed in the laboratory. When using 30 s zeroing periods from the Pico's ambient time series, a precision of 0.40 ppb HCHO is determined, which is comparable to that of the Ultra for the same integration window.

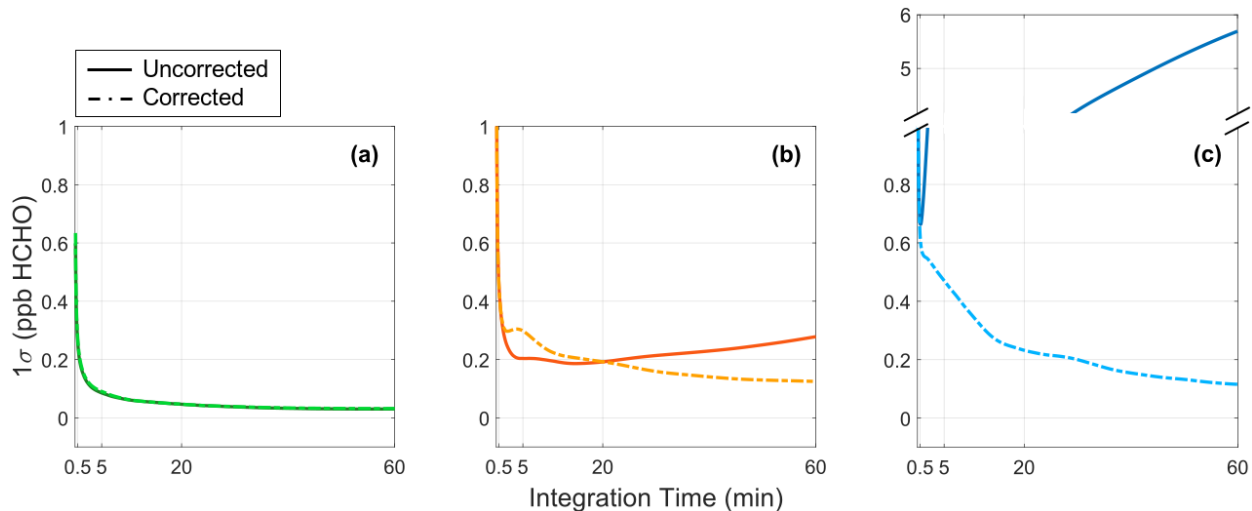


**Figure 3.4** Allan-Werle curves for a) Picarro G2307 b) Aeris Ultra and c) Aeris Pico

instruments. Uncorrected precisions (solid lines) are calculated without accounting for baseline variation, whereas corrected precisions (dashed lines) use the same baseline-characterization method used to process ambient data.

As Allan variance is not meant to address systematic errors like temperature effects, we developed a modified, or corrected, Allan–Werle curve that better characterizes the precision of ambient measurements. Still sampling ZA, we replicated the sampling sequences and data processing methods used for ambient measurements (i.e., the 1 Hz data are drift-corrected by averaging and subtracting out each zeroing period). We then treated the 1 Hz data measured on the “ambient” inlet as contiguous. Results are shown as dashed lines in Figure 3.4. For the Picarro G2307 (Figure 3.4a), there is no change in precision using this method, as the baseline is relatively constant in this period. Both Aeris units benefited significantly from this correction, reaching 40 min precisions of 0.140 and 0.154 ppb for the Ultra and Pico, respectively. The Pico’s modified precision is within 15 ppt of the 40 min precision of 0.14 ppb observed in

Shutter et al. (2019). The corrected Aeris Allan–Werle curves trend similarly to the G2307's, achieving better precisions with longer integration times. These results indicate that the ambient sampling sequences used for each instrument are sufficient to account for the influence of any physical instrument variables on the baseline. As the precision of the ambient measurements (which are calculated differentially) is impacted by both the precision of the ambient and zero baselines, the modified Allan–Werle curves do not account for the precision of the zero measurement. In our ambient dataset, we are limited to a 30 s integration time as per the sampling sequence of the Aeris units. The 30 s Allan deviation while sampling through DNPH in our ambient dataset is 0.45 ppb for the Ultra. For the Pico, observations prior to August 2023 have a precision of 0.41 and 0.66 ppb otherwise. This is taken as the true precision of the ambient dataset. Longer zeroing times may achieve higher precision in the dashed lines of Figure 3.4 if the baseline has sufficiently low drift through the sampling period.

To quantify instrument baseline drift, we show a typical time series of scrubbed-air observations for all three instruments. The period chosen spans 3–8 September 2022 and is shown in Figure 3.5. The zero measurements are averaged according to the respective data scheme for each instrument and plotted differentially relative to the first value of each time series. The G2307 exhibits comparatively little drift with a maximum difference of 1.3 ppb when sampling DR-scrubbed air, occurring late on 4 September. Over the same time frame, the Aeris Ultra's baseline can shift by up to  $\pm 6$  ppb, while the Aeris Pico baseline exhibits the most variability, changing by as much as  $\pm 20$  ppb just over the course of 12 h. This significant drift necessitates more frequent zeroing, thus reducing the total time spent sampling ambiently and exhausting scrubbers faster. At their fastest drift rates ( $1.67$  ppb HCHO  $\text{h}^{-1}$  for the Pico and

0.125 ppb HCHO h<sup>-1</sup> for the Ultra), the improved thermal stability reduces drift by a factor of 13.36. From our observations, we determined that the Pico should be zeroed at least every 3 min and the Ultra every 10 min under typical indoor-deployment configurations as the instrument-reported HCHO signals do not consistently remain stable at longer intervals. For the G2307, observations of the instrument baseline drift obtained using DR suggest that hourly zeroing is sufficient.

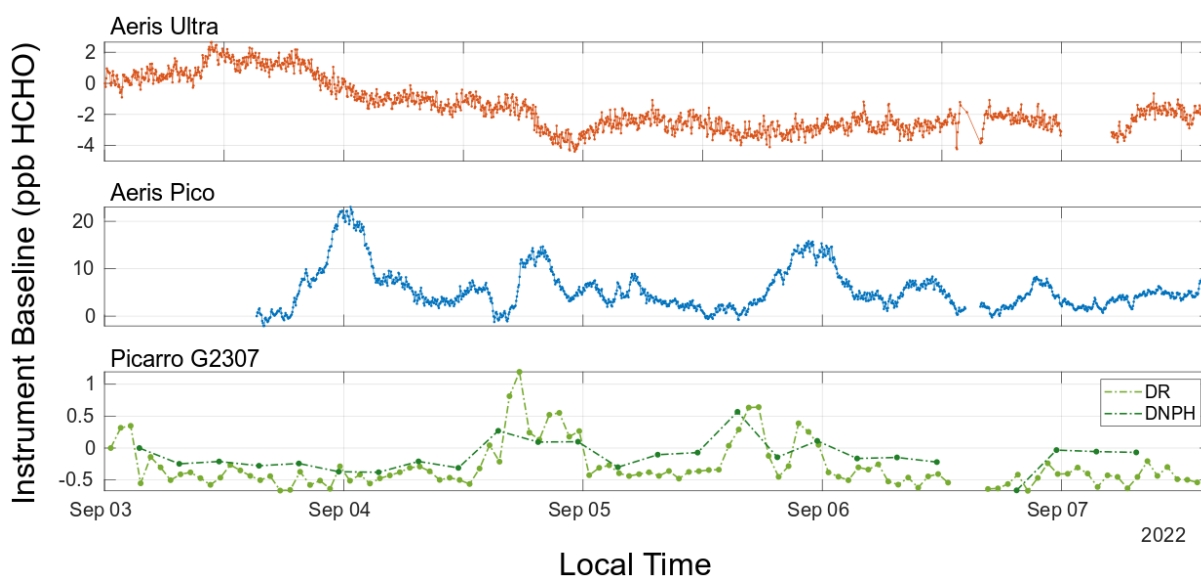


**Figure 3.5** Instrument baseline time series for all three HCHO monitors plotted differentially to the first point in the time series. The Ultra and G2307, equipped with better thermal stabilization, show significantly less drift than the Pico.

## **3.4 Intercomparison**

### **3.4.1 Field site descriptions**

#### **3.4.1.1 South DeKalb**

The location of the South DeKalb (SDK) PAMS is shown in Figure 3.6. The site is located approximately 19 km southeast of the university campus in a less industrialized area with comparatively greater tree coverage. The G2307 was permanently stationed at SDK, with two intercomparisons performed during its deployment. First, the Aeris Pico was co-deployed from 28 July to 13 September 2022 according to the configuration shown in Figure 3.7a. Then, the Aeris Ultra and Pico were co-deployed from 21–29 August 2023 in their standard ambient configurations without sharing ambient lines. Instruments were housed in a climate-controlled trailer with an indoor temperature maintained at 21–23 °C. All tubing was 0.125 in. i.d. (0.25 in. o.d.) PTFE with 7.5 m extending from inside the trailer and up a mast, where the inlet was situated 5 m above the ground. The G2307 and Pico instruments had flow rates of 450 cm<sup>3</sup> min<sup>-1</sup>, leading to a residence time of approximately 4 s when teed together and 8 s when separate. The Ultra had a flow rate of 800 cm<sup>3</sup> min<sup>-1</sup> with a residence time of 5 s. 1 μm PTFE particulate filters (PFs) in Savillex PTFE holders were used, and inlets were shielded by PTFE funnels covered with PTFE mesh. The indoor portion of the sampling lines were heated to 46 °C (≥ 1 °C above the cavity cell temperature of the instruments) to avoid condensation in the plumbing.

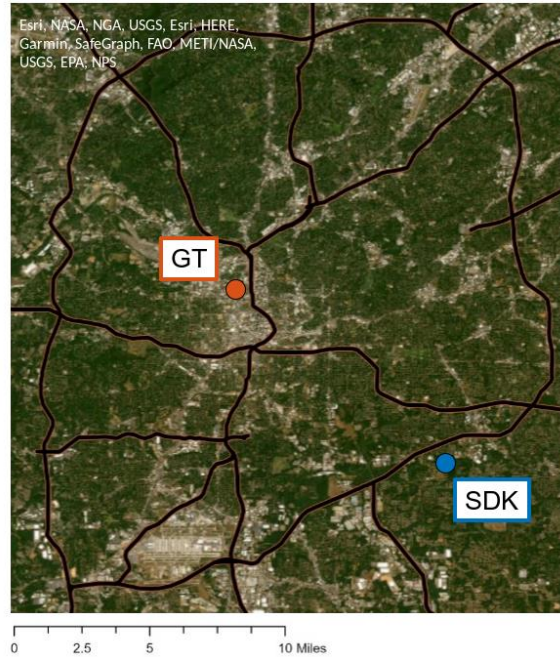


**Figure 3.6** Locations of the two field sites in the Atlanta, GA area where the Aeris Ultra, Aeris Pico, and Picarro G2307 were deployed.

The Aeris instruments' baselines were determined solely using DNPH, while the G2307 sampled between DNPH, DR, or DR + MS. When scrubbing only with DR, air was passed through two adsorption columns (length of 16 in., radius of 2 in.) in series containing 0.5 kg of material each. For DR + MS, the column first in the series was replaced with the MS material. When the adsorption columns were exhausted, the scrubber bed was replaced with either new or regenerated material. DR was thermally regenerated according to the manufacturer instructions.

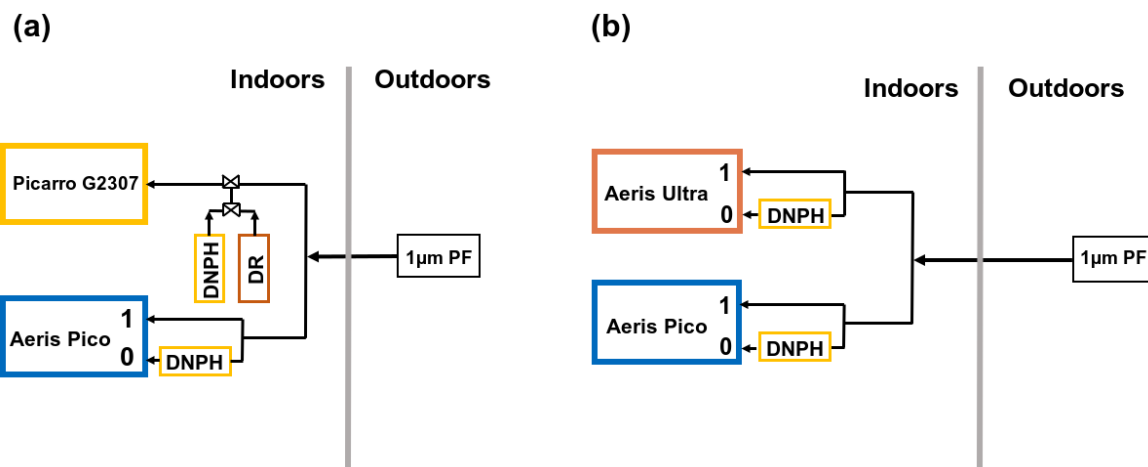


**Figure 3.7** Configurations of instruments during their respective intercomparisons. (a) shows the teed setup used from 28 July – 13 Sep 2022 for the Aeris Pico and Picarro G2307. When not co-located, the G2307 has the same configuration without being teed to the Pico. (b) shows the setup used for the Aeris instruments while deployed at GT from 25 – 28 July and 4 – 17 Oct 2022. For each panel, “0” references HCHO-scrubbed air, “1” is ambient air, and “PF” is a particle filter.

### 3.4.1.2 Georgia Tech

The Aeris instruments were co-deployed in the penthouse laboratory of the Ford Environmental Science and Technology building (GT, Georgia Tech) from 25–28 July 2022 and 4–18 October 2022 with the setups used during their co-located periods shown in Figure 3.7b. The ambient temperature of the lab was maintained at 22 °C. A total of 7 m of 0.25 in. o.d. (0.125 in. i.d.) PTFE line ran from the instruments through a wall port, where the inlet was suspended 3 m above the outdoor roof floor. As before, a 1 µm PTFE PF in a Savillex PTFE filter holder was attached, the inlet shielded with a PTFE funnel, and indoor tubing insulated to

prevent condensation from forming. The Aeris instruments solely used the DNPH-scrubbing method for zeroing.

### **3.4.2 Instrument intercomparisons**

#### **3.4.2.1 Continuous HCHO monitor comparison**

Figure 8 shows all HCHO observations from the Aeris and Picarro G2307 instruments from their co-location periods. York regressions of 20 min averaged data incorporate the measurement uncertainties defined in section 3.2. Observations correlate strongly ( $r \geq 0.9$ ) for each comparison.

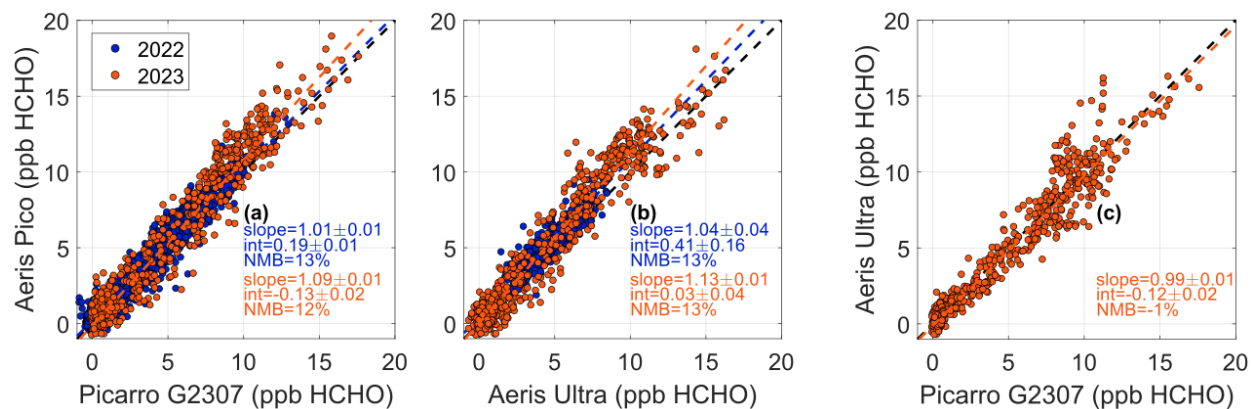


**Figure 3.8** Comparison of ambient observations from the three HCHO monitors assessed in this work. (a) Pico and G2307 observations taken at SDK in 2022 and 2023, (b) Pico and Ultra with 2022 measurements taken at GT in 2022 and SDK in 2023 (c) Ultra and G2307 observations at SDK 2023. Slopes and intercepts result from applying the York regression technique which incorporates the respective uncertainties of each instrument.

The Pico had a NMB of 12 %–13 % relative to the G2307 (Figure 3.8a), with slopes ranging from 1.01 to 1.09. Figure 3.8b shows a Pico NMB of 13 % compared to the Ultra, with slopes ranging from 1.04 to 1.13. Before applying a standard addition calibration factor, the Ultra’s observations were consistently lower compared to the other instruments. The good agreement in the Ultra vs. G2307 comparison (Figure 3.8c; slope = 0.99; NMB = -1 %) supports the use of the standard addition calibration. Intercepts for all regressions range from -0.11–0.41 ppb, which is near or less than the intercomparison offsets observed in Shutter et al. (2019) for ART-fitted measurements.

The scatter around the lines of best fit is primarily owed to the low precision of the Aeris ambient measurements, which is determined by the 30 s zeroing intervals. There are occasional periods of large deviations from the lines of best fit. These periods typically lasted multiple hours, suggesting accuracy (rather than precision) is the cause of the deviations. Specifically, on four separate occasions the Aeris instruments both measured 10–15 ppb HCHO, while the Picarro observations remained at  $\sim 10$  ppb. Reasons underlying this behavior could not be traced to measured instrument parameters or ambient variables.

#### 3.4.2.2 Picarro G2307 and TO-11A DNPH comparison

Figure 3.9 compares G2307 observations from June–August 2022 with those from co-located TO-11A measurements. One-minute integrated G2307 concentrations are averaged to the 8 h TO-11A sampling window. We find moderate correlation ( $r = 0.75$ ) and a  $-52\%$  NMB of TO-11A observations relative to the G2307 (slope =  $0.35 \pm 0.02$ ). Previous studies have demonstrated DNPH-based observations being up to 25 % lower relative to continuous HCHO observations (Hak et al., 2005; Dunne et al., 2018). Hak et al. (2005) determined slopes in the range of 0.64–0.83 when comparing DNPH-HPLC and Hantzsch fluorometric measurements. A comparison of Hantzsch and G2307 observations in Glowania et al. (2021) produced a slope of 1.08.

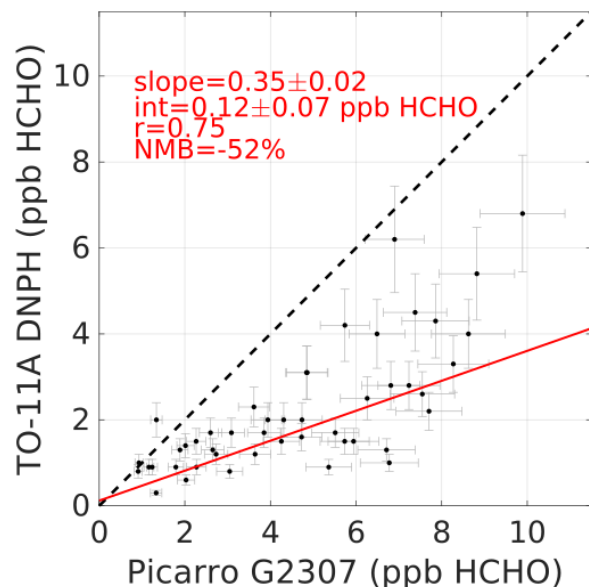


**Figure 3.9** 8 h TO-11A DNPH observations compared to Picarro G2307 observations at the SDK site from June through August 2022. Error bars represent the 10 % and 20 % uncertainty associated with the G2307 and TO-11A measurements.

While a low bias is not unusual for TO-11A measurements, the magnitude of the discrepancy presented here is larger than in prior studies. We find 8 h G2307 and TO-11A observations are well correlated ( $|r| > 0.6$ ) with temperature, RH, and  $O_3$ , which are expected to either drive ambient HCHO or reflect its secondary chemistry. TO-11A observations did not correlate notably with  $NO_2$  which would be expected to bias reported HCHO concentrations high (Herrington and Hays, 2012). Noted in section 3.2.1.5, summertime in Atlanta exhibits high RH and temperatures, which can lead DNPH measurements to underestimate ambient HCHO by 35–80 % (Ho et al., 2014). While we are unable to provide a definite reason for this significant discrepancy, the accuracy and stability shown through the G2307’s calibrations as well as its

agreement with the Aeris units (with independently verified accuracies) lend confidence to its measurements.

### **3.5 Suitability for long-term deployment**

To demonstrate whether these continuous HCHO monitors capture the urban HCHO gradient, we plot time series from both field sites from August 2022–January 2023 (Figure 3.10) and quantify the HCHO concentration gradient that arises between GT (located in Atlanta’s urban core) and SDK (a less industrialized, rural–urban area). Gaps in data typically result from downtime due to scrubber exhaustion or instrument maintenance. The Aeris instruments overall have less available data due to more frequent and intense scrubber usage, valve failures, and spectral fitting failures that could not self-correct. Over this period, the Pico was stationed at both field sites with only sparse data available after 18 October 2022 as it was dedicated to other experiments.

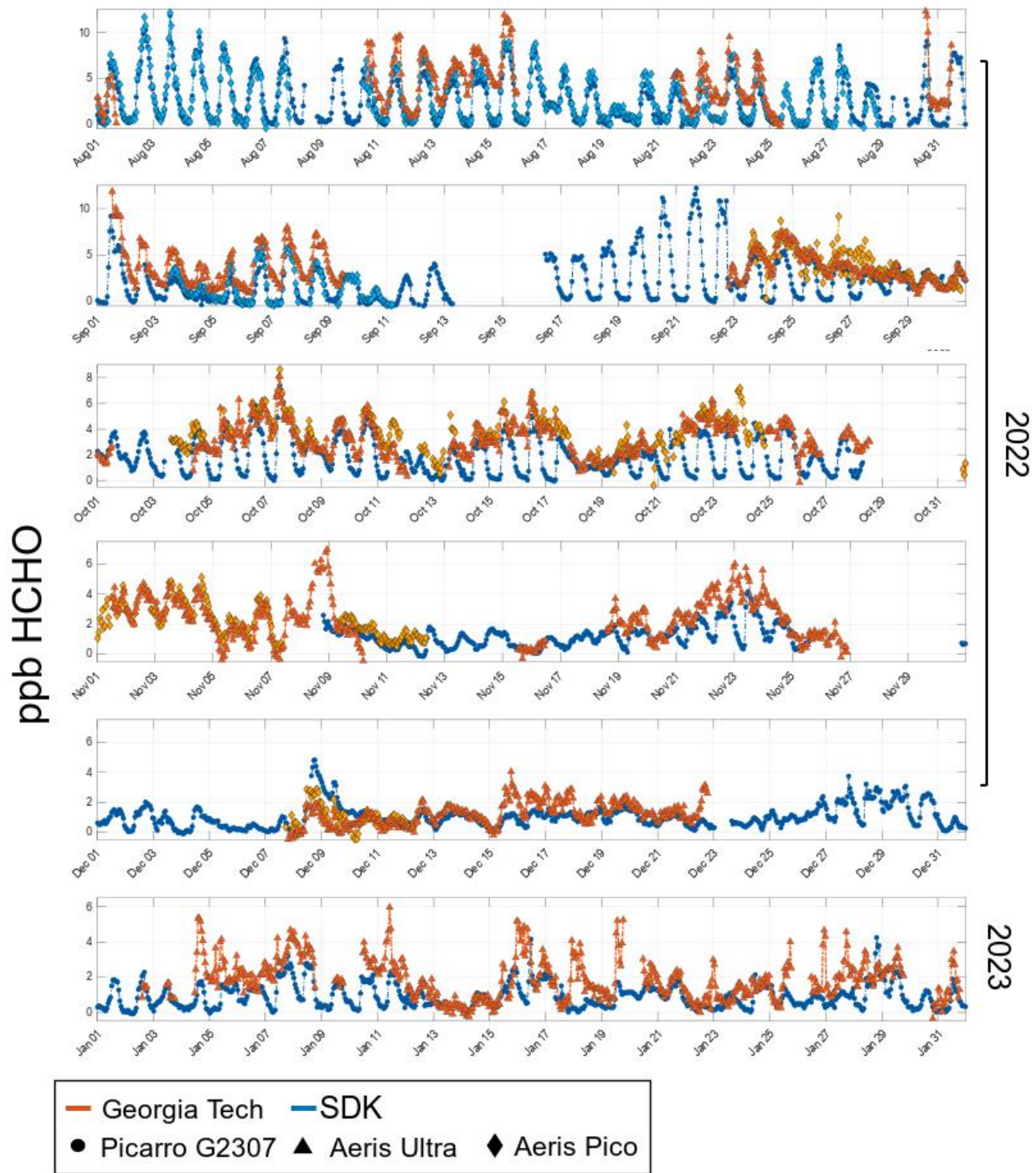


**Figure 3.10** 1 h averaged HCHO time series from Picarro G2307, Aeris Ultra, and Aeris Pico from Aug. 2022 through Jan 2023. Observations at GT show less defined diurnal amplitudes than the SDK site and are on average higher regardless of time of year. Aeris Pico data is sparse past 18 Oct. 2022 as it was periodically dedicated to other experiments.

In August, both sites reached their daily maximums around 13:00 LT with monthly averaged peaks of 7.76 ppb HCHO at GT and 6.38 ppb HCHO at SDK. On average, HCHO concentrations were 2.12 ppb higher than the SDK site, with 1 h maximums of 12.33 ppb at GT on 30 August and 11.86 ppb at SDK on 3 August. Measurements at GT generally had average nighttime minimums above 2 ppb in August and  $\leq 1$  ppb throughout the winter. Diel cycles showed less definition at GT as the year progressed into the colder months, with SDK maintaining comparatively clearer amplitudes that have sub-ppb nighttime minimums throughout the year. Given that the SDK site is located in a less urbanized area and immediately surrounded by trees, this trend matches results found in Wang et al. (2022), who noted that cities with higher levels of biogenic VOCs exhibited larger HCHO diurnal amplitudes. As such, we expect that the influence of isoprene chemistry on HCHO production is stronger at SDK. The consistent nighttime threshold at GT could result from a combination of anthropogenic, primary HCHO emission sources local to the city or possibly from stagnant atmospheric conditions leading to localized changes in nighttime surface layer mixing heights. Figure 3.10 spans a long enough time to capture the ambient extremes of the metropolitan area, showing that the observed HCHO gradient between the two sites is within the measurement capabilities of the G2307 and the Aeris instruments.

These data also allow for a snapshot comparison with previous measurements from both sites to quantify changes in HCHO concentrations. The only prior ground-based campaign to measure HCHO via a continuous monitor in the Atlanta metropolitan area was the 1999 Atlanta Supersite Project (Solomon et al., 2003), where a Hantzsch fluorometric monitor was deployed during the month of August (Dasgupta et al., 2005). HCHO observations taken in the urban core

are used to calculate an August diel cycle for their respective years. We employ the PAMS HCHO data taken at SDK in August 1999 (AQS, 1999) to compare them with the August 2022 data previously used in Figure 3.9. In 1999, DNPH samples were collected every 3 h from 06:00–18:00 LT. As stated previously, samples are now collected every 8 h over a 24 h period starting at 04:00 LT. As such, a 6 h average of the 1999 observations (12:00–18:00 LT) is compared with the 2022 8 h average (12:00–20:00 LT) with the results shown in Figure 3.11.

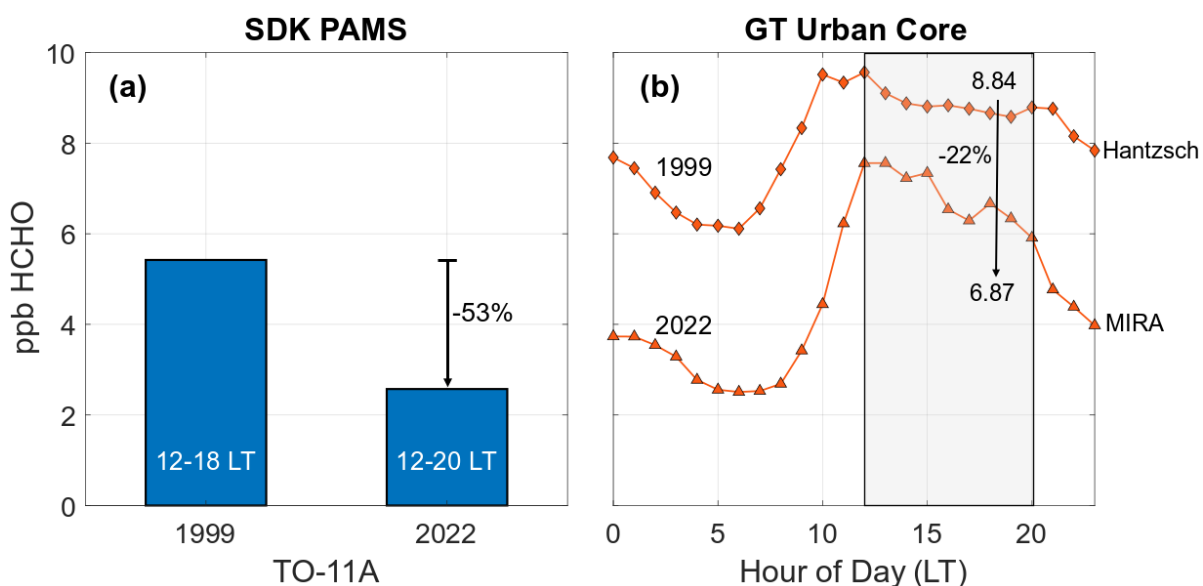


**Figure 3.11** HCHO concentrations from 1999 and 2022. (a) shows a 53% decrease from July 1999 to 2022 in the midday average (12-20:00 LT) of PAMS measurements taken at SDK and (b) shows a 22% decrease for the same averaging window in August in Atlanta’ urban core.

An average of the August HCHO observations over the 12:00–20:00 LT window shows that concentrations at GT have reduced by 22.3 % since 1999 despite the increasing urbanization of the city over the last 2 decades. The average relative decrease in the 1 h monthly maximums

and minimums at GT is 22.9 % and 59.0 %, respectively. Dasgupta et al. (2005) state the possible influence of nearby HCHO emission sources on their observations, but this remains a nonetheless considerable decrease in nighttime concentrations. A significantly greater midday decrease of 53 % is calculated for the SDK PAMS data. However, Picarro G2307 data averaged to the same midday window result in a relative decrease of only 1.9 %. Monthly averaged minimum values cannot be calculated for SDK as the 1999 data do not span a complete diurnal cycle.

Continuous measurements provide the benefit of comprehensive time series, meaning local chemical trends in HCHO can be more clearly related to time-dependent atmospheric conditions. In the urban core, maximum HCHO concentrations always occur in the daytime and minimums in the nighttime, with the relative change in minimums since 1999 being significantly greater than that of the maximums. OH oxidation of isoprene is one of the dominant sources of HCHO in urban environments that have sufficiently high NO<sub>x</sub> concentrations, with the southeast having comparably higher biogenic influences on its atmospheric chemistry than the rest of the country (Travis et al., 2016). As significant reductions in US NO<sub>x</sub> emissions have been observed over the decades (Duncan et al., 2016), urban daytime HCHO production is then expected to decrease. As OH is largely a daytime oxidant, nighttime decreases in HCHO are more likely attributable to reductions in direct emissions of both HCHO as well as its anthropogenic VOC precursors.

### **3.6 Conclusions**

We used yearlong ambient datasets from three commercially new in situ HCHO monitors to quantify instrument performance and to compare observations with measurements produced from co-located monitors employing the EPA TO-11A methodology. These continuous monitors offer an advantage given that their measurements are online, have sufficient precision at finer time resolutions, and do not require special handling or storage of samples or hazardous chemicals. However, previous measurements exhibited humidity dependencies, produced significantly lower concentrations, and showed non-negligible variability in HCHO concentration dependent on the zeroing method. Additionally, all three instruments require frequent zeroing via HCHO scrubbers to account for baseline drift, with each method presenting its own set of practical considerations. We determined calibration procedures and optimal field setups by assessing how measurements were impacted with the usage of four common scrubbing methods: DNPH, DR, DR + MS, and HO.

DNPH-derived baselines were compared to a ZA source, producing values within 14 ppt HCHO on average and demonstrating their efficacy. Ambient conditions year-round at the GT and SDK field sites had sufficient RH ( $\geq 25\%$ ) to not impede DNPH derivatization of hydrazine. At high RH ( $> 50\%$ ), no clear impact to instrument baselines could be observed. DR, DR + MS, and HO-scrubbed baselines were then compared to those resulting from DNPH. HO performed poorly, exhibiting a mean differential baseline value of 0.71 ppb HCHO. DR and DR+MS performed on par with DNPH, indicating high HCHO-scrubbing efficiency. As such, we recommend the use of DR/DR+MS and DNPH for zeroing the Picarro G2307 and only DNPH

for use with the Aeris units given their humidity requirements. Additionally, the G2307's humidity dependence was quantified experimentally. We emphasize this procedure before deployment as results here show this relationship to be instrument specific.

We developed a modified method for determining instrument precision that accounts for instrument zeroing. The G2307, Ultra, and Pico achieved modified precisions of 0.05, 0.20, and 0.22 ppb, respectively, for a 20 min integration time. We determined that the sensitivities of the monitors were stable during their respective deployments. The Aeris Ultra exhibited a NMB of -30 %–36 % compared to Aeris Pico and Picarro G2307 measurements if dynamic dilution calibrations were used as the basis. However, standard addition calibration of the Aeris units led to all instruments agreeing within 13 %. Co-located TO-11A observations exhibited a NMB of -52 % relative to the G2307, which is the largest TO-11A intercomparison discrepancy reported in the extant literature.

Finally, using time series that span August 2022 to January 2023 at two fields sites separated by 12 mi, we demonstrated that these instruments capture the HCHO gradient in the Atlanta metro area over a wide range of ambient conditions, including summer and wintertime seasonal extremes. Comparison with historical HCHO measurements revealed a relative decrease in daytime ambient HCHO of 22.3 % at the urban-core site and 53 % at the urban-rural site. Nighttime HCHO concentrations in the urban core decreased by 59 % during this time. Ultimately, the performance of these instruments and the subsequent results show the feasibility of both deploying across multiple cities and taking fast, accurate HCHO observations, offering the potential for greater insights into the complex chemistry of urban HCHO.

## CHAPTER 4

### INFORMING NEAR-AIRPORT SATELLITE NO<sub>2</sub> RETREIVALS USING PANDORA SKY-SCANNING OBSERVATIONS

#### 4.1 Introduction

Emissions of pollutants such as nitrogen oxides ( $\text{NO}_x = \text{NO} + \text{NO}_2$ ) and fine particulate matter (PM) from aircrafts, ground-support equipment, and airport-associated traffic negatively impact air quality and human health in near-airport communities (Quadros et al., 2020). By 2045, international full-flight aircraft  $\text{NO}_x$  emissions are projected to increase between 140 and 340% relative to 2015 levels as demand for air travel rises (Gössling and Humpe, 2020). Near-airport observations are needed to evaluate emissions inventories and track the impact of aviation on local air quality. Several studies have demonstrated the use of new high-resolution satellite retrievals of  $\text{NO}_2$  in top-down estimates of emissions from urban areas and point sources (Fioletov et al., 2021; Goldberg et al., 2022). While these and similar studies outline promising methods for monitoring co-located emissions, interpreting near-airport retrievals is complicated by horizontal heterogeneity and potential  $\text{NO}_2$  emissions aloft. Validation of satellite products is an essential first step towards using satellite-based observations as constraints on at-airport emissions.

Pandora spectrometer systems (SciGlob) are particularly useful for satellite validation efforts given the similar measurement approach to current satellite measurements, successful deployment during multiple field campaigns, and the growing international Pandonia Global Network. Total vertical column  $\text{NO}_2$  measurements from direct-sun (DS) measurements are of

high quality and have been used in a number of satellite validation studies intensives (Ialongo et al., 2020; Judd et al., 2020; Zhao et al., 2020; Verhoelst et al., 2021; Damiani et al., 2022; Lange et al., 2023). Subtraction of the stratospheric component determined from observations, models, or a fused model/observation component provide a DS tropospheric column that can be used for validation of satellite NO<sub>2</sub> tropospheric columns (Pinardi et al., 2020; Zhao et al., 2020; Verhoelst et al., 2021), and more generally to examine the evolution of surface-to-column NO<sub>2</sub> ratios throughout the day (Adams et al., 2023).

Pandoras can also operate in sky-scanning (sky) mode to measure sky-scattered solar radiation in the desired azimuth viewing direction. Analysis of sky spectra using multi-axis differential optical absorption spectroscopy produces independent tropospheric vertical column densities (VCDs) and vertical profile estimation below 3-4 km (depending on the aerosol properties and conditions). Compared to DS observations, sky observations have higher sensitivity to lower altitudes and are therefore well-suited for examining near-surface emissions. The lower sensitivity to NO<sub>2</sub> at high altitudes (> 3 km) means that tropospheric VCDs from sky measurements will often underestimate the full tropospheric VCD. While the Pandora sky tropospheric column products are relatively new compared to the DS products, prior work has shown good agreement with other MAX-DOAS and aircraft observations (Judd et al., 2020; Tirpitz et al., 2020; Lange et al., 2023) and strong correlation with DS-derived tropospheric VCDs (Pinardi et al., 2020). Products from sky scanning observations were evaluated during the CINDI-2 campaign and obtained the same features in the retrieved NO<sub>2</sub> vertical distribution with a comparable root mean square deviation to other, established MAX-DOAS algorithms (Frieß et al., 2019; Tirpitz et al., 2020).

Since 2018, the TROPospheric Ozone Monitoring Instrument (TROPOMI) aboard the Sentinel-5 Precursor satellite has provided daily NO<sub>2</sub> measurements with a flyover time of approximately 13:30 LT and a nadir spatial resolution of 3.5 x 5.5 km<sup>2</sup>. In polluted areas, the standard TROPOMI NO<sub>2</sub> VCD product typically exhibits negative biases compared to ground- or aircraft-based observations (Dimitropoulou et al., 2020; Ialongo et al., 2020; Judd et al., 2020; Verhoelst et al., 2021; Lange et al., 2023). Discrepancies are often attributed to the use of horizontally coarse chemical transport models (CTMs) for generating a priori vertical profiles used in calculating air mass factors (AMFs). However, even fine-resolution models may not accurately capture the complex meteorological conditions, magnitude and distribution of emissions, and plume dynamics that influence near-source NO<sub>2</sub> AMFs (Laughner et al., 2016; Judd et al., 2019; Silvern et al., 2019; Dang et al., 2023). Empirical NO<sub>2</sub> vertical profiles can be used to identify systematic biases in the CTMs that are used to generate AMFs. Additionally, the use of empirical profiles in AMF calculations allows for evaluation of satellite products unaffected by CTM biases.

Launched in 2023, the TEMPO (Tropospheric Emissions: Monitoring of Pollution) instrument provides hourly daytime NO<sub>2</sub> retrievals at a resolution of 2.1 x 4.4 km<sup>2</sup> (Zoogman et al., 2017). A priori profiles from TEMPO retrievals are informed by the GEOS-CF (Global Earth Observing System Compositional Forecast) CTM, which operates at a horizontal resolution of 25 x 25 km<sup>2</sup> (Keller et al., 2021). Vertical profiles from GEOS-CF and the related GEOS-Chem CTM have been shown to be particularly sensitive to modeled boundary layer heights and chemical mechanisms (Oak et al., 2019; Dang et al., 2023; Shah et al., 2023; Yang et al., 2023).

This study uses Pandora-1S and TROPOMI observations near the Atlanta-Hartsfield Jackson airport (ATL), the world's busiest airport (Jersey, 2021), to examine the impact of aviation on NO<sub>2</sub> vertical profiles, and to demonstrate the benefits of using Pandora sky observations to calculate AMFs. Using TROPOMI data and a statistical plume-fitting approach, Fioletov et al. (2021) estimated NO<sub>x</sub> emissions from ATL to be 5.1-6.4 kt yr<sup>-1</sup> for 2018-2019, which is 40-73% higher than the 2017 EPA NEI estimate of 3.7 kt yr<sup>-1</sup>. The same study estimated a 55% decline in airport emissions during the periods where passenger flights were down 75% and cargo down 25% due to the COVID-19 pandemic. Our observations span a similar COVID-impacted timeframe, from April 2020 – May 2021, and provide a unique ground-based perspective and useful point of comparison for satellite-based assessments.

In section 4.3.1, we use time series to demonstrate how changes in NO<sub>x</sub>-source activities impacted Pandora and TROPOMI VCDs. In section 4.3.2, we describe the Pandora DS and sky products and the impact of viewing geometry on agreement between measurements. In section 4.3.3, we compare tropospheric VCDs derived from these datasets. In section 4.3.4, we compare Pandora sky and GEOS-CF vertical profiles and the impact of aviation on NO<sub>2</sub> concentrations aloft. In section 4.3.5, we evaluate TROPOMI tropospheric NO<sub>2</sub> VCDs with Pandora sky and DS retrievals, using either GEOS-CF or empirically based a priori profiles in AMF calculations. We conclude with a discussion of the benefits and limitations of using TROPOMI observations for evaluation of CTM columns and emissions estimates for aviation and similarly complex urban sources.

## **4.2 Materials and methods**

### **4.2.1 Pandora observations**

The Pandora system is originally described in Herman et al. (2009). Briefly, the instrument optical sensor head collects photons in a narrow field-of-view (FOV =  $1.5^\circ$  at full width at half maximum for sky and  $2.6^\circ$  for DS), which are then transmitted through a fibreoptics cable (single core,  $400\ \mu\text{m}$  in diameter) to a medium spectral resolution spectrometer (0.6 nm per full width at half maximum). Solar spectra in the range of 280-525 nm are measured at varying integration times (2.5 msec to 4 sec) and averaged to improve the signal-to-noise ratio (Herman et al., 2019). The sensor head is mounted on a two-axis positioner which allows for observations in DS and sky geometries.

Two Pandora spectrometer instruments (Pandora 158 and 168, SciGlob, Ltd) were deployed at the Georgia Environmental Protection Division Air Protection Branch offices, located 1.2 km east of the ATL runways (Figure 4.1), with an altitude above sea level of 291 m. Measurements began on 16 April 2020 and continued through 16 May 2021. Pandora 158 operated in DS mode while Pandora 168 alternated between DS and sky modes. Viewing azimuth angles (VAA) for sky observations targeted the urban background (VAA =  $20.5^\circ$ ), the airport runways (VAA =  $262^\circ$ ), and the terminal (VAA =  $273^\circ$ ). Viewing zenith angles (VZA) of  $2^\circ$ ,  $50^\circ$ ,  $60^\circ$ ,  $65^\circ$ ,  $70^\circ$ ,  $75^\circ$ ,  $80^\circ$ ,  $81^\circ$ ,  $82^\circ$ ,  $83^\circ$ ,  $84^\circ$ ,  $85^\circ$ , and  $86^\circ$  were used for all ATL-facing scans. For background scans, the lowest VZA was  $85.5^\circ$  and were otherwise the same.

The Pandora's line of sight for each VAA is shown in Figure 4.1. Sky scanning lines of sight are the horizontally projected optical path lengths calculated by BlickP averaged over the full deployment period. They extend 11.4 km out from the instrument location. DS optical path lengths are colored by local time of day and are capped to the sky scanning mean optical path length for visual clarity (DS path lengths are longer as their light source is more intense). DS VAAs start each day in the east, closer to the background direction, and end closer to the airport-facing direction. When VAAs of DS and sky measurements are most similar, the DS VZA is large ( $\geq 70^\circ$ ).

DS measurements were taken with integration times of 2.5 ms to 4 s and had a total measurement duration of 40 s. Sky measurements had an integration time of 200-300 ms (averaging over  $\leq 20$  sec). This produces DS measurements from P168 averaged to a 1 min resolution and sky observations averaged over 7.5 min that occurred at each direction approximately every 30 minutes. Urban background absorption spectra were measured with an open filter wheel setting. There is an assumption that the air is heterogeneous between different azimuth directions within the remote sensing sampling volume (average photon path distance). Solar spectra were measured over ATL with a U340 optical filter (to reduce stray light in UV due to photons with wavelengths  $> 385$  nm) and without filters.

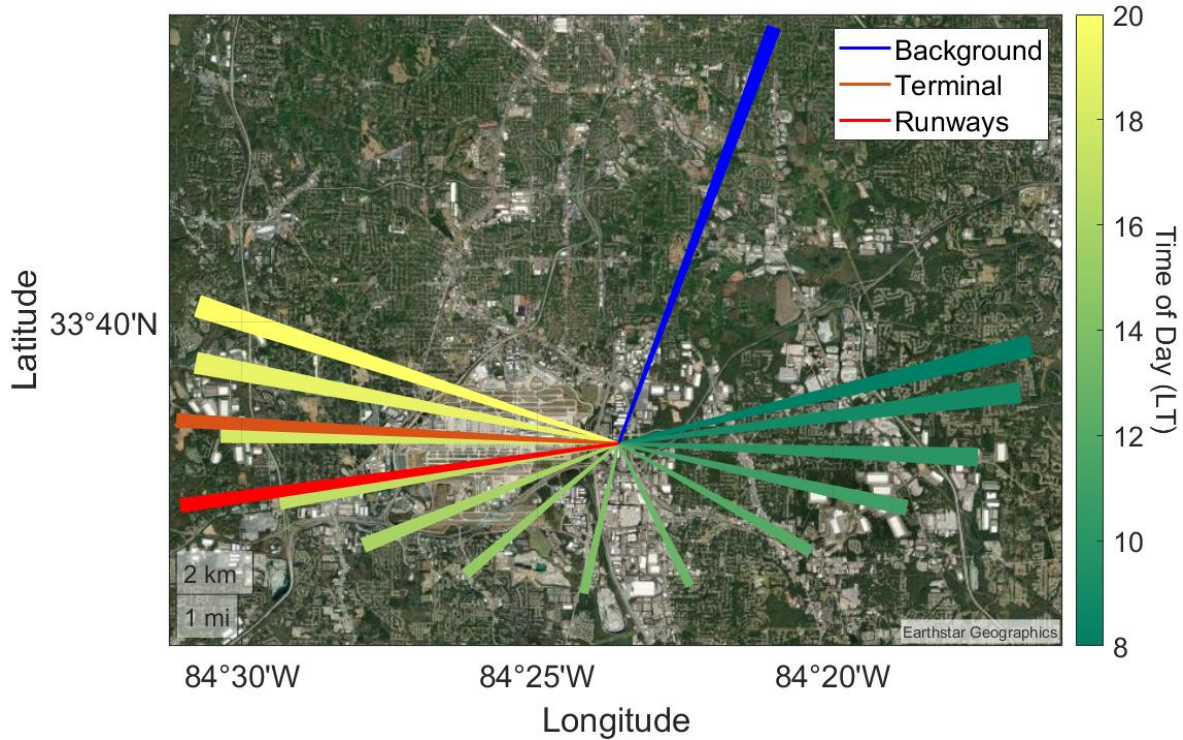


**Figure 4.2** Pandora DS and sky scanning azimuth viewing directions. Line segments originate at the ground site and extend to the mean sky scanning optical path length (11.4 km). DS lines of sight are colored by local hour of day and are capped to the same optical path length as sky scanning measurements for purpose of clarity. FOVs for sky scattered ( $FOV = 1.5^\circ$ ) and DS ( $FOV = 2.6^\circ$ ) are used to show a 2D projection of the Pandora’s conical views. Base map from Esri World Imagery (Esri).

The standard Pandora sky viewing routine scans include measurements from the zenith to the lowest elevation angle, and back to the zenith at a single VAA, forming a “V-shape” in time. For runway and terminal VAAs, we scanned from zenith to the lowest level at one VAA, changed VAAs, and then scanned from the lowest angle to zenith. This allowed for greater measurement frequency. This viewing schedule is non-standard and required post-processing of

the Pandora-generated L0 sky data for compatibility with the BlickP processing software. To create the requisite VZA symmetry, each vertical scan was duplicated to mimic the anticipated viewing pattern. While BlickP codes require observations at  $VZA > 87^\circ$ , the tree line obscured the line of sight at  $VZA > 86^\circ$ . We added artificial spectra at the expected VZAs of  $88^\circ$  and  $89^\circ$  but did not use them in the actual profile estimation. The lowest pointing angle ( $VZA = 86^\circ$ ) provided an average concentration within the lowest layer.

All spectra were processed using the BlickP software. Details of BlickP and r-codes can be found in the developer's data products document (Cede, 2021). Total VCDs from DS measurements were obtained using BlickP v1.7.22 r-code "nvs3", which uses the solar irradiance measured in the visible range of 400-440 nm. Updates in Blick v1.8 are expected to have negligible impact on the total column product (which mainly result from the temperature treatment of molecular absorption cross section). Retrievals of tropospheric and partial VCDs from sky measurements were obtained using BlickP v1.8.50 with r-code "nuh1", (290-380 nm fitting window). We assign measurement uncertainties using the absolute uncertainties calculated by BlickP ("total" uncertainty for total VCDs, "independent" uncertainty for tropospheric VCDs). A detailed description of the uncertainty budgets can be found in Spinei et al. (2020) and Cede (2021).

For all Pandora datasets, we remove observations with solar zenith angles  $> 75^\circ$ , spectral fitting normalized rms weighted by uncertainty ( $wrms$ )  $> 0.0018$  (approximately twice the median  $wrms$  in both geometries), and relative uncertainty  $> 15\%$ . We note that these criteria likely do not screen all cloud-affected measurements which generally exhibit greater uncertainty

(Wagner et al., 2014). We find that using highly restrictive data screening criteria ( $wrms > 0.001$ , relative uncertainty  $> 5\%$ ) does not significantly affect the outcome of the results presented in this work. DS retrievals from the two Pandora instruments are well correlated ( $r = 0.98$ ).

Throughout this work, normalized mean difference (NMD) is used as a comparison metric. It is defined here as:

$$NMD = \frac{\sum(Y-X)}{\sum X} \quad (4.1)$$

where  $Y$  is any quantity relative to  $X$ , which is the point-of-comparison quantity. Pandora DS VCDs have a NMD of 2.4% which is deemed negligible enough that we therefore combine direct sun observations from both instruments into a single dataset.

#### **4.2.2 TROPOMI retrievals**

We use the offline level 2 v2.4 TROPOMI NO<sub>2</sub> tropospheric and stratospheric products (van Geffen et al. 2022) accessed at NASA's Goddard Earth Sciences Data and Information Services Center (GES DISC, <https://tropomi.gesdisc.eosdis.nasa.gov/>). Data is filtered to exclude pixels with cloud fractions greater than 0.3, solar zenith angles greater than 60°, and quality flag ( $qa\_value$ ) less than 0.5. The VCD error provided in the product is taken as the measurement uncertainty.

This TROPOMI product uses TM5-MP modeled slant columns to separate its NO<sub>2</sub> total slant columns into their stratospheric and tropospheric components. The TM5-MP model also

provides the a priori vertical profiles used in the calculation of the TROPOMI tropospheric AMF ( $AMF_{TM5-MP}$ ). The procedure for updating AMFs based on alternative vertical profiles is outlined in Eskes et al. (2022), which follows the approach of Palmer et al. (2001), shown in eqn. 4.2.

$$AMF_{new} = AMF_{TM5-MP} \times \frac{\sum_l AK_l \times x_{new}}{\sum_l x_{new}} \quad (4.2)$$

where  $AK_l$  is the averaging kernel at level  $l$  (provided in the TROPOMI product), and  $x_{new}$  is the partial column in layer  $l$ . In this work, we use vertical profiles from GEOS-CF and a fused GEOS-CF/Pandora product to generate alternative AMFs for our TROPOMI evaluations. This procedure is described in the following section.

### 4.2.3 AMFs from GEOS-CF and fused GEOS-CF/Pandora profiles

GEOS-CF v1 model outputs (Keller et al., 2021) are used to replace a priori vertical profiles in the TROPOMI product, to perform stratospheric separation for Pandora DS observations, and as a point of comparison with observed vertical profiles. The model is run on a cubed-sphere c360 horizontal resolution. The 72 hybrid-eta vertical grid results in a lower layer depth of approximately 130 m agl and a total of 14 model levels below 2 km agl. Anthropogenic  $NO_x$  emissions are from HTAP v2.2, which includes US EPA estimates of aircraft emissions around the airport below 3000 ft (914 m), treated as a ground-level point source (Janssens-Maenhout et al., 2015). Emissions are not adjusted for decreases in activity associated with the COVID-19 pandemic.

All TROPOMI retrievals shown in this work use AMFs generated from GEOS-CF vertical profiles ( $AMF_{GEOS-CF}$ ) unless otherwise noted. TROPOMI pixels are matched to the GEOS-CF hourly-averaged 36-level replay output according to shortest distance between pixel and grid center points, and time bin containing the TROPOMI observation. Vertical remapping of GEOS-CF  $NO_2$  mixing ratios to TROPOMI scattering heights is performed assuming an exponential relationship between  $NO_2$  number density and pressure.

We find that at the location of the Pandora instruments,  $AMF_{GEOS-CF}$  are well-correlated with  $AMF_{TM5-MP}$  ( $r = 0.70$ ) but are significantly lower with a NMD of -18.8%. Use of  $AMF_{GEOS-CF}$  increased TROPOMI  $NO_2$  VCDs at the location of the Pandoras by 25.4% compared to the original product. These results are anticipated given findings from prior studies that saw tropospheric VCD increases of 10-30% when using profiles from higher resolution CTMs ( $\geq 0.1^\circ \times 0.1^\circ$ ) to calculate alternative TROPOMI AMFs for retrievals measured over urban areas (Douros et al., 2023; Pseftogkas et al., 2022).

We use Pandora sky vertical profiles to produce an observation/model fused AMF ( $AMF_{Fused}$ ). Figure 4.2 provides an example of this procedure using profiles from 22 Mar. 2021. For each TROPOMI overpass, we collect Pandora sky observations within 30 min of the overpass time which includes 2 vertical profiles per satellite observation. The concentration derived from the measurement taken closest to the horizon ( $VZA = 86^\circ$ ) is assumed to be constant down to the surface. Surface layer concentrations are expected to have high uncertainty, but the corresponding TROPOMI averaging kernels (AKs) are smallest here and therefore have

the least impact on  $AMF_{Fused}$  (discussed further in section 4.3.3). These profiles are then interpolated to the GEOS-CF  $NO_2$  layer heights assuming a linear relationship between mixing ratio and pressure (shown in grey). Following Dimitropoulou et al. (2020), we calculate a daily median from these profiles (gold) to limit any instabilities in individual profile retrievals and replace the GEOS-CF  $NO_2$  vertical profile at the corresponding layer heights. The portion of the GEOS-CF profile to be replaced is shown as the red profile with circle markers. This approach incorporates daily profile variation when recalculating AMFs which (Laughner et al., 2016) demonstrated the benefits of. At altitudes where Pandora measurements are not available ( $> 3$  km agl), the original GEOS-CF profile is preserved (shown as the red profile with square markers). These new GEOS-CF/Pandora-fused shape profiles are used to generate  $AMF_{Fused}$  using eqn. (4.2).

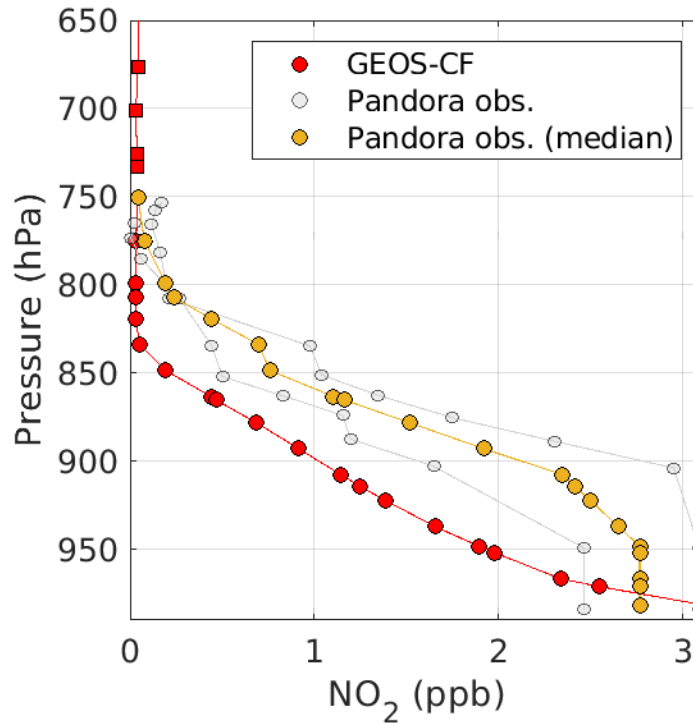


**Figure 4.2** Example of vertical profiles measured over the ATL runways on 22 Mar 2021.

Pandora observations have been interpolated to the GEOS-CF layer heights and are shown in grey. The resulting median profile used to partially replace the GEOS-CF profile is shown in gold. The replaced portion of the GEOS-CF profile is marked with circles and the segment that is unaltered is marked with squares.

#### 4.2.4 Pandora DS troposphere/stratosphere separation

We generate GEOS-CF/TROPOMI fused stratospheric VCDs from the hourly-averaged replay product using an approach similar to that described in Adams et al. (2023). A polynomial equation is used to describe the hourly variation of stratospheric  $\text{NO}_2$  in the grid box containing the Pandora instrument over a 7-day moving average window. We apply the polynomial fits to

the time point of Pandora DS observations to generate stratospheric VCDs on the same time basis as our observations. We then calculate the daily average ratio of TROPOMI stratospheric NO<sub>2</sub> VCD observations to GEOS-CF modeled values. Gaps in the daily average ratio caused by gaps in TROPOMI data availability are linearly interpolated. The modeled stratospheric time series is multiplied by the daily average ratio to provide the GEOS-CF/TROPOMI fused stratospheric VCD. We find adjustments are typically minor (average TROPOMI/GEOS-CF stratospheric VCD ratio at the Pandora location =  $0.97 \pm 0.07$ ). This model/observation fused stratospheric VCD is subtracted from the Pandora DS total NO<sub>2</sub> VCD to produce a Pandora DS tropospheric VCD.

#### **4.2.5 Pandora-TROPOMI comparison approach**

Two Pandora datasets are either compared or combined with TROPOMI observations: the DS Pandora tropospheric VCDs and the Pandora sky tropospheric VCDs. For the DS comparison, all Pandora observations within 10 min of TROPOMI overpass are averaged, with each Pandora observation weighted by the inverse of the reported total column measurement uncertainty. One datapoint is made for each TROPOMI observation that includes the Pandora location in its footprint.

For sky observations, spatial coincidence is determined using the method described in Dimitropoulou et al. (2020). For each VAA, we combine observations within 30 min of the TROPOMI overpass time. We draw a horizontal line segment in the direction of the VAA

extending 5 km from the instrument location. This path length was chosen on the assumption that measurements made in UV are more representative of NO<sub>2</sub> absorption within distances that are closer to and along the line of sight of the instrument. Sinreich et al. (2013) show that the probability of scattered photons reaching the instrument decreases exponentially with distance. Given the proximity of ATL to the instruments and that its area contains approximately 5 km of the Pandora line of sight for the runway and terminal directions, NO<sub>2</sub> absorption beyond this distance is assumed to contribute negligibly. We produce a TROPOMI super-observation by combining the pixels through which the line segment traverses and weighting each TROPOMI pixel by the fraction of the line segment it contains. As in the DS comparisons, one sky datapoint is made for each corresponding TROPOMI super-observation.

#### **4.2.6 Separation of high and low travel periods**

To examine the impact of aviation on our analysis, we identify two periods with similar meteorology, but varying levels of reported departures. Meteorological data are from an Automated Surface Observing System unit located at ATL (accessed at <https://mesonet.agron.iastate.edu/ASOS/>). The reported number of departures was manually recorded from [www.flightradar24.com](http://www.flightradar24.com), accessed daily during the observation period. While the departure data does not encompass every flight, the relative change in observed departures is a relevant proxy for our analysis.

Figure 4.3 shows the resurgence in aviation after Spring 2020, and the time periods selected for comparison throughout our analysis. We select 16 April – 31 May 2020 as our period of low aviation-related activity, with flightradar24 reporting an average of 295 departures per day. We identify 18 March – 16 May 2021 as a meteorologically similar period with a much higher number of average daily departures (958). For simplicity, we refer to these periods as “April-May 2020” and “April-May 2021” in subsequent analysis. TROPOMI retrievals show a decrease in tropospheric NO<sub>2</sub> VCDs throughout the entire Atlanta region during the April-May 2020 period (Figure 4.4). In the following sections, we discuss specifically the NO<sub>2</sub> in the airport hot spot where the Pandora is located, and the impact of AMF calculations on this analysis.

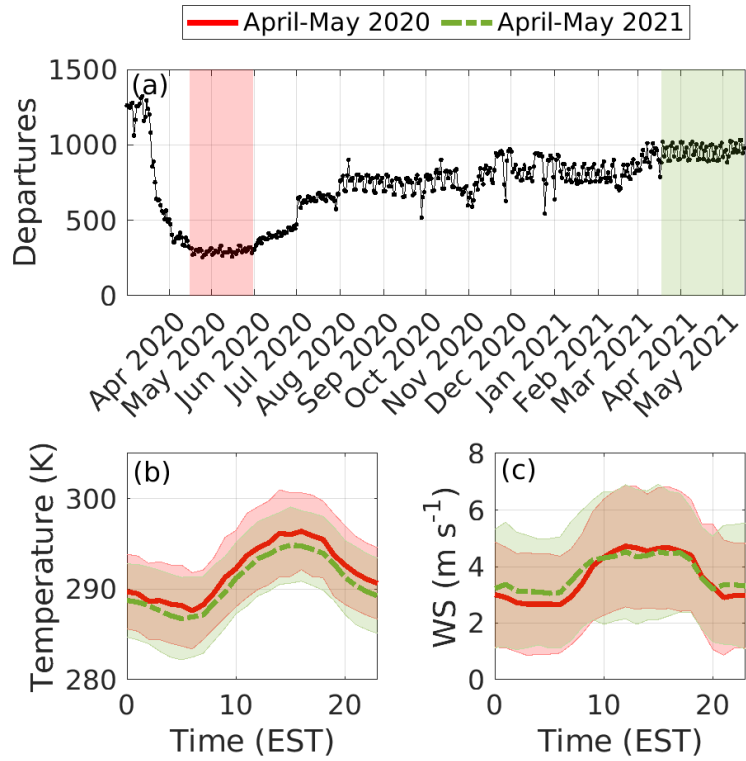


**Figure 4.3** (a) Daily departures from ATL reported by Flightradar24.com. Shaded segments represent selected periods of high and low aviation-related activity with similar (b) temperature and (c) windspeeds. Shaded regions in (b) and (c) represent the standard deviation of the observations.

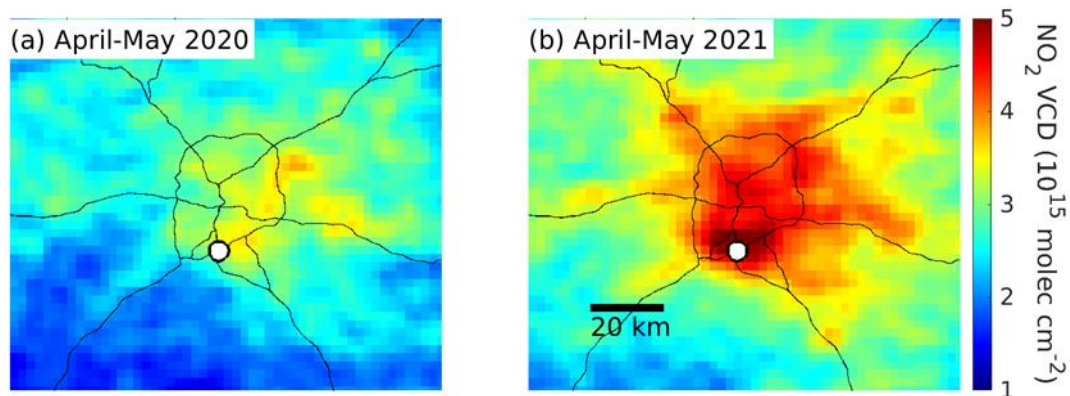


**Figure 4.4** TROPOMI tropospheric NO<sub>2</sub> VCDs for periods of (a) low and (b) high aircraft departures from ATL. VCDs have been oversampled to 0.02° using the method described in Sun et al. (2018). Lines denote major highways. The white circle is the measurement site.

## **4.3 Results and discussion**

### **4.3.1 NO<sub>2</sub> VCD variability**

Time series for the full deployment period are plotted to demonstrate how changes in airport and traffic activity impacted DS and TROPOMI tropospheric VCDs (Figure 4.5). TROPOMI VCDs are recalculated using  $AMF_{GEOS-CF}$ . Monthly midday median VCDs and their absolute deviations (MAD) are shown for DS and TROPOMI VCDs. DS medians and MADs are calculated using data only from the TROPOMI overpass window (12-14 LT). Three periods of interest are delineated: periods A and C are April-May 2020 and April-May 2021. Period B spans the month of July 2020, which exhibits an overnight increase of >154 daily departures on the first of the month.

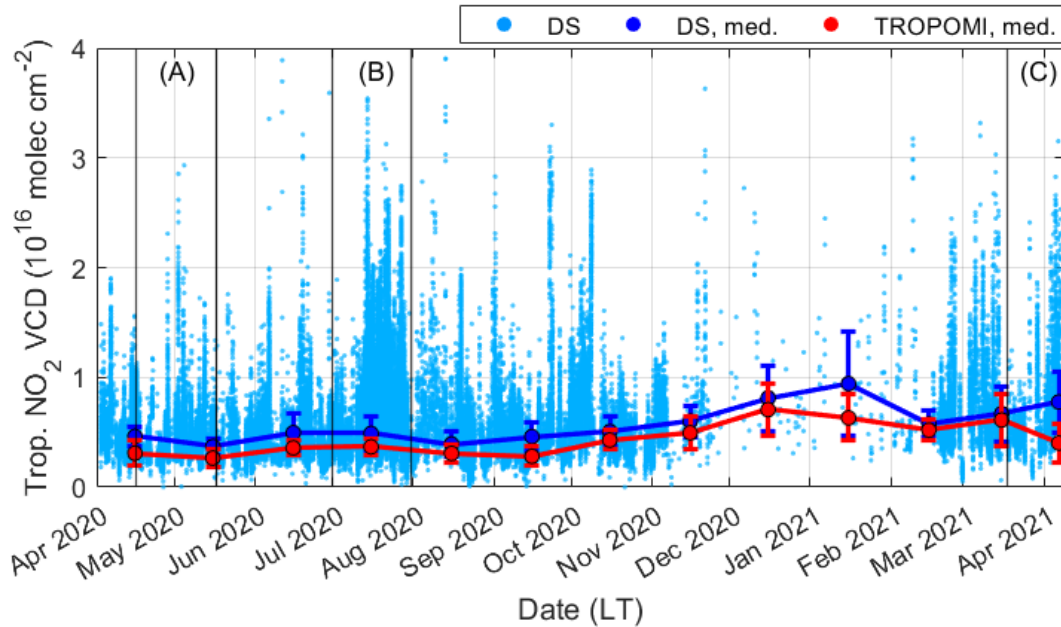


**Figure 4.5** DS and TROPOMI tropospheric NO<sub>2</sub> VCDs for the full deployment period. Monthly median VCDs are plotted for DS (blue) and TROPOMI (red) using data only from the TROPOMI overpass window (12-14 LT). Error bars are MADs. Three periods are delineated: (A) April-May 2020, (B) 1-31 July 2020, and (C) April-May 2021.

Period A exhibits the lowest values and variability in VCDs with median DS and TROPOMI tropospheric VCDs of  $(4.2 \pm 1.0) \times 10^{15}$  molec cm<sup>-2</sup> and  $(2.7 \pm 0.9) \times 10^{15}$  molec cm<sup>-2</sup>, respectively. During this period, urban on-road traffic counts were 50% lower than in 2019 (Huang et al., 2021) with a monthly average of  $1.3 \times 10^5$  counts (data from Georgia Department of Transportation, station 063-1192). Daily departures declined by 78% from the month prior (Figure 4.3). For period B, traffic volume plateaued (monthly average of  $1.6 \times 10^5$  counts, increase of 26% from period A), returning to business-as-usual levels. Daily departures increased by 117% relative to period A to a monthly average of 641 counts. Monthly median and MADs

for DS and TROPOMI VCDs increased to  $(4.9 \pm 1.5) \times 10^{15}$  molec cm<sup>-2</sup> and  $(3.7 \pm 0.7) \times 10^{15}$  molec cm<sup>-2</sup>, respectively, which correspond to increases of 17% and 37%. We note that meteorological conditions have not been accounted for in these comparisons. Goldberg et al. (2022) determined that meteorology was favorable for low NO<sub>2</sub> during spring 2020, so relative changes here may be exacerbated.

VCDs and variability are comparably greater for period C with median DS and TROPOMI tropospheric VCDs values of  $(6.1 \pm 1.9) \times 10^{15}$  molec cm<sup>-2</sup> and  $(4.6 \pm 1.7) \times 10^{15}$  molec cm<sup>-2</sup>, respectively. As atmospheric conditions between time periods were similar, increases in air and vehicle traffic are considered the dominant driver in column variability and led to relative increases in median VCDs of 45% (DS) and 71% (TROPOMI). The relative change in TROPOMI VCDs in this work is significantly higher than what has been reported in prior studies, which determined decreases in tropospheric NO<sub>2</sub> over ATL from 2019 to 2020 of 33-50% during spring (Goldberg et al., 2020; Fioletov et al., 2021; Huang et al., 2021). As these studies used VCDs with AMF<sub>TM5-MP</sub>, the higher relative change in VCDs in this work is attributed to use of AMF<sub>GEO5-CF</sub>.

Midday DS and TROPOMI monthly medians trend similarly throughout deployment. Both reach their minimums in May 2020 (DS:  $(3.7 \pm 0.8) \times 10^{15}$  molec cm<sup>-2</sup>, TROPOMI:  $(2.6 \pm 0.8) \times 10^{15}$  molec cm<sup>-2</sup>) and maximums during December 2020 – January 2021 (DS:  $(9.4 \pm 4.7) \times 10^{15}$  molec cm<sup>-2</sup>, TROPOMI:  $(7.1 \pm 2.4) \times 10^{15}$  molec cm<sup>-2</sup>). Daily departures continue to increase after winter but VCDs remain in a similar range, showing that the seasonal decrease in photoactive radiation significantly enhanced NO<sub>2</sub> lifetime. Midday variability is also greatest

during this period, though we note that DS MADs may be artificially inflated as observations are sparser.

### 4.3.2 Impact of Pandora viewing geometry on sky columns

Pandora sky observations produce tropospheric columns that differ from DS observations for at least two reasons. The first is that DS and sky observations typically have different horizontal footprints (measurement direction and measurement surface projection, Figure 4.1). In Figure 4.6a, we compare DS and sky tropospheric VCDs under all viewing directions. The datasets correlate well with an  $r = 0.68$ . Sky observations are systematically lower than DS observations. A York regression (York et al., 2004) (weighted using the uncertainties described in section 4.2.1) produces a slope of  $0.69 \pm 0.001$  with an offset of  $(0.90 \pm 0.01) \times 10^{15}$  molec  $\text{cm}^{-2}$ . Sky tropospheric VCDs exhibit a NMD = -10.7% relative to the DS VCDs. This compares closely with prior radiative transfer simulations which reported sky scanning VCDs to be 12% lower than DS VCDs. These results are anticipated as sky measurements are more representative of the planetary boundary layer (PBL) and thus do not capture  $\text{NO}_2$  in the upper troposphere (Pinaridi et al., 2020; Tirpitz et al., 2020).

Pinaridi et al. (2020) performed a similar comparison for three different polluted cities, but calculated slopes greater than unity and intercepts that were negative. These discrepancies likely result from the different techniques used to apply a stratospheric correction to the DS data. Tropospheric VCDs reported in this work are less than or similar to those measured in the other

cities of study (Xianghe, Beijing, and Thessaloniki), which suggests the PBL for the Atlanta area is less polluted. In more polluted regions, a greater amount of  $\text{NO}_2$  resides in the PBL, decreasing the contribution of upper tropospheric  $\text{NO}_2$  to the full tropospheric column. The sub-unity slope in this work indicates that free tropospheric  $\text{NO}_2$  contributes significantly to the full tropospheric column for the Atlanta area.

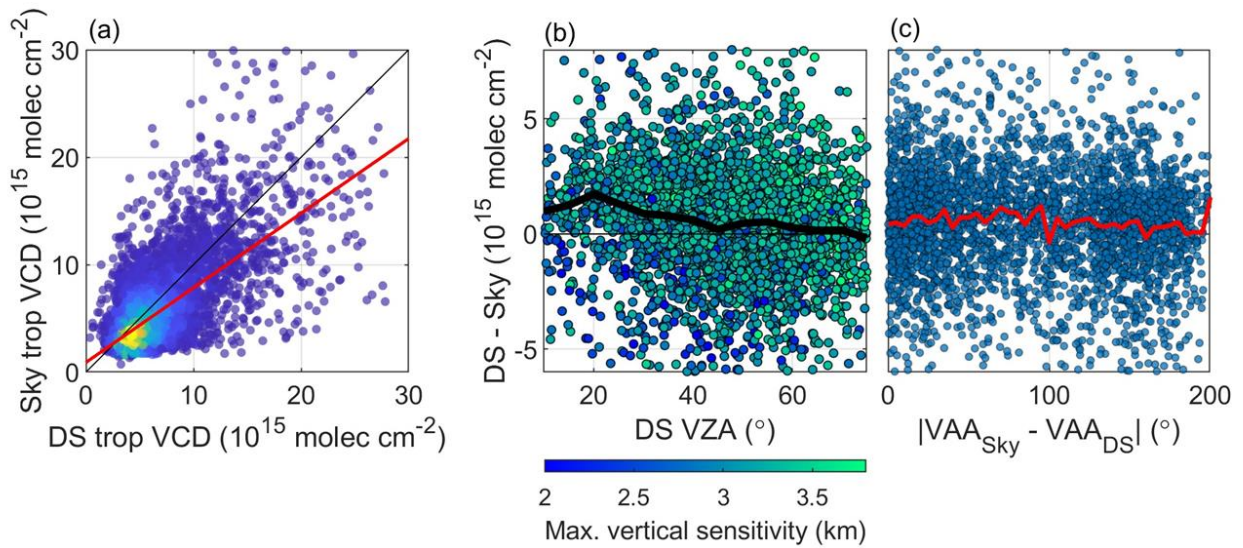


**Figure 4.6** DS and tropospheric VCDs from entire deployment period. (a) compares sky and DS tropospheric VCDs. Red line is determined via York regression using “total” uncertainty for DS and “independent” uncertainty for sky VCDs. Data beyond the x and y range of the figure are not shown for clarity. (b) shows the difference between DS and sky tropospheric VCDs as a function of the DS VZA. Black line is the median VCD difference binned in  $5^{\circ}$  increments. (c) shows the difference in DS and sky VCDs (runway and terminal directions) as a function of the RAA. Red line is the median VCD difference binned in  $5^{\circ}$  increments.

Differences between DS and sky observations are also found to reflect differing vertical sensitivities. Figure 4.6b shows the differences between DS and sky tropospheric VCDs as the DS VZA increases. These points are colored using the max vertical distance of the Pandora line of sight as a proxy for vertical sensitivity. The median difference at progressing DS VZAs shows a declining trend while the vertical sensitivity typically increases. As the DS VZA increases, DS vertical sensitivity towards tropospheric concentrations increases, and more closely approximates that of the sky viewing geometry.

Given our sky viewing geometry, ATL-facing measurements with small relative-to-sun azimuth angles ( $RAA = |VAA_{sky} - VAA_{DS}|$ ) would be expected to agree better with DS columns as both VAAs and VZAs are similar (background RAAs are always large). Figure 4.6c shows the difference in DS and sky VCDs (runway and terminal-facing) as a function of RAA. Median VCD differences are shown in red and do not exhibit a systematic relationship with RAA. This is attributed to two reasons: (1) Sky measurement integration times are two orders of magnitude longer than those of DS measurements. Light intensity increases as the instrument measures closer to the sun ( $RAA \leq 30^\circ$ ) which can induce a “smearing effect” (Park et al., 2019) and bias the resulting VCDs. Measurements over ATL (which had westward-facing VAAs) could be subject to this in the afternoon. (2) even at small RAAs, high urban  $NO_2$  heterogeneity causes DS and sky geometries to not observe the same plume.

### 4.3.3 Impact of aviation on NO<sub>2</sub> tropospheric VCDs and vertical profiles

The differences between NO<sub>2</sub> tropospheric column densities measured over the airport reflect the prevailing wind patterns and the amount of airport activity (Figure 4.7). In both 2020 and 2021, enhancements over ATL are greatest when winds are westerly, and the background viewing direction is not influenced by emissions near ATL. Easterly and northeasterly winds transport near-airport emissions over the background viewing direction, leading to higher NO<sub>2</sub> over the background than the airport. In April-May 2021, ATL enhancements are greater, with a mean increase from  $1.88$  to  $2.86 \times 10^{15}$  molec cm<sup>-2</sup> and an increase in daily median maximums from  $2.49$  to  $4.42 \times 10^{15}$  molec cm<sup>-2</sup>. This is primarily attributed to the increase in aviation relative to 2020, though increases in vehicle most likely contributed as well. Background enhancements show a smaller mean enhancement increase of  $1.49$  to  $1.68 \times 10^{15}$  molec cm<sup>-2</sup> for the same periods.

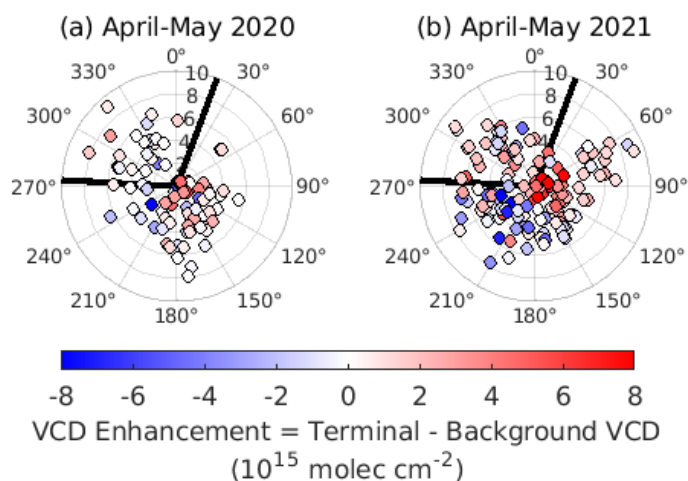


**Figure 4.7** Midday (11-14 EST) enhancement of tropospheric VCD over ATL measured by Pandora sky observations as a function of windspeed and wind direction. Solid lines represent

the VAA over the background ( $20.5^\circ$ ) and terminals ( $273^\circ$ ) under periods of (a) low and (b) high aviation.

To examine the impact of aviation on  $\text{NO}_2$  vertical profiles, we isolate periods when Pandora sky observations are larger in the airport-viewing direction compared to the background, with the measured enhancement at least 3 times greater than measurement uncertainty. Figure 4.8 shows median observed vertical profiles (excluding the estimated surface layer) binned in 150 m altitude increments at different times of day for this subset of data. Points greater than 3 times the MAD of each bin are excluded. We show the background and terminal azimuth viewing angles only, as runway and terminal measurements produced similar profiles. The MADs for terminal and background-facing measurements are similar and are only plotted for the terminal profile.

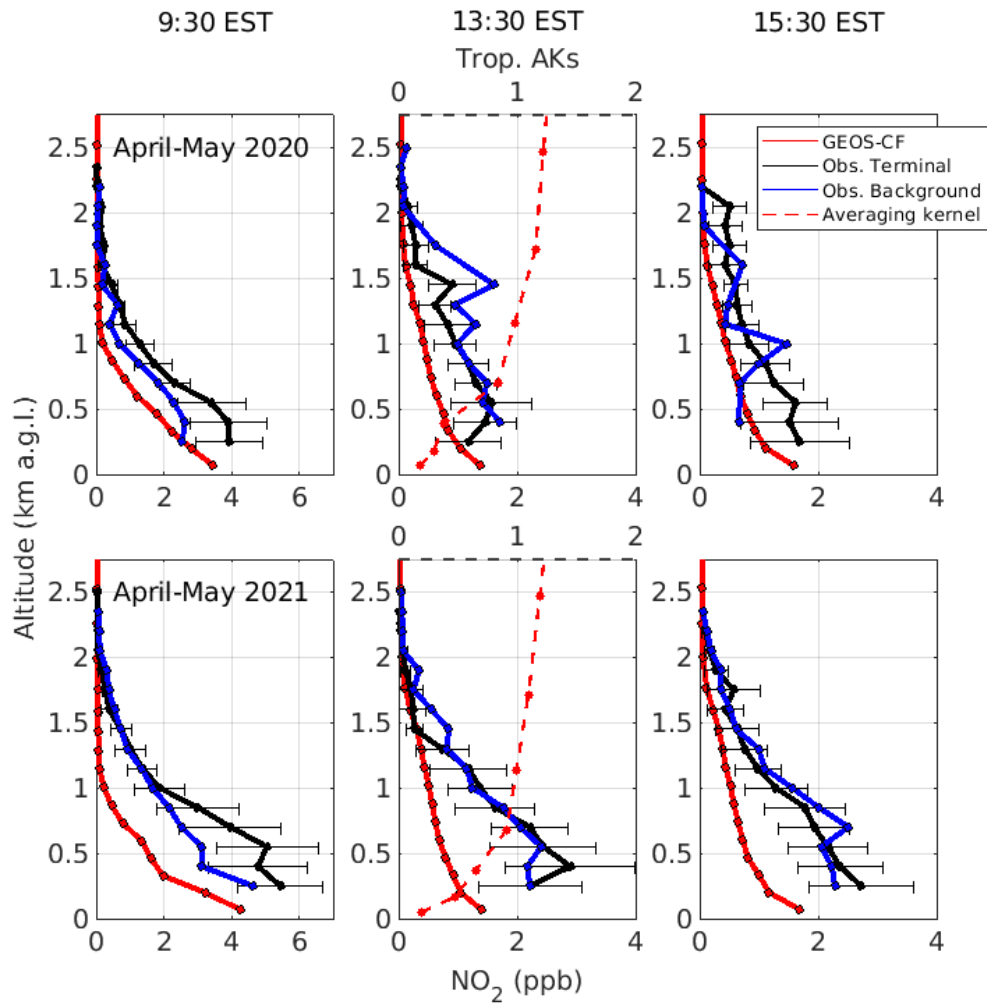


**Figure 4.8** Median modeled and observed  $\text{NO}_2$  profiles for periods of low and high air traffic (top and bottom, respectively). Only observations with tropospheric VCD enhancements (= terminal-background) 3 times greater than the measurement uncertainty are used for constructing the median profile shapes. Error bars are the median absolute deviation at each altitude. The median averaging kernel profile is shown for the TROPOMI overpass time and corresponds to the dashed axis.

In the morning (09:30 EST), airport vertical profiles consistently show elevated NO<sub>2</sub> at altitudes  $\leq 1$  km agl compared to background. The difference between background and airport-facing vertical profiles is larger in 2021 within the 0.4-1 km agl range, when airport activity is higher. These enhancements are likely a result of the larger near-airport emissions in the second period and comparably limited background vertical mixing in the morning. By mid-day (13:30 EST or later), the observed profile shapes for the background and runway directions are more similar in both years. Vertical profiles over ATL continue to show slight enhancements at altitudes  $\leq 0.5$  km agl, but are reduced relative to 09:30 EST. The horizontal homogeneity in median mid-day profiles may reflect a higher relative importance of NO<sub>2</sub> near the instrument and stronger atmospheric mixing. Absolute differences in over-airport and background NO<sub>2</sub> concentrations mid-day may be smaller than in the morning due to NO<sub>2</sub> photolysis, and therefore more difficult to detect on top of any near-instrument NO<sub>2</sub>. These smaller absolute differences likely result from diurnal PBL growth and pollution mixing from extensive on-road and ATL sources which could result in a large, polluted air mass that potentially spans several km in radius around the measurement site.

Figure 4.8 also shows the median GEOS-CF vertical profiles for the grid cell containing the Pandora instruments. The profiles are consistent from year-to-year, as COVID-related impacts are not included in the model. As the boundary layer grows throughout the day, the NO<sub>2</sub> mixing height increases, with sharp decreases in concentration around 1.25 km agl at 9:30 EST and near 2 km agl at 15:30 EST, and near-surface gradients becoming less pronounced. The observed shape profiles reflect an NO<sub>2</sub> mixing height that is typically higher than modeled which is consistent with comparisons made between GEOS-Chem and either MAX-DOAS or aircraft

vertical profiles from prior studies conducted in urban areas (Phaka et al., 2023; Yang et al., 2023). Additional analysis comparing Pandora and aircraft vertical profiles over U.S. airports is provided in section B.1. Results suggest Pandora profiles may not allocate enough of the NO<sub>2</sub> column within the first km agl, but more comparisons are needed.

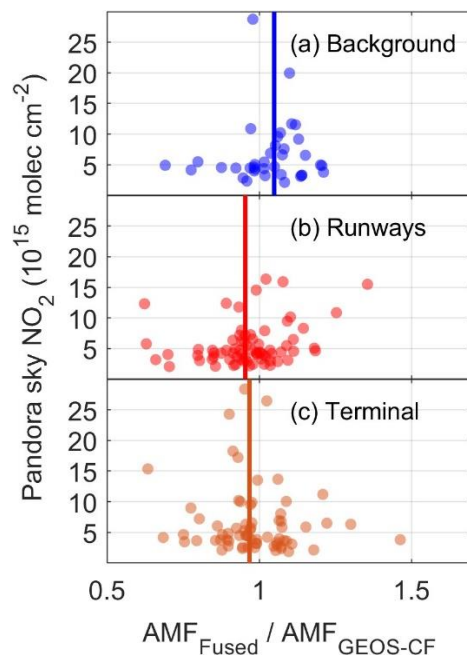
#### **4.3.4 TROPOMI NO<sub>2</sub> tropospheric VCDs: impact of modeled and fused AMF**

Figure 4.9 shows the ratio of AMF<sub>Fused</sub> to AMF<sub>GEOS-CF</sub> throughout the entire deployment period plotted against the corresponding sky VCD measurements. Median AMF<sub>Fused</sub> / AMF<sub>GEOS-CF</sub> ratios are 1.05 (background), 0.95 (runways), and 0.97 (terminal). Sky tropospheric VCDs are typically greater than modeled and the fused profile has more NO<sub>2</sub> nearer to the surface. Profile shape dictates the recalculated AMF values as they are normalized by the tropospheric VCD. Modeled profiles typically allocate approximately 87% (range of 80-95%) of the column within the first 0.75 km agl. By comparison, fused profiles in the runway and terminal directions allocate approximately 94% (range of 88-98%) within the same altitude, and would therefore be expected to produce smaller AMF than AMF<sub>GEOS-CF</sub>. However, while measuring over the North Sea, Riess et al. (2023) found a low sensitivity of recalculated AMFs to changes in near-surface concentrations, where a 50% increase in surface concentration resulted in only a 10% change in the AMF.

We perform similar sensitivity tests as in Riess et al. (2023). AMF<sub>Fused</sub> were recalculated two ways: by doubling either 1) the surface concentration of the profile or 2) the concentration of

the layer closest to 1 km agl. Doubling the surface concentration produced a linear regression between the recalculated and original  $AMF_{Fused}$  with a slope of 0.97. The same comparison after doubling the concentration at 1 km agl led to a slope of 1.04. These results indicate that increasing the surface layer concentration is offset by similar increases at 1 km agl. Median Pandora vertical profiles frequently have greater concentrations than the corresponding GEOS-CF estimates at altitudes up to 2.5 km agl (for instance, when measuring an aloft plume). Since AMF sensitivity to  $NO_2$  concentration increases with altitude, the fused profiles result in only a slight decrease in non-background AMFs relative to  $AMF_{GEOS-CF}$ .

The variability in the ratio is largest over the runway, with standard deviation ( $\sigma$ ) of 0.14. Standard deviations in the terminal and background direction are 0.12 and 0.11, respectively. Deviation from the median AMF ratio at large tropospheric  $NO_2$  VCDs may be indicative of plumes, with greater ratios indicating the plume is elevated above the surface. Additionally, aircraft departures are based on prevailing wind speed and direction. Behere et al. (2019) determined take-offs from ATL were primarily west-bound along the two inner landing strips to the north and south of the terminal. The runway-facing line of sight intersects with the southern landing strip and is anticipated to exhibit the most variability in  $NO_2$  VCDs. Deviations at lower tropospheric  $NO_2$  VCDs often reflect a lack of  $NO_2$  observed at the surface rather than a plume aloft and results in lower-than-median AMFs.



**Figure 4.9** Ratio of AMFs calculated from fused and GEOS-CF vertical profiles for each Pandora viewing direction. Vertical lines indicate median values. For clarity, data points with ratios  $>2$  are not shown ( $n=0, 1,$  and  $3$  in panels (a), (b), and (c), respectively).

Using  $AMF_{Fused}$  rather than  $AMF_{GEOS-CF}$  generally produces greater TROPOMI tropospheric VCDs. Pandora DS observations provide an independent, high-precision tropospheric  $NO_2$  VCD dataset for comparison. Results are shown in Figure 4.10. TROPOMI VCDs are super-observations in the runway direction, which is most similar to the Pandora DS footprint at the time of TROPOMI overpass (Figure 4.1). Correlations and NMDs are calculated as TROPOMI VCDs relative to Pandora VCDs. TROPOMI and Pandora DS tropospheric VCDs are well correlated with  $r = 0.70$  for VCDs calculated using  $AMF_{GEOS-CF}$  and  $r = 0.73$  for VCDs calculated using  $AMF_{Fused}$  over the entire deployment period. VCDs using  $AMF_{GEOS-CF}$  produced a  $NMD = -29\%$ , while VCDs using  $AMF_{Fused}$  produced a  $NMD = -22\%$ . These biases are

significantly lower than Phaka et al. (2023), who compared similarly recalculated TROPOMI VCDs (daily median MAX-DOAS vertical profiles in an urban area) to MAX-DOAS tropospheric VCDs. They report biases of -11.5% when comparing daily measurements for monthly averaged values. Correlations for monthly averaged data ( $r = 0.68$ ) were comparable to correlations determined in this work. NO<sub>2</sub> vertical profiles reported in their study indicate that our surface concentration assumption underestimates the actual concentration. Our results indicate that combining GEOS-CF or fused profiles with TROPOMI retrievals improves accuracy but still produces underestimated columns when monitoring airport NO<sub>2</sub>.

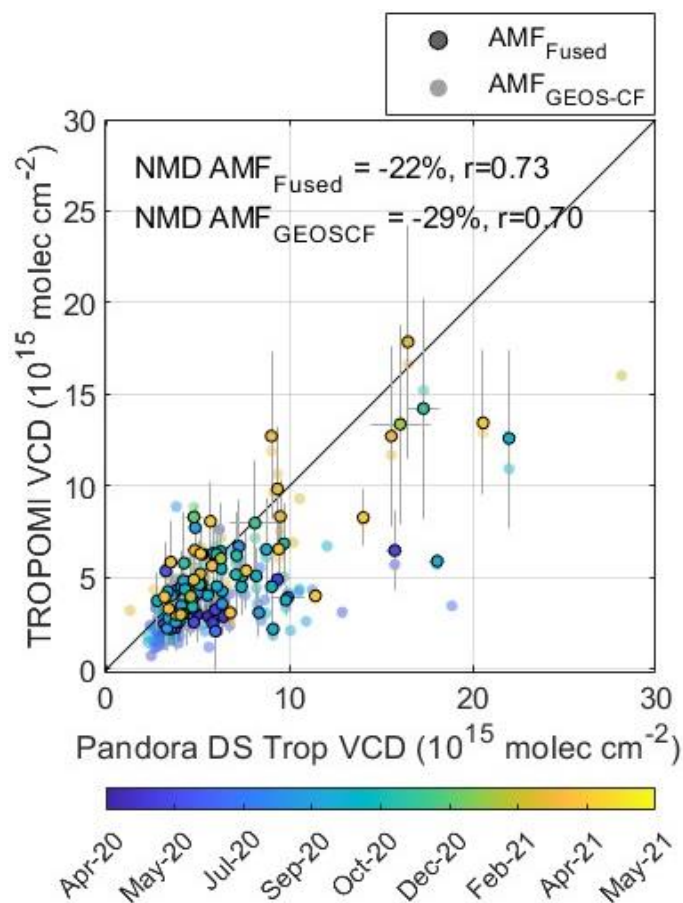


**Figure 4.10** TROPOMI and Pandora DS  $NO_2$  tropospheric VCDs. TROPOMI products are updated using either  $AMF_{GEOS-CF}$  or  $AMF_{Fused}$ . Error bars represent measurement uncertainty.

Looking forward to TEMPO, we examine diurnal variation in tropospheric  $NO_2$  VCDs over the runway and the airport and compare to the variation seen by TROPOMI, while noting that number of observations in the late afternoon is small. Observations for periods of high and low airport activity are shown in Figure 4.11. As also suggested by the vertical profiles in Figure 4.8, mid-afternoon Pandora sky tropospheric VCDs show little difference between viewing directions in both 2020 and 2021. In 2020, observations remain flat throughout the day, whereas 2021 shows over-airport enhancements in the morning. From Figure 4.5, DS observations reveal

that these morning enhancements begin in July 2020 when vehicle traffic stabilized and daily departures saw a significant increase which continued throughout deployment. This suggests that satellite-based observations in the early morning will more clearly reflect the impact of aviation on near-airport emissions than what is possible with TROPOMI. These early morning profiles, however, may be more sensitive to errors in modeled mixing heights. We find that TROPOMI VCDs calculated using  $AMF_{GEOS-CF}$  are within the range of Pandora observations and show similarly small hourly variation in mid-afternoon. TROPOMI VCDs calculated using  $AMF_{Fused}$  show larger variation, which is a reflection both of greater observed  $NO_2$  variability and a more limited number of Pandora sky observations in this dataset.

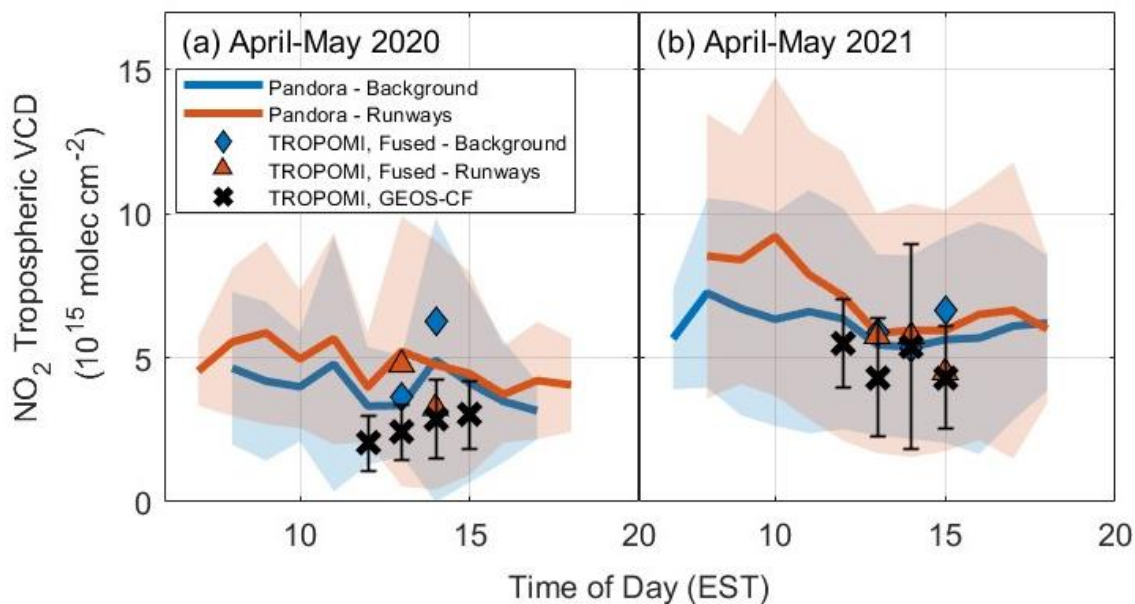


**Figure 4.11** Hourly averaged Pandora sky VCDs overlooking the background or ATL runways during periods of (a) low and (b) high aviation. Shaded regions and error bars are the standard deviation of hourly averaged data. TROPOMI VCDs are calculated using  $AMF_{GEOS-CF}$  and  $AMF_{Fused}$ . TROPOMI VCDs using  $AMF_{Fused}$  super-observations along the line of sight.

### 4.3.5 Implications

We report the first Pandora sky vertical profiles measured in a complex, heterogeneous environment. We find that using fused vertical profiles to inform TROPOMI AMFs results in a product that exhibits less bias than using only modeled profiles relative to independent Pandora DS tropospheric NO<sub>2</sub> observations. However, both products still exhibit significantly low biases indicating that alternative AMFs calculated in this work are too large. This is attributed to the resolution of GEOS-CF, Pandora measurements not directly measuring near-surface, and the assumption for our surface concentration being too low. The improvement in bias using fused profiles nonetheless gives confidence in the ability to use NO<sub>2</sub> vertical profile estimates and observations from the rapidly expanding Pandora global network not just for satellite evaluation, but for development of improved products. We note that results here using our unique viewing configuration and location may differ from studies in other environments and with the standard Pandora viewing schedules. There is still a need for independent evaluation of Pandora sky observations using in-situ observations.

We find that difference between observed and modeled vertical profiles, and between vertical profiles in different viewing directions, is largest in morning hours. This underscores the opportunity of geostationary observations from geostationary instrumentation like TEMPO to diagnose emissions at times when “hot-spots” appear brightest. Our results suggest that a correct representation of vertical mixing heights is especially important when using models to calculate a priori vertical profiles. In contrast, variability in observations suggest that even very different emissions scenarios such as those driven by the COVID pandemic have little impact on AMFs

calculated from observations. This gives confidence in top-down emissions derivation methods that assume a constant emissions/AMF relationship. However, Jin et al. (2021) found that using GEOS-CF NO<sub>2</sub> vertical profiles for calculating alternative TROPOMI AMFs led to significant enhancements in satellite-derived NO<sub>2</sub> emission factors. Coupled with the agreement between the modeled and fused versions of TROPOMI VCDs and observations in this work, this indicates that prior emissions estimates like that of Fioletov et al. (2021), who used the standard TROPOMI NO<sub>2</sub> VCD product, may underpredict absolute emissions in urban areas or around point sources.

Further quantification of free tropospheric NO<sub>2</sub> will be required. Dang et al. (2023) predicted a 14% increase in AMFs over the next decade, owed to increasing free tropospheric NO<sub>2</sub> resulting from aircraft emissions. However, results from recent works show the difficulty in accurately modeling free tropospheric NO<sub>2</sub> ((Dang et al., 2023; Shah et al., 2023). Pandora spectrometers have been used previously for measuring upper tropospheric NO<sub>2</sub> (Marais et al., 2021) and could be beneficial to future modeling efforts. We note that the standard GEOS-CF profiles used in this work likely underestimate free tropospheric NO<sub>2</sub> as this product doesn't include updated mechanisms used in prior works (Dang et al., 2023; Yang et al., 2023). As Pandora vertical profiles are representative of the boundary layer, TROPOMI tropospheric VCDs in this work are anticipated to underestimate NO<sub>2</sub> in the upper layers regardless of AMF choice.

A prior work by Lawal et al. (2021) focused on NO<sub>2</sub> emissions at ATL using a high resolution (4 x 4 km<sup>2</sup>) CTM coupled with a landing and take-off emissions inventory to develop new AMFs. Updated TROPOMI VCDs saw a 60% increase over ATL compared to the standard

VCD product, which is significantly greater than the corresponding increases seen in this work when using  $AMF_{GEOS-CF}$  (25.4%) or  $AMF_{Fused}$  (17%). They noted significant improvement in bias between satellite and modeled VCDs, which was attributed to less steep, modeled  $NO_2$  vertical profiles near the airport due to the dilution of emissions. GEOS-CF vertical profiles in this work exhibit similar behavior, having a much steeper vertical gradient than observed, leading to underestimations of near-airport  $NO_2$  VCDs.

Even after correcting for the vertical profiles of  $NO_2$  observed over the airport, TROPOMI retrievals suggest that ATL is a dominant source of  $NO_x$  emissions in the Atlanta region. As is true for several airports, there are no regulatory monitors near ATL. Aviation-related emissions have a disproportionate impact on historically disadvantaged communities. Our results suggest that satellite observations coupled with higher resolution models provide a reliable starting point for diagnosing longer-term trends in  $NO_2$  and the underlying emissions from the growing airport source sector.

## CHAPTER 5 SUMMARY AND FUTURE WORK

### 5.1 Summary of current work

Anthropogenic emissions have and continue to degrade air quality, impact human health, and alter atmospheric chemical regimes. They lead to enhanced radiative forcing through the emission of greenhouse gases and the formation of ozone ( $O_3$ ) through chemical interactions of volatile organic compounds (VOCs) and oxides of nitrogen ( $NO_x = NO + NO_2$ ). To predict and mitigate pollution events, understanding atmospheric composition and the oxidation pathways of VOCs is imperative. Models provide a spatiotemporally complete estimation of VOC chemical pathways. Recent satellite developments now allow for hourly measurements of  $NO_x$  and formaldehyde (HCHO) that cover vast swaths of area. However, both exhibit biases and rely on observations to test their underlying hypotheses.

Observations from single instruments or ground-networks are frequently used to inform and gauge model and satellite retrieval accuracy. Modern day techniques offer fast measurements with high resolution, precision, and accuracy, that are chemically detailed and easily deployable. In this thesis, ground-observations from multiple instrument platforms were employed for the purpose of expanding available wildfire emissions modeling datasets (Chapter 2), evaluating extant ground-network HCHO measurements and demonstrating the advantages of modern day in situ monitors (Chapter 3), and developing methods of fusing observations and models (Chapter 4).

As part of the Characterizing Organic Aerosols and Loading Over Australia 2020 (COALA-2020) campaign, we deployed a proton transfer reaction time-of-flight mass spectrometer (PTR-ToF-MS) to New South Wales (NSW), AU during the Black Summer wildfire season. Chemical abundance and speciation of VOCs emitted from wildfires exhibit high variability. Biomass burning VOCs (BBVOCs) are oxidized during plume transport, which affects local chemistry. The temperate forests of NSW are understudied as they have few prior wildfire measurements. We used PTR-ToF-MS observations of an opportunistically sampled wildfire plume that travelled overnight to the COALA field site to develop a nighttime-oxidation chemical age marker, derive EFs for 15 VOCs, and quantify OH reactivity. Absolute values of chemical aging could not be determined, but ratios of furan and its NO<sub>3</sub>-initiated oxidation products revealed the chemically youngest smoke was sampled from 04:00-06:00 LT, coinciding with the shortest HYSPLIT back-trajectories that travelled entirely in the night. The choice of meteorological dataset has the possibility to influence the interpretation of a plume's origin, its transport time and pathway, and its subsequent interaction with other plumes. Future works studying the chemical evolution of plumes could utilize different meteorological datasets for the same model run for a more wholistic picture of plume transport. OH reactivity revealed that biogenic VOCs contributed most to reactivity (2-6.35 s<sup>-1</sup>), then furans (1.24-3.93 s<sup>-1</sup>), aromatics (0.66-2.14 s<sup>-1</sup>), and alkenes (0.86-1.83 s<sup>-1</sup>). EFs were compared to those from two AU-based, two U.S.-based, and 1 globally averaged study. The greatest disagreement was seen with another AU-based work that sampled controlled burns and is attributed to differences in sampling approach and fuel type. Agreement was best with EFs from the U.S.-based studies which supports the use of EFs from geographically separate but analogous biomes for modeling of wildfire emissions.

Three fast, in-situ HCHO monitors (Aeris Ultra, Aeris Pico, and Picarro G2307) were deployed over a period of one year across two different field sites in the Atlanta, GA metropolitan area. Optimal strategies were developed to make deployment feasible and mitigate the influence of H<sub>2</sub>O on measurements. Maximum precisions for the HCHO monitors were determined to be 0.01 ppb (Picarro G2307, 20 min average), 0.20 ppb (Aeris Ultra, 30 s average), and 0.40 ppb (Aeris Pico, 30 s average). All monitors exhibited stable sensitivities during deployment. Two intercomparisons using ambient measurements were performed one year apart and showed strong correlations ( $r \geq 0.9$ ) and normalized mean differences (NMDs)  $\leq 13\%$ . Observations from the Picarro G2307 were compared to those from the U.S. Environmental Protection Agency's TO-11A sampling technique. TO-11A observations correlated well with the Picarro G2307 ( $r = 0.75$ ) but produced a NMD of -52%. Low biases between TO-11A and other fast measurement monitors have been previously reported, but this discrepancy is by far the largest. We compared our HCHO measurements with historical observations from 1999 in Atlanta's urban core and at the South Dekalb (SDK) photochemical and assessment monitoring station located 15 km southeast (rural/urban atmospheric regime). Midday urban HCHO showed a decrease of 22.3% in Atlanta and 53% at SDK. Importantly, the relative decrease at SDK was determined using TO-11A measurements. Comparing 1999 TO-11A values to those from the Picarro G2307 resulted in only a 2% decrease. This chapter shows the precision, accuracy, and feasibility of deployment achievable by modern day, commercially available HCHO monitors and the advantages they offer over existing ground-network sampling strategies.

Finally, we used NO<sub>2</sub> vertical profiles measured by a Pandora spectrometer to evaluate TROPOMI retrievals over the Hartsfield-Jackson International airport (ATL) during the COVID-19 lockdown. Airports are officially unmonitored and increasingly significant sources of NO<sub>2</sub>. Satellite observations offer a long-term strategy for tracking NO<sub>2</sub> vertical column densities (VCDs). Previous studies have shown satellites exhibit biases when observing over polluted regions due to coarse resolution a priori vertical profiles used for calculating air mass factors (AMFs). We recalculated AMFs from TROPOMI (TROPospheric Ozone Monitoring Instrument) using profiles from Global Earth Observing System Compositional Forecasts (GEOS-CF, AMF<sub>GEOS-CF</sub>) and from a model/measurement fusion approach (AMF<sub>Fused</sub>). Observed vertical profile concentrations were typically greater than modeled from 0-3 km above ground level and showed greater mixing heights. Near-surface concentrations are greatest in the morning, indicating the potential for recently launched geostationary satellites to diagnose emissions during this “hot-spot” time of day. We found that median AMF<sub>Fused</sub> / AMF<sub>GEOS-CF</sub> ratios ranged from 0.97-1.05. TROPOMI VCDs when compared to direct sun tropospheric VCDs exhibited NMDs of -22% (AMF<sub>Fused</sub>) and -29% (AMF<sub>GEOS-CF</sub>) for the deployment period. These results show that geostationary satellites will provide greater chemical insight into the trends of aviation-related NO<sub>2</sub> but highlight the need for continued intensive ground-monitoring and further validation of the Pandora vertical profile product.

## **5.2 Future directions**

Beyond the work detailed in this thesis, there are many future directions to consider. As wildfire seasonal lengths are projected to globally increase, Australia will increasingly experience the ramifications of degrading air quality and exposure to carcinogenic biomass burning emissions. Simmons et al. (2022) employed measurements from our PTR-ToF-MS and quantified the toxicological loading of gas phase variables for a small suite of compounds. Further health studies could be conducted linking impacts of specific fires (like the infamously intense Canberra fires of the Black Summer) to air pollution-related health in cities. Additionally, no new EFs have been made available since COALA-2020, keeping the list of extant Australian temperate biome EFs small. While work in this thesis suggests the use of biome-analogous EFs may be suitable, variability across EFs within the same biome is large and indicates the need for more chemically comprehensive measurements. EFs from global averages, U.S.-based and AU-based ground burns (like those studied in Guérette et al. 2018) in temperate zones could be compared to further assess the impact of plume sampling approach on inter-study EF agreement. Nighttime plume-tracking measurements from aircraft campaigns (e.g. WE-CAN, FIREX 2019) may offer the ability to better constrain the temporal evolution of NO<sub>3</sub>-oxidation of furan and subsequently the nighttime chemical age marker presented in this work.

Within the U.S., results in this thesis suggest that the TO-11A method may produce HCHO observations that are biased low relative to actual concentrations. These biases carry into evaluations of satellite retrievals or into HCHO emissions estimates calculated using TO-11A

data. Future works could explore whether this issue systematically occurs at PAMS sites and identify the mechanism underlying it.

An attempt at deriving free tropospheric NO<sub>2</sub>, which is expected to increase over the next decade as a result of aviation-related emissions and, consequently, increase satellite AMFs, could be done using direct sun and sky measurements from the Pandora global network. Specific to our ATL measurements, observed vertical profiles could be combined with a statistical plume-fitting approach like that of Fioletov et al. (2021) to deconvolute and quantify airport and urban background NO<sub>2</sub> emissions as current satellite-based estimates likely underestimate actual NO<sub>2</sub>. Such analysis could determine to what extent tropospheric NO<sub>2</sub> accounts for differences between airport and background emissions. Missing NO<sub>2</sub> mass in extant emissions estimates affects our understanding of the local NO<sub>x</sub>-regime and may convolute our understanding of VOC oxidation pathways.

Finally, retrievals from the recently launched Tropospheric Emissions: Monitoring of Pollution (TEMPO) instrument will require extensive evaluation as a function of time of day. The Pandora network offers both the means for hourly evaluation as well as measurements that can be used to improve satellite retrieval accuracy. Furthermore, this thesis only presents measurements from the Pandora NO<sub>2</sub> product. Pandoras offer the same VCD products for HCHO for which analogous evaluation efforts could be conducted. The utility of Pandora measurements makes them indispensable for extensive monitoring of highly polluted areas. Future efforts to better constrain airport vertical profiles could be done through comparison with missed landing approaches from aircraft campaigns like WE-CAN. The ability to evaluate and improve the

accuracy of TEMPO retrievals, especially over increasingly important hot-spots, will provide a remarkable, regional-scale image of air pollution formation and transport.

**APPENDIX A**  
**SUPPORTING INFORMATION FOR CHAPTER 2**

**A.1 Supplemental information for PTR-ToF-MS and supporting observations**

**Table A.1** Standards used to calibrate PTR-TOF-MS as well as determine instrument transmission and limits of detection. The uncertainty of each compound is 15%.

		<b>Calibration Standards</b>			
<b>Compound</b>	<b>Formula</b>	<b>m/z</b>	<b>Uncertainty (%)</b>	<b>In Standard</b>	<b>Limit of Detection (3σ, ppt)</b>
Methanol	CH <sub>4</sub> OH+	33.00	15	Yes	5
Acetonitrile	C <sub>2</sub> H <sub>3</sub> NH+	42.03	15	Yes	5
Acetaldehyde	C <sub>2</sub> H <sub>4</sub> OH+	45.03	15	Yes	5
Acrolein	C <sub>3</sub> H <sub>4</sub> OH+	57.03	15	Yes	15
Acetone	C <sub>3</sub> H <sub>6</sub> OH+	59.05	15	Yes	20
Isoprene	C <sub>5</sub> H <sub>8</sub> H+	69.07	15	Yes	165
Methyl Vinyl Ketone	C <sub>4</sub> H <sub>6</sub> OH+	71.05	15	Yes	5
Methacrolein	C <sub>4</sub> H <sub>6</sub> OH+	71.05	15	Yes	5
Methyl Ethyl Ketone	C <sub>4</sub> H <sub>8</sub> OH+	73.07	15	Yes	5
Benzene	C <sub>6</sub> H <sub>6</sub> H+	79.05	15	Yes	10

Toluene	$C_7H_8H^+$	93.07	15	Yes	15
C <sub>8</sub> -aromatics	$C_8H_{10}H^+$	107.09	15	Yes	5
Chlorobenzene	$C_5H_6ClH^+$	113.02	15	Yes	5
C <sub>3</sub> -benzene	$C_9H_{12}H^+$	121.10	15	Yes	20
P-cymene	$C_{10}H_{14}H^+$	135.12	15	Yes	10
$\alpha$ -pinene	$C_{10}H_{16}H^+$	137.13	15	Yes	20
Cineole	$C_{10}H_{18}H^+$	155.14	15	Yes	20

**Table A.2** All species in this work either in calibration standards or for which an EF was derived and their respective uncertainties.

		<b>All Presented Compounds</b>		
<b>Compound</b>	<b>Formula</b>	<b>m/z</b>	<b>Uncertainty (%)</b>	<b>In Standard</b>
Methanol	CH <sub>4</sub> OH <sup>+</sup>	33.00	15	Yes
Acetonitrile	C <sub>2</sub> H <sub>3</sub> NH <sup>+</sup>	42.03	15	Yes
Acetaldehyde	C <sub>2</sub> H <sub>4</sub> OH <sup>+</sup>	45.03	15	Yes
Acrolein	C <sub>3</sub> H <sub>4</sub> OH <sup>+</sup>	57.03	15	Yes
Acetone	C <sub>3</sub> H <sub>6</sub> OH <sup>+</sup>	59.05	15	Yes
Isoprene	C <sub>5</sub> H <sub>8</sub> H <sup>+</sup>	69.07	15	Yes
Methyl Vinyl Ketone	C <sub>4</sub> H <sub>6</sub> OH <sup>+</sup>	71.05	15	Yes
Methacrolein	C <sub>4</sub> H <sub>6</sub> OH <sup>+</sup>	71.05	15	Yes
Methyl Ethyl Ketone	C <sub>4</sub> H <sub>8</sub> OH <sup>+</sup>	73.07	15	Yes
Benzene	C <sub>6</sub> H <sub>6</sub> H <sup>+</sup>	79.05	15	Yes
m/z 85	C <sub>4</sub> H <sub>4</sub> O <sub>2</sub> H <sup>+</sup>	85.03	100	No
Methyl propanoate	C <sub>4</sub> H <sub>8</sub> O <sub>2</sub> H <sup>+</sup>	89.06	100	No
Toluene	C <sub>7</sub> H <sub>8</sub> H <sup>+</sup>	93.07	15	Yes

Maleic Anhydride	C <sub>4</sub> H <sub>2</sub> O <sub>3</sub> H <sup>+</sup>	99.00	100	No
Methyl Methacrylate	C <sub>5</sub> H <sub>8</sub> O <sub>2</sub> H <sup>+</sup>	101.06	100	No
Benzaldehyde	C <sub>7</sub> H <sub>6</sub> OH <sup>+</sup>	107.05	100	No
C <sub>8</sub> -aromatics	C <sub>8</sub> H <sub>10</sub> H <sup>+</sup>	107.09	15	Yes
Chlorobenzene	C <sub>5</sub> H <sub>6</sub> ClH <sup>+</sup>	113.02	15	Yes
C <sub>3</sub> -benzene	C <sub>9</sub> H <sub>12</sub> H <sup>+</sup>	121.10	15	Yes
P-cymene	C <sub>10</sub> H <sub>14</sub> H <sup>+</sup>	135.12	15	Yes
α-pinene	C <sub>10</sub> H <sub>16</sub> H <sup>+</sup>	137.13	15	Yes
Cineole	C <sub>10</sub> H <sub>18</sub> H <sup>+</sup>	155.14	15	Yes

## **A.2 Supplemental analysis of plume origin and transport time**

Figure A.1 shows the altitude above ground level (agl) for each of the 12 back-trajectories plotted in Figure 2.1. For the periods closer to sunrise (06:00 LT) on 4 Feb 2020, the model predicts higher altitudes that reach 563 m agl at maximum. The increasing altitudes likely resulted from air masses spending more time travelling over active fires. The decline in altitude results from these same masses travelling over the ocean which has less turbulent, cooler atmospheric conditions and generally a lower boundary layer height.

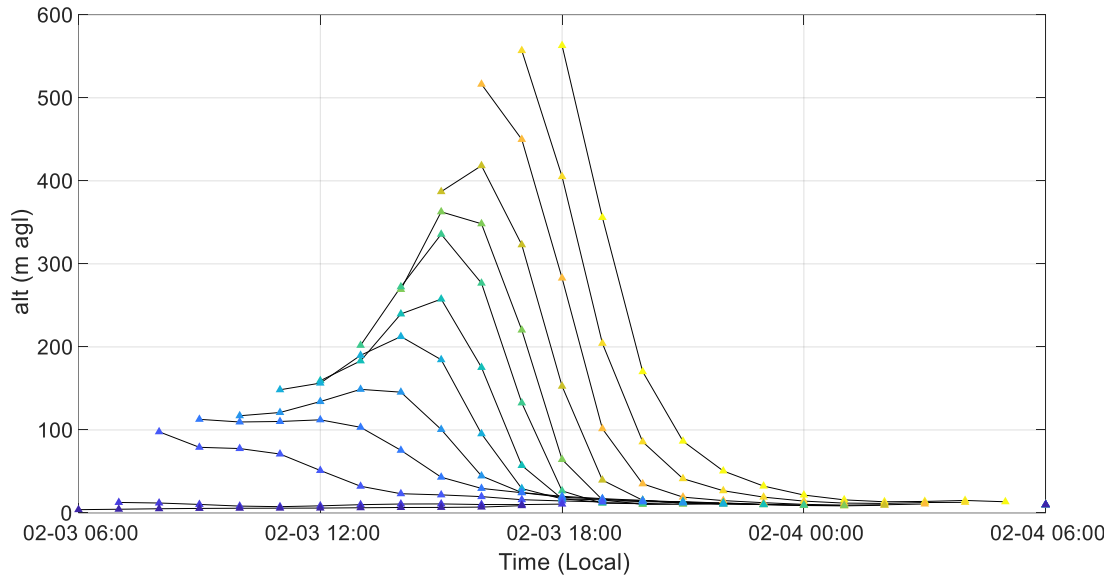


**Figure A.1** Altitudes corresponding by color to trajectories plotted in Figure 2.1.

There are two major clusters of fires emitting during the period over which we sampled smoke; the fires just to the south of Canberra (Figure A.2), and the two large clusters at the southeast (SE) corner (Figures A.3 and A.4) which mix into one plume. We examine both how these plumes interacted and the meteorological conditions surrounding the SE clusters. HYSPLIT forward trajectories are shown in Figures A.2 and A.3 using the same meteorological input and at the same altitude layers as in Figure 2.1.

In Figure A.2, the HYSPLIT forward trajectory shows that the plumes from the Canberra fires intersected with the SE fire clusters up until local midnight on 4 Feb 2020. When both sets of trajectories intersected, plumes from the Canberra wildfires had lofted to altitudes of 1600-2000 m agl, while plumes from the SE cluster descended to altitudes < 200 m agl (Figure A.1). While the Canberra wildfire emissions likely mixed throughout the column, these trajectories indicate that little mixing would have occurred between these two plumes and that the plume

from the SE is almost entirely what was sampled, with only smaller fires along the eastern coast potentially contributing.

After local midnight on 4 Feb, trajectories from the Canberra cluster shifted and transported plumes to the northwest, and therefore are assumed to negligibly mix with plumes from the SE clusters.

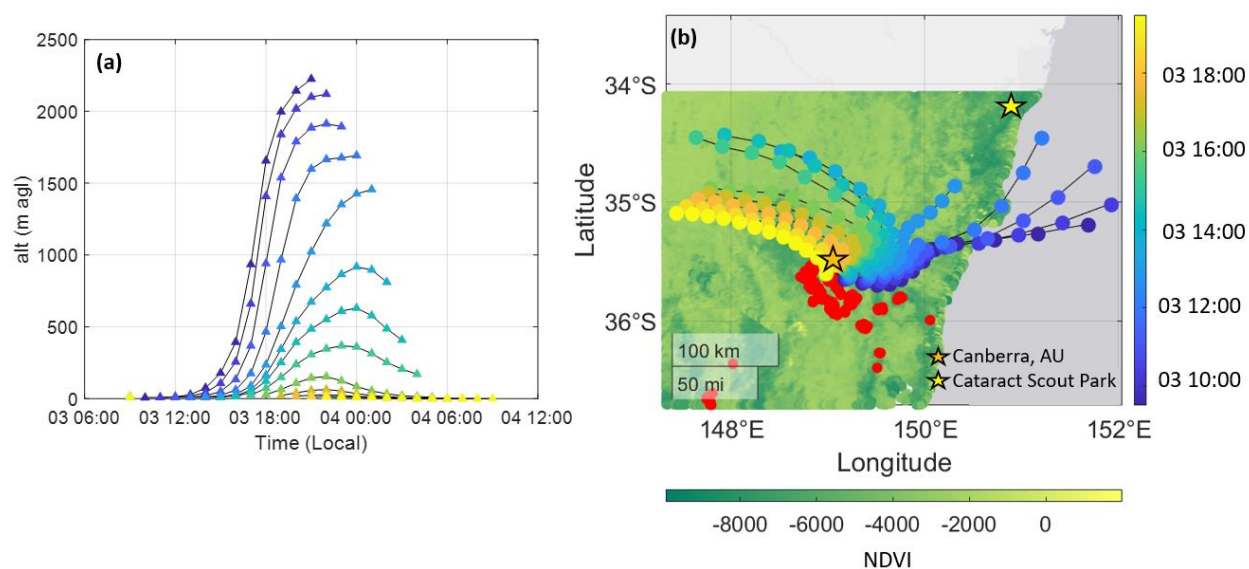


**Figure A.2** HYSPLIT forward trajectory starting at the centroid of the fire cluster to the south of Canberra, AU. This simulation was set to run at 10:30 on 3 Feb 2020 - 8 h in advance of when the PTR-ToF-MS began sampling smoke. Each tail moves forward in time 12 h, with a new tail plotted every hour. Panel (a) shows the altitude to which each trajectory was lofted, and panel (b) shows the spatial distribution of the plots as well as Canberra and Cataract Scout Park's location. Normalized difference vegetation index (NDVI) is also plotted to show greenery distribution, with darker green signifying denser foliage.

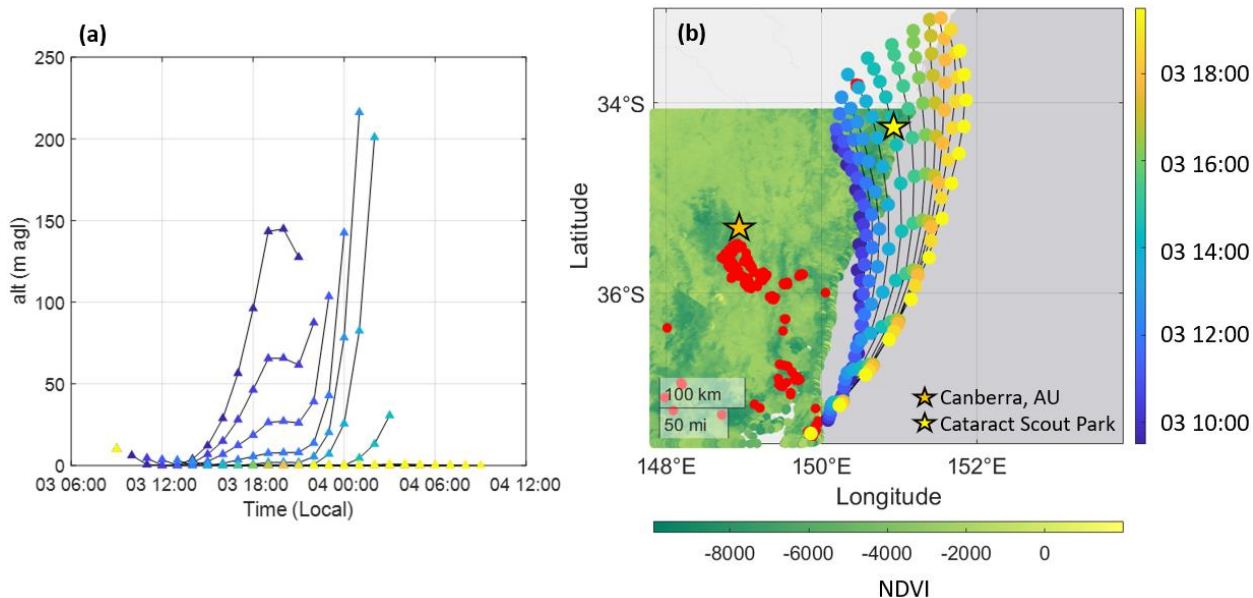


**Figure A.3** HYSPLIT forward trajectory starting at the southern fire cluster in the southeast corner of the country. This simulation was set to run at 10:30 on 3 Feb 2020 - 8 h in advance of when the PTR-ToF-MS began sampling smoke. Each tail moves forward in time 12 h, with a new tail plotted every hour. Panel (a) shows the altitude to which each trajectory was lofted, and panel (b) shows the spatial distribution of the plots as well as Canberra and Cataract Scout Park's location. Normalized difference vegetation index (NDVI) is also plotted to show greenery distribution, with darker green signifying denser foliage.

Combustion conditions can change the chemical profile of wildfire emissions and are governed by local meteorology. Wind speed as well as fuel moisture content change a burn's combustion efficiency. Figure A.4 displays a closer view of the two active fires in the southeast (SE), whose centroids are spaced approximately 70 km apart and potentially subject to different meteorological conditions. We compare the wind speeds of the areas containing the SE fire clusters (green and blue triangles in Figure A.4) and use total precipitation as a proxy for fuel moisture content.

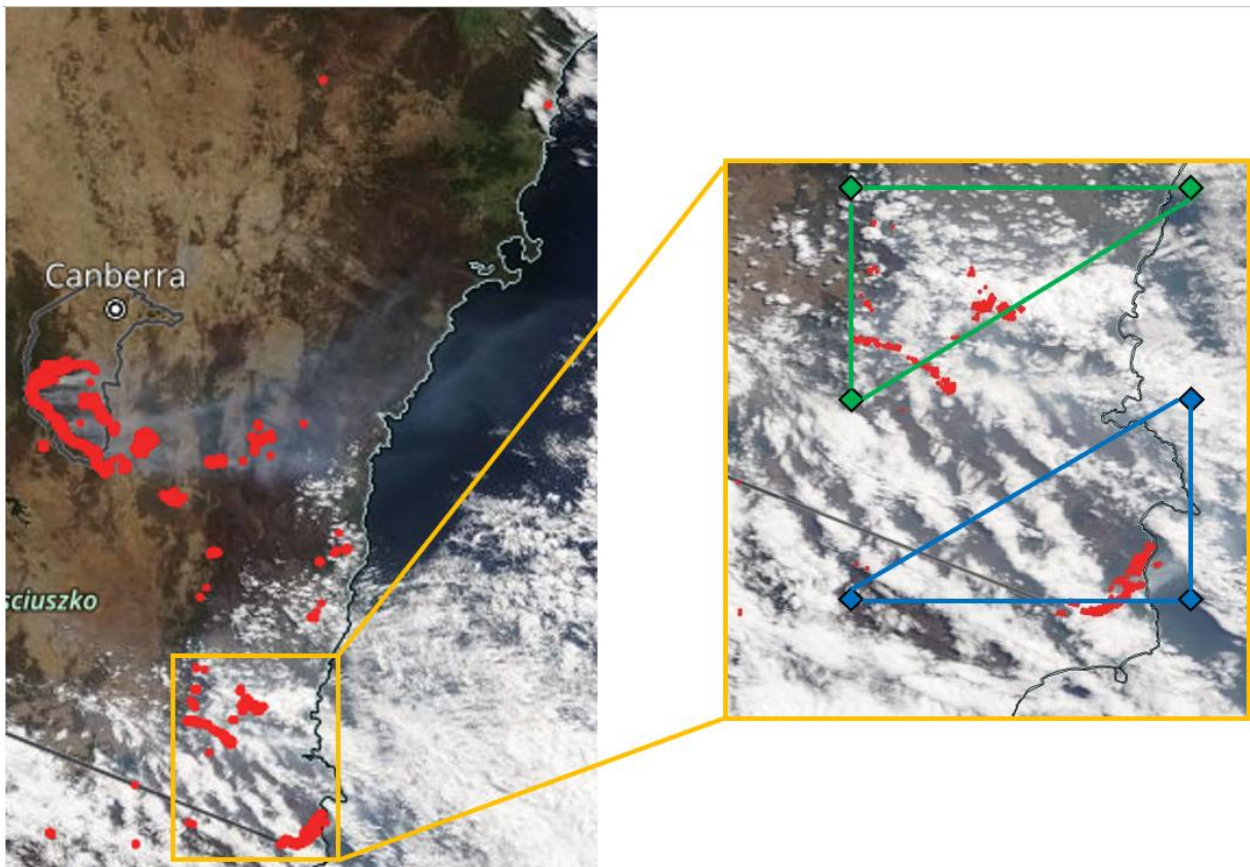


**Figure A.4** NASA Worldview imagery with fire counts plotted from the VNP14IMGTDL\_NRT data from Suomi VIIRS satellite imaging. The left side of the graph shows the general location of the two southeast fire clusters which are termed the “north” (green triangle) and “south” (blue

triangle) clusters. These active burning sites are approximately 70 km apart. The green and blue triangles on the right correspond to the indices over which average surface wind speed was calculated using data from MERRA-2.

Hourly wind speed is calculated using data from MERRA-2 measured at 10 m agl (Gelaro et al., 2017). This data has a spatial resolution of  $0.5^\circ \times 0.625^\circ$  and the corresponding coordinate points used for spatial averaging are shown on the right side of Figure A.4, with the green triangle overlaid on the northern fire cluster and the blue triangle on the southern. Results are shown in Figure A.5 and indicate that both fires saw similar wind speeds before, during, and after the period the PTR-ToF-MS sampled smoke. We assume that wind speed didn't cause significantly different combustion conditions between the two fire clusters.

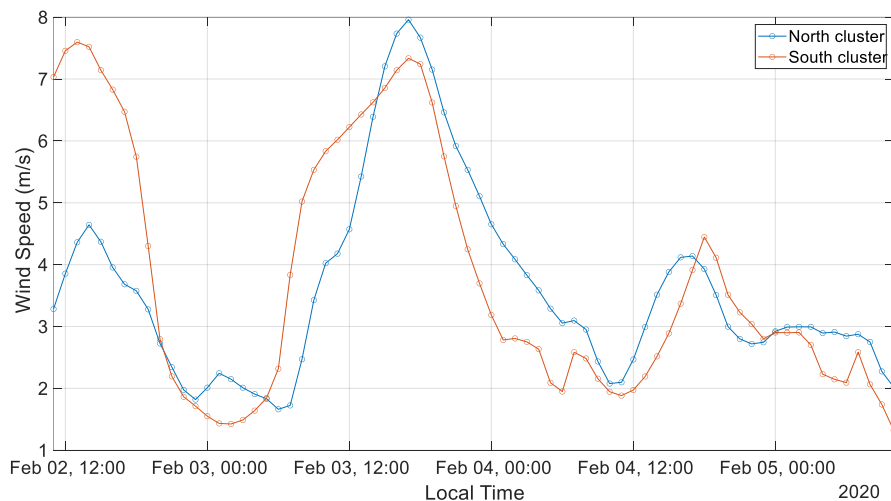


**Figure A.5** Hourly, spatially averaged wind speed for the northern and southern fire clusters corresponding to the green (northern) and blue (southern) triangles in Figure A.4. These values are calculated using hourly measurements of the U10M and V10M wind direction data from the MERRA-2 `tavg1_2d_slv_Nx` dataset at  $0.5^\circ \times 0.625^\circ$  resolution.

Last, Figure A.6 shows modeled monthly averages of total precipitation for the month of January 2020, preceding when the southeast fires started. This data is outputted from the Australian Bureau of Meteorology’s Gridded Climate Data at a  $0.05^\circ \times 0.05^\circ$  resolution (Jones et al., 2009) with the image generated from the Australian Bureau of Meteorology’s website. Both of the SE fire clusters are active in similarly forested regions that experienced approximately 25 mm precipitation, indicating fuel moisture content shouldn’t be significantly different. We assume that both clusters burned under similar combustion conditions and that EFs derived the their combined plume are representative of a biome-averaged EF.

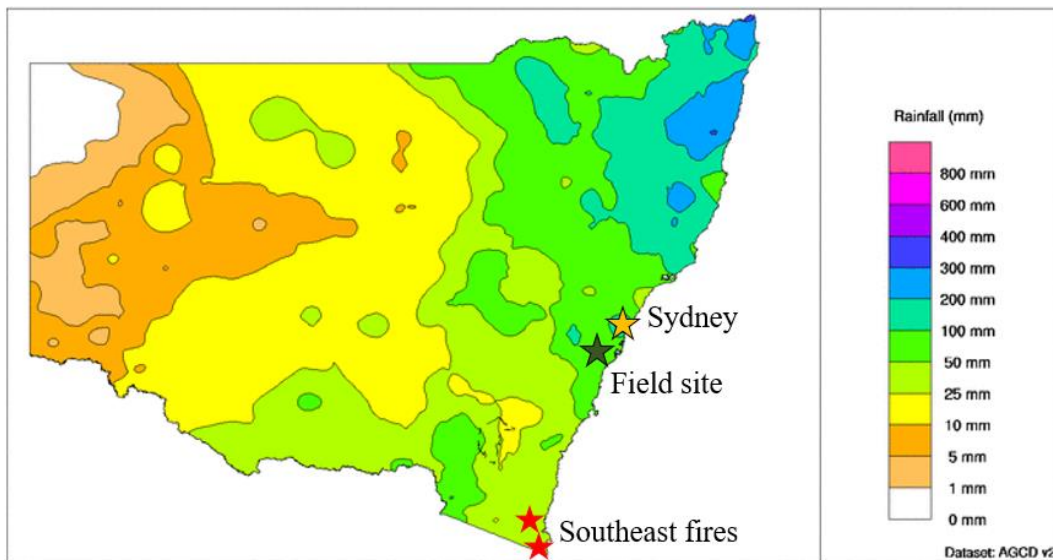


**Figure A.6** Daily total precipitation averaged over the month of January 2020 from the Australian Bureau of Meteorology’s Gridded Climate Data at a resolution of  $0.05^\circ \times 0.05^\circ$ , occurring prior to the southeast fires. Image generated from the Bureau of Meteorology (<http://www.bom.gov.au/climate/maps/rainfall/>). Both clusters are in a region that has experienced similar total rainfall between 25-50 mm.

### A.3 Supplemental information for emission ratios

Figure A.7 shows a comparison between ERs derived from two subsets of data over the smoke event – one from the freshest portion of the plume and the other using an average of the 4 subsets making up the entirety of the event. Table A.3 provides the ERs averaged over all four periods with the corresponding standard deviation. For species with ERs during different periods, period D ERs are within  $1\sigma$ .

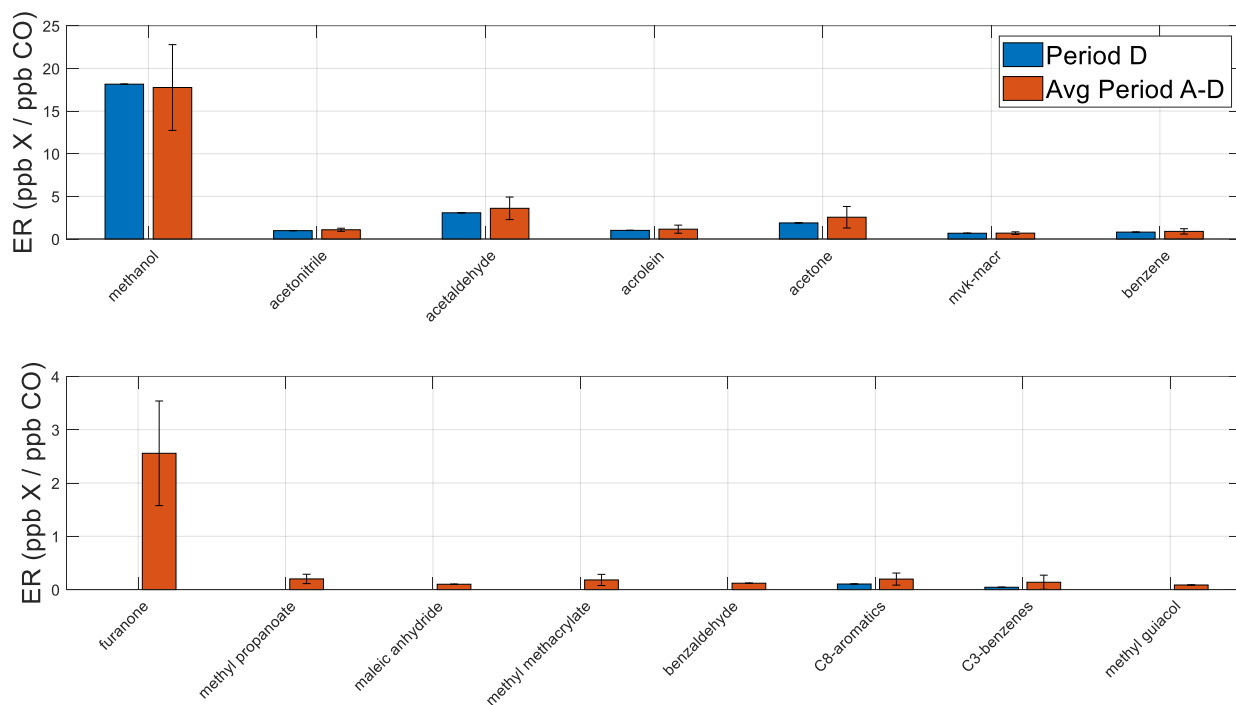


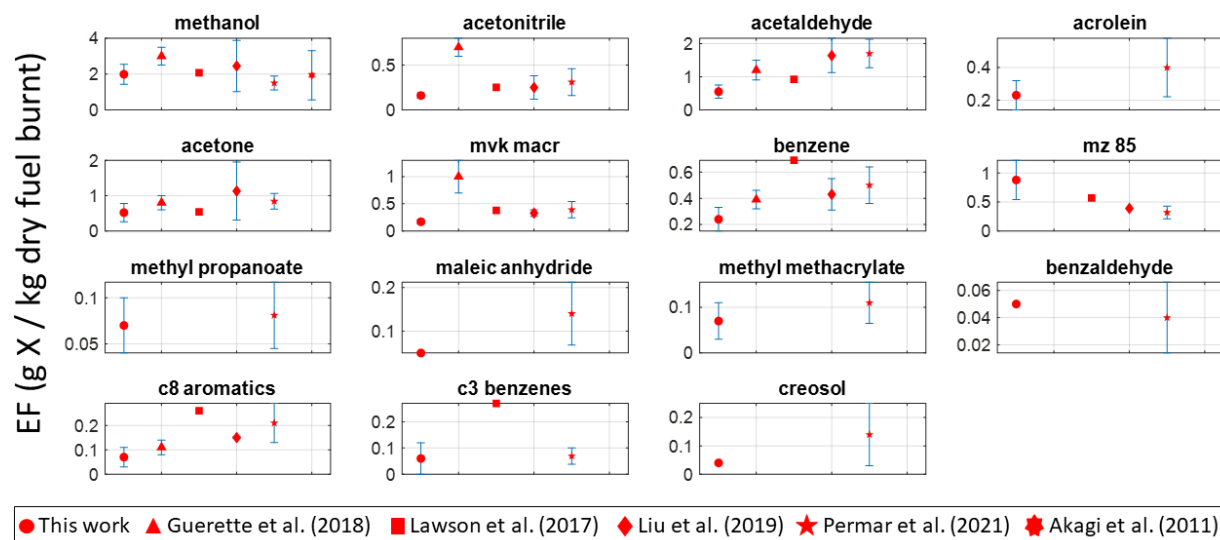
**Figure A.7** Comparison of ERs derived from solely period D and from average of all periods. Standard deviation is reported for each average ER. If standard deviation is missing, then that compound had only one viable ER of the four periods.

**Table A.3** Emission ratios derived from averaging over periods A-D. Standard deviation is reported for each ER. Dashes indicated that only one of four periods had a viable ER.

<b>Compound</b>	<b>Formula</b>	<b>m/z</b>	<b>Emission Ratios (ppt ppbCO<sup>-1</sup>)</b>
Methanol	CH <sub>4</sub> OH+	33.00	17.97±5.08
Acetonitrile	C <sub>2</sub> H <sub>3</sub> NH+	42.03	1.11±0.19
Acetaldehyde	C <sub>2</sub> H <sub>4</sub> OH+	45.03	3.67±1.30
Acrolein	C <sub>3</sub> H <sub>4</sub> OH+	57.03	1.19±0.42
Acetone	C <sub>3</sub> H <sub>6</sub> OH+	59.05	2.70±1.36
MVK+MACR	C <sub>4</sub> H <sub>6</sub> OH+	71.05	0.71±0.13
Benzene	C <sub>6</sub> H <sub>6</sub> H+	79.05	0.93±0.28
m/z 85	C <sub>4</sub> H <sub>4</sub> O <sub>2</sub> H+	85.03	2.84±0.91
Methyl propanoate	C <sub>4</sub> H <sub>8</sub> O <sub>2</sub> H+	89.06	0.21±0.10
Maleic anhydride	C <sub>4</sub> H <sub>2</sub> O <sub>3</sub> H+	99.00	0.14±--
Methyl methacrylate	C <sub>5</sub> H <sub>8</sub> O <sub>2</sub> H+	101.06	0.19±0.12
Benzaldehyde	C <sub>7</sub> H <sub>6</sub> OH+	107.05	0.14±--
C <sub>8</sub> -aromatics	C <sub>8</sub> H <sub>10</sub> H+	107.09	0.22±0.13
C <sub>3</sub> -benzene	C <sub>9</sub> H <sub>12</sub> H+	121.10	0.17±0.15
Creosol	C <sub>8</sub> H <sub>10</sub> O <sub>2</sub> H+	139.08	0.10±--

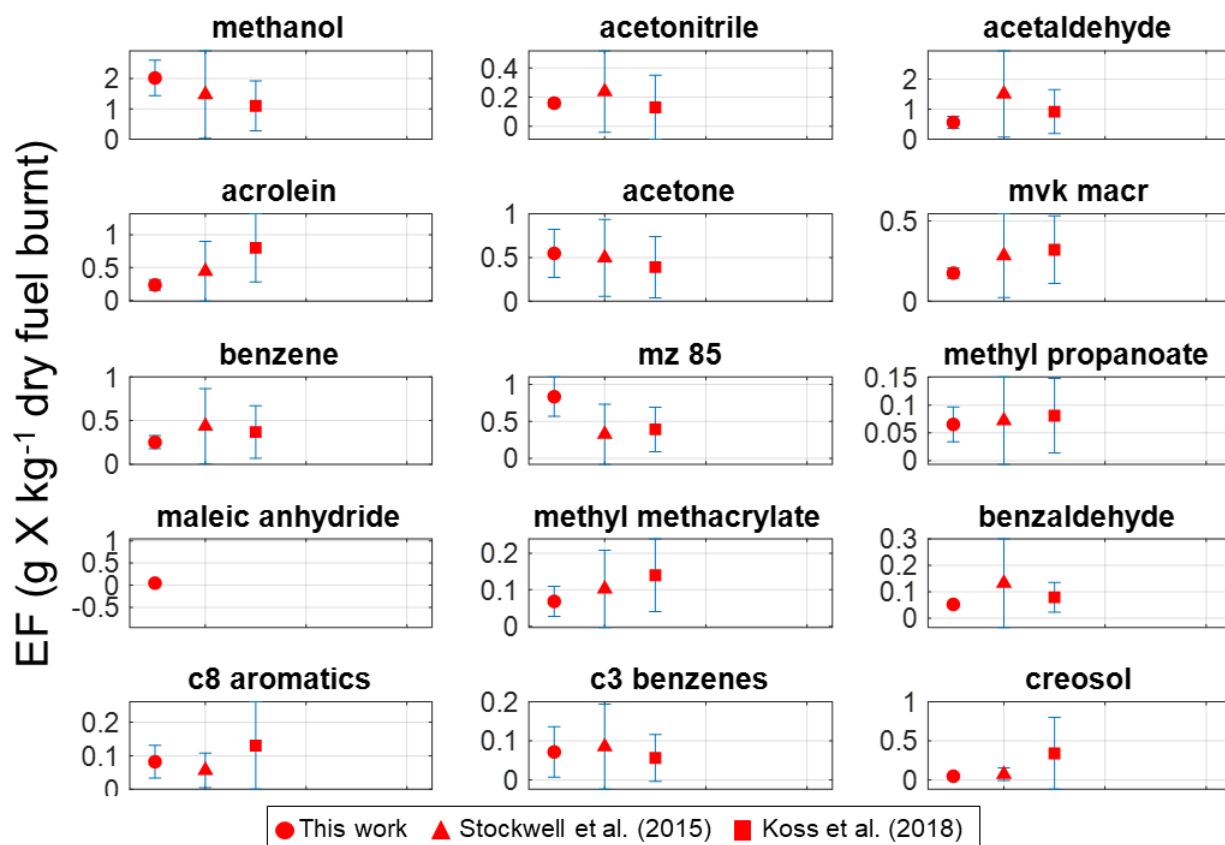
#### A.4 Supplementary analysis of emission factors

Figure A.8 shows the EFs and standard deviations from Table 2.1 in scatter plot form for better visualization of the comparison. An additional comparison of 12 of the 15 EFs derived in this work and those determined from lab studies is also provided in Figure A.9.



**Figure A.8** Scatter plot version of all reported emission factors and uncertainty plotted for all studies that this work was compared to.

EFs calculated from this work show excellent agreement with values from both Stockwell et al. (2015b) and Koss et al. (2018b) with values for each compound falling within  $1\sigma$  of each other. These results are unexpected as they indicate the ability to even employ lab-based, averaged EFs across geographically separate, analogous biomes.



**Figure A.9** Scatter plots showing EFs calculated in this work alongside those calculated from laboratory based, individual fuel type studies wherein the fuels are all located in temperate U.S. forests. Values from Koss et al. (2018) are the EF averages over all fuel types. Values from Stockwell et al. (2015) are determined from selecting a subgroup of fuel types present in temperate forests (e.g. excluding cooking emissions of fuel types from savannahs).

Table A.4 shows the EFs from this work and from three U.S.-based wildfire studies: Andreae (2019), Gkatzelis et al. (2024), and the Smoke Emissions Reference Application (SERA, Prichard et al. 2020). EFs from Andreae (2019) are from wildfire measurements stratified by biome and averaged over a global dataset. EFs from Gkatzelis et al. (2024) are derived from aircraft

measurements taken over U.S. temperate biomes during the 2019 FIREX-AQ campaign. The SERA database allows for the selection and averaging of U.S.-based EFs according to campaign and fire criteria (e.g. burn type, platform, region). SERA EFs shown here result from criteria selected to resemble the comparison U.S. aircraft campaigns (Permar et al., 2021, Gkatzelis et al., 2024) (conditions: Burn Type = Wildfire, Platform = airborne, Region = West, Vegetation Type = conifer forest, mixedwood forest). Each EF is averaged over results from 2-5 studies (Hegg, 1989; Radke, 1989; Babbitt, 1994; Urbanski, 2013; Lui et al., 2017).

**Table A.4** EFs  $\pm 1\sigma$  (g kg<sup>-1</sup>) from this work, two U.S.-based studies, and one global study for geographically distant temperate forests. \* Again, m/z 85 indicates the sum of furanone and cis-2-butenediol.

				<b>Biome</b>		
				<b>Location</b>		
			AU	AU	AU	Temperate Forests
<b>Compound</b>	<b>Formula</b>	<b>m/z</b>	<b>This work</b>	<b>Gkatzelis et al. (2024)</b>	<b>Lawson et al. (2015b)</b>	<b>Andreae (2019)</b>
Methanol	CH <sub>4</sub> O	33.00	2.01±0.58	1.42±0.66	2.45±1.17	2.20±0.9
Acetonitrile	C <sub>2</sub> H <sub>3</sub> N	42.03	0.16±0.03	0.32±0.14	0.25±0.11	0.22±0.17
Acetaldehyde	C <sub>2</sub> H <sub>4</sub> O	45.03	0.57±0.20	1.95±0.60	1.64±0.43	1.21±0.56
Acrolein	C <sub>3</sub> H <sub>4</sub> O	57.03	0.23±0.08	0.88±0.88	--	0.34±0.12
Acetone	C <sub>3</sub> H <sub>6</sub> O	59.05	0.55±0.28	0.93±0.34	--	0.76±0.50
MVK+MACR	C <sub>4</sub> H <sub>6</sub> O	71.05	0.18±0.03	0.71±0.27	0.33±0.04	0.14±0.18
Benzene	C <sub>6</sub> H <sub>6</sub>	79.05	0.25±0.08	0.69±0.17	0.43±0.1	0.42±0.17
m/z 85	C <sub>4</sub> H <sub>4</sub> O <sub>2</sub>	85.03	0.83±0.27	0.54±0.26	--	--
Methyl propanoate	C <sub>4</sub> H <sub>8</sub> O <sub>2</sub>	89.06	0.07±0.03	--	--	--
Maleic Anhydride	C <sub>4</sub> H <sub>2</sub> O <sub>3</sub>	99.00	0.05±--	--	--	--
Methyl methacrylate	C <sub>5</sub> H <sub>8</sub> O <sub>2</sub>	101.06	0.07±.04	--	--	--
Benzaldehyde	C <sub>7</sub> H <sub>6</sub> O	107.05	0.05±--	0.15±0.05	--	0.132±0.08
C8-aromatics	C <sub>8</sub> H <sub>10</sub>	107.09	0.08±0.05	0.08±0.04	0.038±0.002	0.16±0.09
C3-benzenes	C <sub>9</sub> H <sub>12</sub>	121.10	0.07±0.06	0.084±0.043	--	--
Creosol	C <sub>8</sub> H <sub>10</sub> O <sub>2</sub>	139.08	0.05±--	0.47±0.26	--	--

\* Dashes indicate either EF or EF variability not reported in study.

Figure A.10 shows the same EFs as Figure A.8, except values from Akagi et al. (2011) and Lui et al. (2017) have been removed, and those from Table A.4 are displayed. EFs are color coded by geography with global EFs shown in green, AU-based EFs in blue, and U.S.-based EFs in red. We note that the averaged SERA EFs include the values from Lui et al. (2017). The single methanol EF  $\pm 1\sigma$  from Akagi et al. (2011) is within both uncertainty and a factor of 2 of the corresponding EFs from Gkatzelis et al. (2024), SERA, and Andreae (2019).

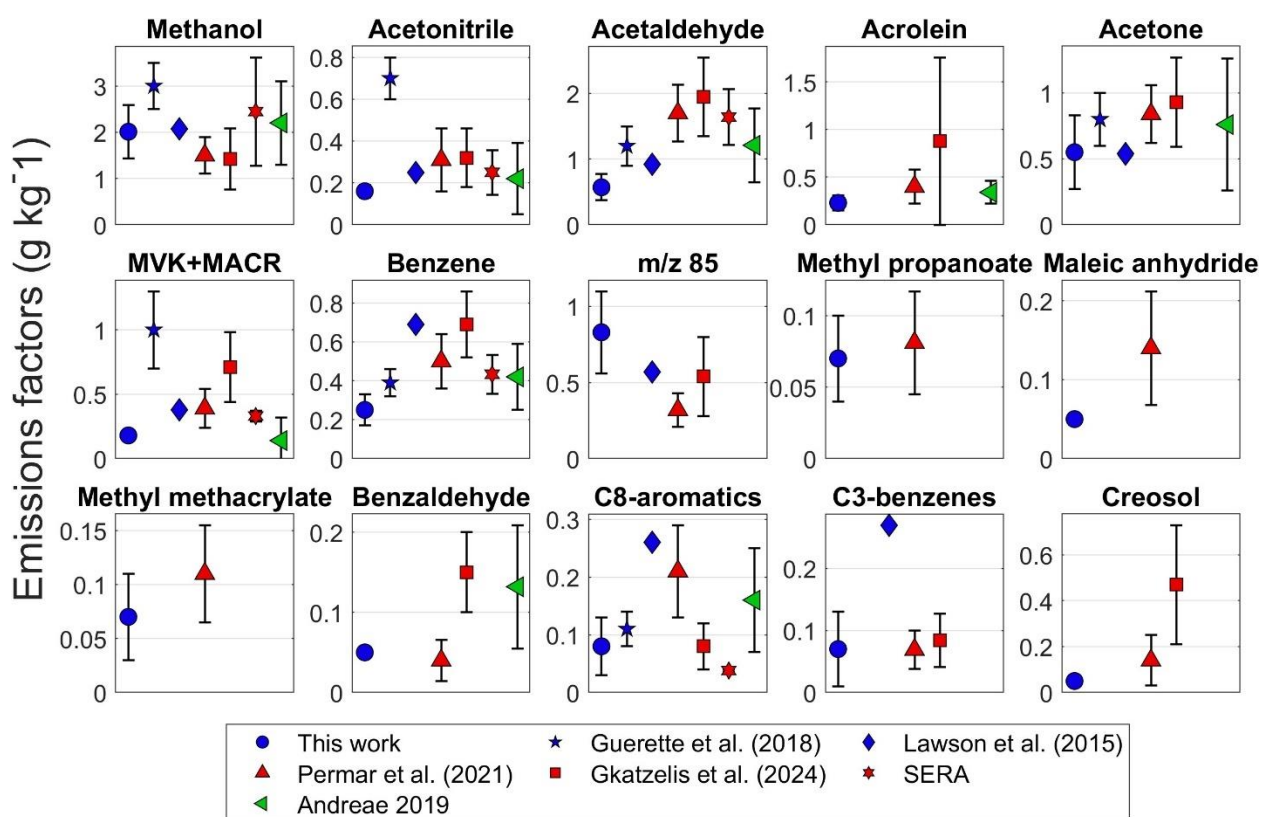


**Figure A.10** EFs from this work compared to six other studies – two conducted in biomes in Australia (blue), three conducted in or data was aggregated from biomes in the United States (red), and one that globally aggregated EFs based on biome.

10 of the 15 EFs in this work are lower than all three U.S.-based studies. Acetonitrile, acetone, and methyl propanoate exhibit the smallest relative differences in the range of -50 – -14%. Acrolein, MVK+MACR, benzene, methyl methacrylate, and creosol constitute a middle range with this work's EFs being smaller by -89 – -36%. Acetaldehyde and maleic anhydride typically show the largest disparities, being smaller by -71 – -64%. Given that our m/z 85 EF is the greatest of the four shown, the low bias in our EFs likely results from chemical aging. Global EFs and those from this work all show excellent agreement as they are within  $1\sigma$  and a factor of 2, though our EFs are notably lower for 6 of the 9 compounds (acetaldehyde, acrolein, acetone, benzene, benzaldehyde, and C<sub>8</sub>-aromatics). However, global EFs are within  $1\sigma$  of  $\geq 4$  other studies for all species which suggests that their lower limits may be useful as floors for discerning when a species has been too chemically depleted for EF derivation.

Differences between Australian-derived EFs and the U.S.-based and global EFs are generally the same as those discussed in section 2.6 except for C<sub>8</sub>-aromatics. Inclusion of Gkatzelis et al. (2024) and SERA EFs indicate that the EF from Lawson et al. (2015) is exceptionally high (up to a factor of 4 greater than U.S.-based studies, nearly 3 times greater than both Australian-based studies).

Two-thirds of our EFs ( $\pm 1\sigma$ ) are within EFs ( $\pm 1\sigma$ ) and from Gkatzelis et al. (2024), and one-half are within EFs ( $\pm 1\sigma$ ) (all are within a factor of 2) from the SERA EFs. These results overall continue to bolster confidence in the EFs derived in this work, and in the applicability of U.S.-based EFs for wildfire emissions modeling in temperate Australian biomes.

## APPENDIX B SUPPORTING INFORMATION FOR CHAPTER 4

### **B.1 Comparison with California airport NO<sub>2</sub> vertical profiles**

Figure B.1 shows median NO<sub>2</sub> vertical profiles binned in 150 m increments at ATL and the Los Angeles International (LAX) and Santa Barbara (SBA) airports. Median LAX and SBA profiles use measurements taken during the 2016 KORean and U.S. Air Quality (KORUS-AQ) campaign during a flight on Friday 17 June 2016 (Crawford et al., 2021). Several missed landing approaches were performed during this flight at airports across California, typically lasting 10-15 minutes. Measurements were taken from 10:00-11:00 LT and have been spatially selected to be within 20 km of the target airport. This provides observations up to 2.75 km for LAX and 2 km for SBA. The median ATL profile is derived using terminal-facing measurements from the month of June 2020 during the same local time of day. The surface layer concentration is assumed to be the same as the layer above it.

We note that historical meteorology data indicates that SBA experienced wildfire smoke throughout 17 June 2016 (Weather Underground, Santa Barbara municipal airport station: <https://www.wunderground.com/history/daily/us/ca/santa-barbara/KSBA/date/2016-6-17>) which potentially impacted NO<sub>2</sub> concentrations.

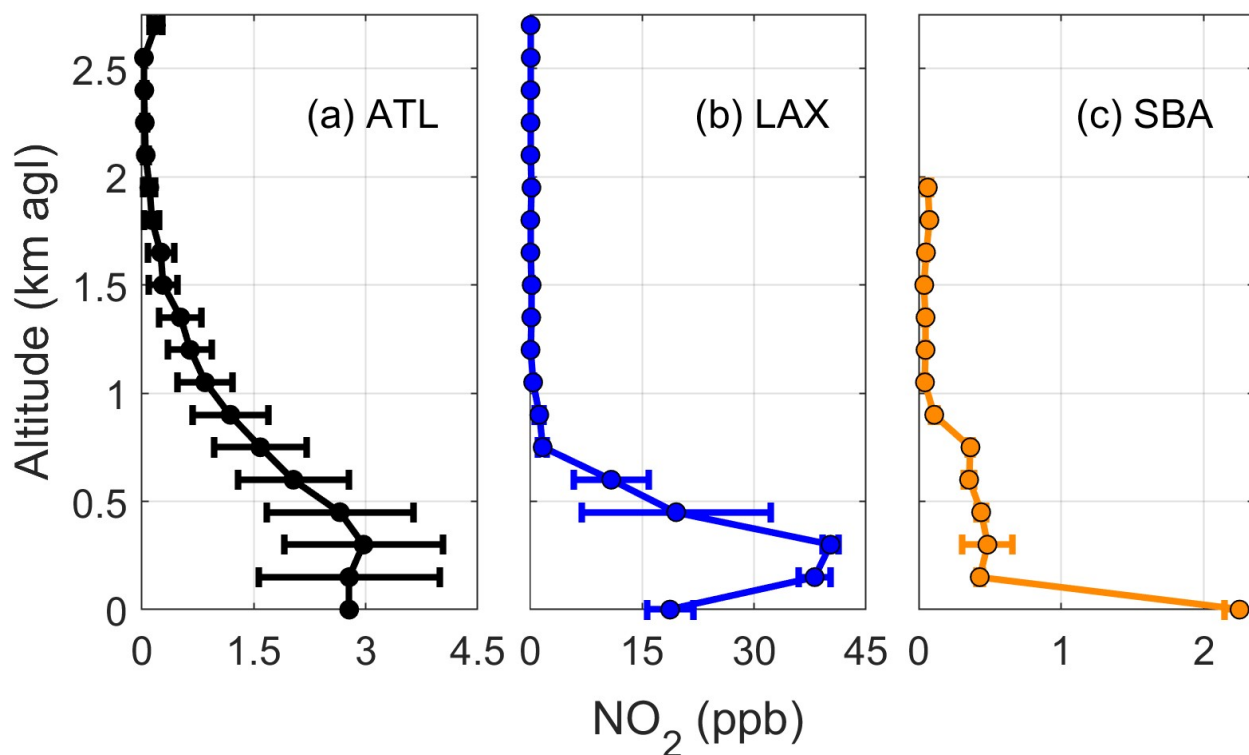


**Figure B.1** NO<sub>2</sub> vertical profiles at three U.S. airports at 10:00 LT. (a) shows the median vertical profile for the month of June 2020 at ATL. (b) and (c) show the median profiles at LAX and SBA, respectively, on 17 June 2016 from measurements taken during the KORUS-AQ campaign. Error bars are the median absolute deviation.

NO<sub>2</sub> profile maximums are observed at 3 ppb at 0.3 km (ATL), 40.2 ppb at 0.3 km (LAX), and 2.25 ppb at surface level (SBA). Of the three profiles, the ATL profile decays the slowest with altitude and allocates 88.2% of the tropospheric column below the first km. The LAX and SBA profiles allocate 99.5% and 93.2%, respectively, within the same distance. ATL and LAX both have the largest proportion of the NO<sub>2</sub> column at 0.3 km, with LAX (30.6%) nearly doubling that of ATL (15.6%). LAX is centrally located in currently one of the highest NO<sub>x</sub>-emitting cities in the U.S. (Fioletov et al. 2021). As such, high near-surface concentrations

are expected. However, we note that atmospheric conditions were cloudy over LAX at the time of observation (Weather Underground, LAX station:

<https://www.wunderground.com/history/daily/us/ca/los-angeles/KLAX/date/2016-6-17>) which could contribute to an accumulation of near-surface NO<sub>2</sub>.

The SBA profile shape deviates the most of the three, having the majority of the NO<sub>2</sub> column at the surface (46.2%). SBA resides in a smaller urban area with less urban emissions than Los Angeles and is surrounded by more forestry. Less NO<sub>2</sub> emissions and relatively greater biogenic VOC concentrations, particularly of isoprene, would lead to smaller concentrations near-surface. Profiles shapes in Figure B.1B and B.1C could indicate Pandora vertical profiles may not allocate enough of the tropospheric column near the surface over airports but more comparisons are needed to be conclusive.

## REFERENCES

- Abatzoglou, J. T., Williams, A. P., and Barbero, R.: Global emergence of anthropogenic climate change in fire weather indices, *Geophysical Research Letters*, 46, 326-336, 2019.
- Achatz, S., Lörinci, G., Hertkorn, N., Gebefügi, I., and Kettrup, A.: Disturbance of the determination of aldehydes and ketones: Structural elucidation of degradation products derived from the reaction of 2,4-dinitrophenylhydrazine (DNPH) with ozone, *Fresenius' Journal of Analytical Chemistry*, 364, 141-146, 10.1007/s002160051313, 1999.
- Adams, T. J., Geddes, J. A., and Lind, E. S.: New insights into the role of atmospheric transport and mixing on column and surface concentrations of NO<sub>2</sub> at a coastal urban site, *Journal of Geophysical Research: Atmospheres*, 128, e2022JD038237, 2023.
- Akagi, S., Yokelson, R. J., Wiedinmyer, C., Alvarado, M. J., Reid, J. S., Karl, T., Crouse, J. D., and Wennberg, P. O.: Emission factors for open and domestic biomass burning for use in atmospheric models, *Atmospheric Chemistry and Physics*, 11, 4039-4072, 2011a.
- Akagi, S. K., Yokelson, R. J., Wiedinmyer, C., Alvarado, M. J., Reid, J. S., Karl, T., Crouse, J. D., and Wennberg, P. O.: Emission factors for open and domestic biomass burning for use in atmospheric models, *Atmos. Chem. Phys.*, 11, 4039-4072, 10.5194/acp-11-4039-2011, 2011b.
- Akagi, S. K., Craven, J., Taylor, J., McMeeking, G., Yokelson, R., Burling, I., Urbanski, S., Wold, C., Seinfeld, J., and Coe, H.: Evolution of trace gases and particles emitted by a chaparral fire in California, *Atmospheric Chemistry and Physics*, 12, 1397-1421, 2012.
- Allan, D. W.: Statistics of atomic frequency standards, *Proceedings of the IEEE*, 54, 221-230, 1966.

- Alvarado, L. M., Richter, A., Vrekoussis, M., Hilboll, A., Kalisz Hedegaard, A. B., Schneising, O., and Burrows, J. P.: Unexpected long-range transport of glyoxal and formaldehyde observed from the Copernicus Sentinel-5 Precursor satellite during the 2018 Canadian wildfires, *Atmospheric Chemistry and Physics*, 20, 2057-2072, 2020.
- Alvarado, M., Logan, J., Mao, J., Apel, E., Riemer, D., Blake, D., Cohen, R., Min, K.-E., Perring, A., and Browne, E.: Nitrogen oxides and PAN in plumes from boreal fires during ARCTAS-B and their impact on ozone: an integrated analysis of aircraft and satellite observations, *Atmospheric Chemistry and Physics*, 10, 9739-9760, 2010.
- Andreae, M. O.: Emission of trace gases and aerosols from biomass burning—an updated assessment, *Atmospheric Chemistry and Physics*, 19, 8523-8546, 2019.
- Babbitt, R. E., Ward, D. E., Susott, R. A., Hao, W. M. and Baker, S. P.: Smoke From western wildfires, Proceedings of the 1994 Annual Meeting of Interior West Fire Council, Coeur d'Alene, Idaho,
- Behere, A., Lim, D., Kirby, M., and Mavris, D. N.: Alternate Departure Procedures for Takeoff Noise Mitigation at Atlanta Hartsfield-Jackson International Airport, AIAA Scitech 2019 Forum, 2090,
- Bent, J., Wallace, C., Lucic, G., Rella, C., Haffnagle, J., Baumann, K.: G2307: Traceable calibration of Formaldehyde (H<sub>2</sub>CO), White Paper, 2023.
- Berndt, T., Böge, O., and Rolle, W.: Products of the gas-phase reactions of NO<sub>3</sub> radicals with furan and tetramethylfuran, *Environmental science & technology*, 31, 1157-1162, 1997.

- Bierbach, A., Barnes, I., Becker, K. H., and Wiesen, E.: Atmospheric chemistry of unsaturated carbonyls: Butenedial, 4-oxo-2-pentenal, 3-hexene-2, 5-dione, maleic anhydride, 3H-furan-2-one, and 5-methyl-3H-furan-2-one, *Environmental science & technology*, 28, 715-729, 1994.
- Bloss, C., Wagner, V., Jenkin, M., Volkamer, R., Bloss, W., Lee, J., Heard, D., Wirtz, K., Martin-Reviejo, M., and Rea, G.: Development of a detailed chemical mechanism (MCMv3. 1) for the atmospheric oxidation of aromatic hydrocarbons, *Atmospheric Chemistry and Physics*, 5, 641-664, 2005.
- Bray, C. D., Battye, W. H., Aneja, V. P., and Schlesinger, W. H.: Global emissions of NH<sub>3</sub>, NO<sub>x</sub>, and N<sub>2</sub>O from biomass burning and the impact of climate change, *Journal of the Air & Waste Management Association*, 71, 102-114, 2021.
- Brey, S. J. and Fischer, E. V.: Smoke in the city: How often and where does smoke impact summertime ozone in the United States?, *Environmental science & technology*, 50, 1288-1294, 2016.
- Brilli, F., Gioli, B., Ciccioli, P., Zona, D., Loreto, F., Janssens, I. A., and Ceulemans, R.: Proton Transfer Reaction Time-of-Flight Mass Spectrometric (PTR-TOF-MS) determination of volatile organic compounds (VOCs) emitted from a biomass fire developed under stable nocturnal conditions, *Atmospheric Environment*, 97, 54-67, 2014.
- Bruns, E. A., Slowik, J. G., El Haddad, I., Kilic, D., Klein, F., Dommen, J., Temime-Roussel, B., Marchand, N., Baltensperger, U., and Prévôt, A. S.: Characterization of gas-phase organics using proton transfer reaction time-of-flight mass spectrometry: fresh and aged residential wood combustion emissions, *Atmospheric Chemistry and Physics*, 17, 705-720, 2017.

- Burling, I., Yokelson, R. J., Akagi, S., Urbanski, S., Wold, C. E., Griffith, D. W., Johnson, T. J., Reardon, J., and Weise, D.: Airborne and ground-based measurements of the trace gases and particles emitted by prescribed fires in the United States, *Atmospheric Chemistry and Physics*, 11, 12197-12216, 2011.
- Cardenas, L., Brassington, D., Allan, B., Coe, H., Alicke, B., Platt, U., Wilson, K., Plane, J., and Penkett, S.: Intercomparison of formaldehyde measurements in clean and polluted atmospheres, *Journal of Atmospheric Chemistry*, 37, 53-80, 2000.
- Cazorla, M., Wolfe, G., Bailey, S., Swanson, A., Arkinson, H., and Hanisco, T.: A new airborne laser-induced fluorescence instrument for in situ detection of formaldehyde throughout the troposphere and lower stratosphere, *Atmospheric Measurement Techniques*, 8, 541-552, 2015.
- Cede, A.: Manual for Blick Software Suite 1.8, 2021.
- Chang, D. Y., Yoon, J., Lelieveld, J., Park, S. K., Yum, S. S., Kim, J., and Jeong, S.: Direct radiative forcing of biomass burning aerosols from the extensive Australian wildfires in 2019–2020, *Environmental Research Letters*, 16, 044041, 2021.
- Coggon, M. M., Gkatzelis, G. I., McDonald, B. C., Gilman, J. B., Schwantes, R. H., Abuhassan, N., Aikin, K. C., Arend, M. F., Berkoff, T. A., and Brown, S. S.: Volatile chemical product emissions enhance ozone and modulate urban chemistry, *Proceedings of the National Academy of Sciences*, 118, e2026653118, <https://doi.org/10.1073/pnas.2026653118>, 2021.

- Coggon, M. M., Veres, P. R., Yuan, B., Koss, A., Warneke, C., Gilman, J. B., Lerner, B. M., Peischl, J., Aikin, K. C., and Stockwell, C. E.: Emissions of nitrogen-containing organic compounds from the burning of herbaceous and arboraceous biomass: Fuel composition dependence and the variability of commonly used nitrile tracers, *Geophysical Research Letters*, 43, 9903-9912, 2016.
- Crawford, J. H., Ahn, J.-Y., Al-Saadi, J., Chang, L., Emmons, L. K., Kim, J., Lee, G., Park, J.-H., Park, R. J., and Woo, J. H.: The Korea–United States air quality (KORUS-AQ) field study, *Elem Sci Anth*, 9, 00163, 2021.
- Damiani, A., Irie, H., Belikov, D. A., Kaizuka, S., Hoque, H. M. S., and Cordero, R. R.: Peculiar COVID-19 effects in the Greater Tokyo Area revealed by spatiotemporal variabilities of tropospheric gases and light-absorbing aerosols, *Atmospheric Chemistry and Physics*, 22, 12705-12726, 2022.
- Dang, R., Jacob, D. J., Shah, V., Eastham, S. D., Fritz, T. M., Mickley, L. J., Liu, T., Wang, Y., and Wang, J.: Background nitrogen dioxide (NO<sub>2</sub>) over the United States and its implications for satellite observations and trends: effects of nitrate photolysis, aircraft, and open fires, *Atmospheric chemistry and physics*, 23, 6271-6284, 2023.
- Dasgupta, P. K., Li, J., Zhang, G., Luke, W. T., McClenny, W. A., Stutz, J., and Fried, A.: Summertime ambient formaldehyde in five US metropolitan areas: Nashville, Atlanta, Houston, Philadelphia, and Tampa, *Environmental science & technology*, 39, 4767-4783, 2005.
- Davey, S. M. and Sarre, A.: the 2019/20 Black Summer bushfires, 2020.

- De Gouw, J., Gilman, J., Kim, S. W., Alvarez, S., Dusanter, S., Graus, M., Griffith, S., Isaacman-VanWertz, G., Kuster, W., and Lefer, B.: Chemistry of volatile organic compounds in the Los Angeles Basin: Formation of oxygenated compounds and determination of emission ratios, *Journal of Geophysical Research: Atmospheres*, 123, 2298-2319, 2018.
- Decker, Z. C., Robinson, M. A., Barsanti, K. C., Bourgeois, I., Coggon, M. M., DiGangi, J. P., Diskin, G. S., Flocke, F. M., Franchin, A., and Fredrickson, C. D.: Nighttime and daytime dark oxidation chemistry in wildfire plumes: an observation and model analysis of FIREX-AQ aircraft data, *Atmospheric Chemistry and Physics*, 21, 16293-16317, 2021.
- Decker, Z. C., Zarzana, K. J., Coggon, M., Min, K.-E., Pollack, I., Ryerson, T. B., Peischl, J., Edwards, P., Dubé, W. P., and Markovic, M. Z.: Nighttime chemical transformation in biomass burning plumes: a box model analysis initialized with aircraft observations, *Environmental Science & Technology*, 53, 2529-2538, 2019.
- Didan, K.: MODIS/Terra Vegetation Indices 16-Day L3 Global 250m SIN Grid V061, NASA EOSDIS Land Processes Distributed Active Archive Center [dataset], <https://doi.org/10.5067/MODIS/MOD13Q1.061>, 2021.
- Dimitropoulou, E., Hendrick, F., Pinardi, G., Friedrich, M. M., Merlaud, A., Tack, F., De Longueville, H., Fayt, C., Hermans, C., and Laffineur, Q.: Validation of TROPOMI tropospheric NO<sub>2</sub> columns using dual-scan multi-axis differential optical absorption spectroscopy (MAX-DOAS) measurements in Uccle, Brussels, *Atmospheric Measurement Techniques*, 13, 5165-5191, 2020.
- Donovan, V. M., Wonkka, C. L., and Twidwell, D.: Surging wildfire activity in a grassland biome, *Geophysical Research Letters*, 44, 5986-5993, 2017.

- Douros, J., Eskes, H., van Geffen, J., Boersma, K. F., Compernelle, S., Pinardi, G., Blechschmidt, A.-M., Peuch, V.-H., Colette, A., and Veefkind, P.: Comparing Sentinel-5P TROPOMI NO<sub>2</sub> column observations with the CAMS regional air quality ensemble, *Geoscientific Model Development*, 16, 509-534, 2023.
- Dugheri, S., Massi, D., Mucci, N., Marrubini, G., Cappelli, G., Speltini, A., Bonferoni, M. C., and Arcangeli, G.: Exposure to airborne formaldehyde: Sampling and analytical methods—A review, *Trends in Environmental Analytical Chemistry*, 29, e00116, <https://doi.org/10.1016/j.teac.2021.e00116>, 2021.
- Duncan, B. N., Lamsal, L. N., Thompson, A. M., Yoshida, Y., Lu, Z., Streets, D. G., Hurwitz, M. M., and Pickering, K. E.: A space-based, high-resolution view of notable changes in urban NO<sub>x</sub> pollution around the world (2005–2014), *Journal of Geophysical Research: Atmospheres*, 121, 976-996, 2016.
- Dunne, E., Galbally, I. E., Cheng, M., Selleck, P., Molloy, S. B., and Lawson, S. J.: Comparison of VOC measurements made by PTR-MS, adsorbent tubes–GC-FID-MS and DNPH derivatization–HPLC during the Sydney Particle Study, 2012: a contribution to the assessment of uncertainty in routine atmospheric VOC measurements, *Atmos. Meas. Tech.*, 11, 141-159, 10.5194/amt-11-141-2018, 2018.
- Eskes, H., van Geffen, J., Boersma, F., Eichmann, K., Apituley, A., Pedergnana, M., Sneep, M., Veefkind, P., Loyola, D.: Sentinel-5 precursor/TROPOMI Level 2 Product User Manual Nitrogen dioxide, 2022.
- Esri, E. G. a. t. G. u. c.: ESRI World Imagery,

- Fairman, T. A., Nitschke, C. R., and Bennett, L. T.: Too much, too soon? A review of the effects of increasing wildfire frequency on tree mortality and regeneration in temperate eucalypt forests, *International journal of wildland fire*, 25, 831-848, 2015.
- Filkov, A. I., Ngo, T., Matthews, S., Telfer, S., and Penman, T. D.: Impact of Australia's catastrophic 2019/20 bushfire season on communities and environment. Retrospective analysis and current trends, *Journal of safety science and resilience*, 1, 44-56, 2020.
- Fioletov, V., McLinden, C. A., Griffin, D., Krotkov, N., Liu, F., and Eskes, H.: Quantifying urban, industrial, and background changes in NO<sub>2</sub> during the COVID-19 lockdown period based on TROPOMI satellite observations, *Atmos. Chem. Phys. Discuss.*, 2021, 1-48, 10.5194/acp-2021-536, 2021.
- Ford, B., Val Martin, M., Zelasky, S., Fischer, E., Anenberg, S., Heald, C. L., and Pierce, J.: Future fire impacts on smoke concentrations, visibility, and health in the contiguous United States, *GeoHealth*, 2, 229-247, 2018.
- Fried, A., Walega, J., Weibring, P., Richter, D., Simpson, I. J., Blake, D. R., Blake, N. J., Meinardi, S., Barletta, B., and Hughes, S. C.: Airborne formaldehyde and volatile organic compound measurements over the Daesan petrochemical complex on Korea's northwest coast during the Korea-United States Air Quality study Estimation of emission fluxes and effects on air quality, *Elementa: Science of the Anthropocene*, 8, <https://doi.org/10.1525/elementa.2020.121>, 2020.
- Frieß, U., Beirle, S., Alvarado Bonilla, L., Bösch, T., Friedrich, M. M., Hendrick, F., Piters, A., Richter, A., Van Roozendaal, M., and Rozanov, V. V.: Intercomparison of MAX-DOAS vertical profile retrieval algorithms: studies using synthetic data, *Atmospheric Measurement Techniques*, 12, 2155-2181, 2019.

- Furdyna, P.: Experiences with Picarro G2307 HCHO Analyzers, New York Department of Environmental Conservation, 2020.
- Gelaro, R., McCarty, W., Suárez, M. J., Todling, R., Molod, A., Takacs, L., Randles, C. A., Darmenov, A., Bosilovich, M. G., and Reichle, R.: The modern-era retrospective analysis for research and applications, version 2 (MERRA-2), *Journal of climate*, 30, 5419-5454, 2017.
- Gilman, J., Lerner, B., Kuster, W., Goldan, P., Warneke, C., Veres, P., Roberts, J., De Gouw, J., Burling, I., and Yokelson, R.: Biomass burning emissions and potential air quality impacts of volatile organic compounds and other trace gases from fuels common in the US, *Atmospheric Chemistry and Physics*, 15, 13915-13938, 2015.
- Gkatzelis, G. I., Coggon, M. M., Stockwell, C. E., Hornbrook, R. S., Allen, H., Apel, E. C., Bela, M. M., Blake, D. R., Bourgeois, I., and Brown, S. S.: Parameterizations of US wildfire and prescribed fire emission ratios and emission factors based on FIREX-AQ aircraft measurements, *Atmospheric Chemistry and Physics*, 24, 929-956, 2024.
- Glowania, M., Rohrer, F., Dorn, H. P., Hofzumahaus, A., Holland, F., Kiendler-Scharr, A., Wahner, A., and Fuchs, H.: Comparison of formaldehyde measurements by Hantzsch, CRDS and DOAS in the SAPHIR chamber, *Atmos. Meas. Tech.*, 14, 4239-4253, 10.5194/amt-14-4239-2021, 2021.
- Goldberg, D. L., Anenberg, S. C., Griffin, D., McLinden, C. A., Lu, Z., and Streets, D. G.: Disentangling the Impact of the COVID-19 Lockdowns on Urban NO<sub>2</sub> From Natural Variability, *Geophysical Research Letters*, 47, e2020GL089269, <https://doi.org/10.1029/2020GL089269>, 2020.

- Goldberg, D. L., Harkey, M., de Foy, B., Judd, L., Johnson, J., Yarwood, G., and Holloway, T.: Evaluating NO<sub>x</sub> emissions and their effect on O<sub>3</sub> production in Texas using TROPOMI NO<sub>2</sub> and HCHO, *Atmospheric Chemistry and Physics*, 22, 10875-10900, 2022.
- Gössling, S. and Humpe, A.: The global scale, distribution and growth of aviation: Implications for climate change, *Global Environmental Change*, 65, 102194, <https://doi.org/10.1016/j.gloenvcha.2020.102194>, 2020.
- Griffith, D., Deutscher, N., Caldow, C., Kettlewell, G., Riggenbach, M., and Hammer, S.: A Fourier transform infrared trace gas and isotope analyser for atmospheric applications, *Atmospheric Measurement Techniques*, 5, 2481-2498, 2012.
- Grosjean, D. and Williams II, E. L.: Environmental persistence of organic compounds estimated from structure-reactivity and linear free-energy relationships. Unsaturated aliphatics, *Atmospheric Environment. Part A. General Topics*, 26, 1395-1405, 1992.
- Guérette, E.-A., Paton-Walsh, C., Desservettaz, M., Smith, T. E., Volkova, L., Weston, C. J., and Meyer, C. P.: Emissions of trace gases from Australian temperate forest fires: emission factors and dependence on modified combustion efficiency, *Atmospheric Chemistry and Physics*, 18, 3717-3735, 2018a.
- Guérette, E. A., Paton-Walsh, C., Desservettaz, M., Smith, T. E. L., Volkova, L., Weston, C. J., and Meyer, C. P.: Emissions of trace gases from Australian temperate forest fires: emission factors and dependence on modified combustion efficiency, *Atmos. Chem. Phys.*, 18, 3717-3735, [10.5194/acp-18-3717-2018](https://doi.org/10.5194/acp-18-3717-2018), 2018b.

- Hak, C., Pundt, I., Trick, S., Kern, C., Platt, U., Dommen, J., Ordóñez, C., Prévôt, A., Junkermann, W., and Astorga-Lloréns, C.: Intercomparison of four different in-situ techniques for ambient formaldehyde measurements in urban air, *Atmospheric Chemistry and Physics*, 5, 2881-2900, 2005.
- Hansen, R., Griffith, S., Dusanter, S., Rickly, P., Stevens, P., Bertman, S., Carroll, M., Erickson, M., Flynn, J., and Grossberg, N.: Measurements of total hydroxyl radical reactivity during CABINEX 2009–Part 1: field measurements, *Atmospheric Chemistry and Physics*, 14, 2923-2937, 2014.
- Hatch, L. E., Luo, W., Pankow, J. F., Yokelson, R. J., Stockwell, C. E., and Barsanti, K.: Identification and quantification of gaseous organic compounds emitted from biomass burning using two-dimensional gas chromatography–time-of-flight mass spectrometry, *Atmospheric Chemistry and Physics*, 15, 1865-1899, 2015.
- Hatch, L. E., Yokelson, R. J., Stockwell, C. E., Veres, P. R., Simpson, I. J., Blake, D. R., Orlando, J. J., and Barsanti, K. C.: Multi-instrument comparison and compilation of non-methane organic gas emissions from biomass burning and implications for smoke-derived secondary organic aerosol precursors, *Atmospheric Chemistry and Physics*, 17, 1471-1489, 2017.
- He, Y., Zhao, B., Wang, S., Valorso, R., Chang, X., Yin, D., Feng, B., Camredon, M., Aumont, B., and Dearden, A.: Formation of secondary organic aerosol from wildfire emissions enhanced by long-time ageing, *Nature Geoscience*, 17, 124-129, 2024.
- Hegg, D., Radke, L. F., Hobbs, P. V., Rasmussen, R. A., and Riggan, P. J.: Emissions of some trace gases from biomass fires, *Emissions of some trace gases from biomass fires*, Anaheim, CA,

- Herman, J., Cede, A., Spinei, E., Mount, G., Tzortziou, M., and Abuhassan, N.: NO<sub>2</sub> column amounts from ground-based Pandora and MFDOAS spectrometers using the direct-sun DOAS technique: Intercomparisons and application to OMI validation, *Journal of Geophysical Research: Atmospheres*, 114, <https://doi.org/10.1029/2009JD011848>, 2009.
- Herman, J., Abuhassan, N., Kim, J., Kim, J., Dubey, M., Raponi, M., and Tzortziou, M.: Underestimation of column NO<sub>2</sub> amounts from the OMI satellite compared to diurnally varying ground-based retrievals from multiple PANDORA spectrometer instruments, *Atmospheric Measurement Techniques*, 12, 5593-5612, 2019.
- Herndon, S. C., Zahniser, M. S., Nelson Jr, D. D., Shorter, J., McManus, J. B., Jiménez, R., Warneke, C., and De Gouw, J. A.: Airborne measurements of HCHO and HCOOH during the New England Air Quality Study 2004 using a pulsed quantum cascade laser spectrometer, *Journal of Geophysical Research: Atmospheres*, 112, <https://doi.org/10.1029/2006JD007600>, 2007.
- Herrington, J. S. and Hays, M. D.: Concerns regarding 24-h sampling for formaldehyde, acetaldehyde, and acrolein using 2, 4-dinitrophenylhydrazine (DNPH)-coated solid sorbents, *Atmospheric Environment*, 55, 179-184, 2012.
- Ho, S. S. H., Chow, J. C., Watson, J. G., Ip, H. S. S., Ho, K. F., Dai, W. T., and Cao, J.: Biases in ketone measurements using DNPH-coated solid sorbent cartridges, *Analytical Methods*, 6, 967-974, 2014.
- Huang, G., Ponder, R., Bond, A., Brim, H., Temeng, A., Naeger, A. R., and Zhu, L.: Unexpected impact of COVID-19 lockdown on the air quality in the metro Atlanta, USA using ground-based and satellite observations, *Aerosol and Air Quality Research*, 21, 210153, 2021.

- Ialongo, I., Virta, H., Eskes, H., Hovila, J., and Douros, J.: Comparison of TROPOMI/Sentinel-5 Precursor NO<sub>2</sub> observations with ground-based measurements in Helsinki, *Atmos. Meas. Tech.*, 13, 205-218, 10.5194/amt-13-205-2020, 2020.
- Ito, A. and Penner, J. E.: Global estimates of biomass burning emissions based on satellite imagery for the year 2000, *Journal of Geophysical Research: Atmospheres*, 109, 2004.
- Jaffe, D. A. and Wigder, N. L.: Ozone production from wildfires: A critical review, *Atmospheric Environment*, 51, 1-10, 2012.
- Janssens-Maenhout, G., Crippa, M., Guizzardi, D., Dentener, F., Muntean, M., Pouliot, G., Keating, T., Zhang, Q., Kurokawa, J., and Wankmüller, R.: HTAP\_v2. 2: a mosaic of regional and global emission grid maps for 2008 and 2010 to study hemispheric transport of air pollution, *Atmospheric Chemistry and Physics*, 15, 11411-11432, 2015.
- Jenkin, M. E., Saunders, S. M., and Pilling, M. J.: The tropospheric degradation of volatile organic compounds: a protocol for mechanism development, *Atmospheric Environment*, 31, 81-104, 1997.
- Jenkin, M. E., Saunders, S. M., Wagner, V., and Pilling, M. J.: Protocol for the development of the Master Chemical Mechanism, MCM v3 (Part B): tropospheric degradation of aromatic volatile organic compounds, *Atmospheric Chemistry and Physics*, 3, 181-193, 2003.
- Jersey, T. P. A. o. N. Y. a. N.: Airport Traffic Report, 2021.
- Jin, X., Zhu, Q., and Cohen, R. C.: Direct estimates of biomass burning NO<sub>x</sub> emissions and lifetimes using daily observations from TROPOMI, *Atmospheric Chemistry and Physics*, 21, 15569-15587, 2021.
- Jones, D. A., Wang, W., and Fawcett, R.: High-quality spatial climate data-sets for Australia, *Australian Meteorological and Oceanographic Journal*, 58, 233, 2009.

- Jones, M. W., Abatzoglou, J. T., Veraverbeke, S., Andela, N., Lasslop, G., Forkel, M., Smith, A. J., Burton, C., Betts, R. A., and van der Werf, G. R.: Global and regional trends and drivers of fire under climate change, *Reviews of Geophysics*, 60, e2020RG000726, 2022.
- Judd, L. M., Al-Saadi, J. A., Janz, S. J., Kowalewski, M. G., Pierce, R. B., Szykman, J. J., Valin, L. C., Swap, R., Cede, A., Mueller, M., Tiefengraber, M., Abuhassan, N., and Williams, D.: Evaluating the impact of spatial resolution on tropospheric NO<sub>2</sub> column comparisons within urban areas using high-resolution airborne data, *Atmos. Meas. Tech.*, 12, 6091-6111, 10.5194/amt-12-6091-2019, 2019.
- Judd, L. M., Al-Saadi, J. A., Szykman, J. J., Valin, L. C., Janz, S. J., Kowalewski, M. G., Eskes, H. J., Veefkind, J. P., Cede, A., Mueller, M., Gebetsberger, M., Swap, R., Pierce, R. B., Nowlan, C. R., Abad, G. G., Nehrir, A., and Williams, D.: Evaluating Sentinel-5P TROPOMI tropospheric NO<sub>2</sub> column densities with airborne and Pandora spectrometers near New York City and Long Island Sound, *Atmos. Meas. Tech. Discuss.*, 2020, 1-52, 10.5194/amt-2020-151, 2020.
- Karst, U., Binding, N., Cammann, K., and Witting, U.: Interferences of nitrogen dioxide in the determination of aldehydes and ketones by sampling on 2,4-dinitrophenylhydrazine-coated solid sorbent, *Fresenius' Journal of Analytical Chemistry*, 345, 48-52, 10.1007/BF00323325, 1993.
- Keller, C. A., Knowland, K. E., Duncan, B. N., Liu, J., Anderson, D. C., Das, S., Lucchesi, R. A., Lundgren, E. W., Nicely, J. M., and Nielsen, E.: Description of the NASA GEOS composition forecast modeling system GEOS-CF v1. 0, *Journal of Advances in Modeling Earth Systems*, 13, e2020MS002413, 2021.

- Keywood, M., Kanakidou, M., Stohl, A., Dentener, F., Grassi, G., Meyer, C., Torseth, K., Edwards, D., Thompson, A. M., and Lohmann, U.: Fire in the air: Biomass burning impacts in a changing climate, *Critical Reviews in Environmental Science and Technology*, 43, 40-83, 2013.
- Knorr, W., Jiang, L., and Arneth, A.: Climate, CO<sub>2</sub> and human population impacts on global wildfire emissions, *Biogeosciences*, 13, 267-282, 2016.
- Kodros, J. K., Papanastasiou, D. K., Paglione, M., Masiol, M., Squizzato, S., Florou, K., Skyllakou, K., Kaltsonoudis, C., Nenes, A., and Pandis, S. N.: Rapid dark aging of biomass burning as an overlooked source of oxidized organic aerosol, *Proceedings of the National Academy of Sciences*, 117, 33028-33033, 2020.
- Koss, A. R., Sekimoto, K., Gilman, J. B., Selimovic, V., Coggon, M. M., Zarzana, K. J., Yuan, B., Lerner, B. M., Brown, S. S., and Jimenez, J. L.: Non-methane organic gas emissions from biomass burning: identification, quantification, and emission factors from PTR-ToF during the FIREX 2016 laboratory experiment, *Atmospheric Chemistry and Physics*, 18, 3299-3319, 2018a.
- Koss, A. R., Sekimoto, K., Gilman, J. B., Selimovic, V., Coggon, M. M., Zarzana, K. J., Yuan, B., Lerner, B. M., Brown, S. S., Jimenez, J. L., Krechmer, J., Roberts, J. M., Warneke, C., Yokelson, R. J., and de Gouw, J.: Non-methane organic gas emissions from biomass burning: identification, quantification, and emission factors from PTR-ToF during the FIREX 2016 laboratory experiment, *Atmos. Chem. Phys.*, 18, 3299-3319, 10.5194/acp-18-3299-2018, 2018b.

- Lamsal, L., Martin, R., Padmanabhan, A., Van Donkelaar, A., Zhang, Q., Sioris, C., Chance, K., Kurosu, T., and Newchurch, M.: Application of satellite observations for timely updates to global anthropogenic NO<sub>x</sub> emission inventories, *Geophysical Research Letters*, 38, 2011.
- Lange, K., Richter, A., Schönhardt, A., Meier, A. C., Bösch, T., Seyler, A., Krause, K., Behrens, L. K., Wittrock, F., and Merlaud, A.: Validation of Sentinel-5P TROPOMI tropospheric NO<sub>2</sub> products by comparison with NO<sub>2</sub> measurements from airborne imaging DOAS, ground-based stationary DOAS, and mobile car DOAS measurements during the S5P-VAL-DE-Ruhr campaign, *Atmospheric Measurement Techniques*, 16, 1357-1389, 2023.
- Laughner, J. L., Zare, A., and Cohen, R. C.: Effects of daily meteorology on the interpretation of space-based remote sensing of NO<sub>2</sub>, *Atmospheric Chemistry and Physics*, 16, 15247-15264, 2016.
- Lawal, A. S., Russell, A. G., and Kaiser, J.: Assessment of airport-related emissions and their impact on air quality in atlanta, ga, using cmaq and tropomi, *Environmental Science & Technology*, 56, 98-108, 2021.
- Lawson, S., Keywood, M., Galbally, I., Gras, J., Cainey, J., Cope, M., Krummel, P., Fraser, P., Steele, L., and Bentley, S.: Biomass burning emissions of trace gases and particles in marine air at Cape Grim, Tasmania, *Atmospheric Chemistry and Physics*, 15, 13393-13411, 2015a.
- Lawson, S. J., Cope, M., Lee, S., Galbally, I. E., Ristovski, Z., and Keywood, M. D.: Biomass burning at Cape Grim: exploring photochemistry using multi-scale modelling, *Atmospheric Chemistry and Physics*, 17, 11707-11726, 2017.

- Lawson, S. J., Keywood, M. D., Galbally, I. E., Gras, J. L., Caine, J. M., Cope, M. E., Krummel, P. B., Fraser, P. J., Steele, L. P., Bentley, S. T., Meyer, C. P., Ristovski, Z., and Goldstein, A. H.: Biomass burning emissions of trace gases and particles in marine air at Cape Grim, Tasmania, *Atmos. Chem. Phys.*, 15, 13393-13411, 10.5194/acp-15-13393-2015, 2015b.
- Liang, Y., Weber, R. J., Misztal, P. K., Jen, C. N., and Goldstein, A. H.: Aging of volatile organic compounds in October 2017 northern California wildfire plumes, *Environmental science & technology*, 56, 1557-1567, 2022.
- Lin, Y. C., Schwab, J. J., Demerjian, K. L., Bae, M. S., Chen, W. N., Sun, Y., Zhang, Q., Hung, H. M., and Perry, J.: Summertime formaldehyde observations in New York City: Ambient levels, sources and its contribution to HO<sub>x</sub> radicals, *Journal of Geophysical Research: Atmospheres*, 117, <https://doi.org/10.1029/2011JD016504>, 2012.
- Liu, X., Huey, L. G., Yokelson, R. J., Selimovic, V., Simpson, I. J., Müller, M., Jimenez, J. L., Campuzano-Jost, P., Beyersdorf, A. J., and Blake, D. R.: Airborne measurements of western US wildfire emissions: Comparison with prescribed burning and air quality implications, *Journal of Geophysical Research: Atmospheres*, 122, 6108-6129, 2017a.
- Liu, X., Zhang, Y., Huey, L., Yokelson, R., Wang, Y., Jimenez, J., Campuzano-Jost, P., Beyersdorf, A., Blake, D., and Choi, Y.: Agricultural fires in the southeastern US during SEAC4RS: Emissions of trace gases and particles and evolution of ozone, reactive nitrogen, and organic aerosol, *Journal of Geophysical Research: Atmospheres*, 121, 7383-7414, 2016.

- Liu, X., Huey, L. G., Yokelson, R. J., Selimovic, V., Simpson, I. J., Müller, M., Jimenez, J. L., Campuzano-Jost, P., Beyersdorf, A. J., Blake, D. R., Butterfield, Z., Choi, Y., Crouse, J. D., Day, D. A., Diskin, G. S., Dubey, M. K., Fortner, E., Hanisco, T. F., Hu, W., King, L. E., Kleinman, L., Meinardi, S., Mikoviny, T., Onasch, T. B., Palm, B. B., Peischl, J., Pollack, I. B., Ryerson, T. B., Sachse, G. W., Sedlacek, A. J., Shilling, J. E., Springston, S., St. Clair, J. M., Tanner, D. J., Teng, A. P., Wennberg, P. O., Wisthaler, A., and Wolfe, G. M.: Airborne measurements of western U.S. wildfire emissions: Comparison with prescribed burning and air quality implications, *Journal of Geophysical Research: Atmospheres*, 122, 6108-6129, <https://doi.org/10.1002/2016JD026315>, 2017b.
- Luecken, D., Napelenok, S., Strum, M., Scheffe, R., and Phillips, S.: Sensitivity of ambient atmospheric formaldehyde and ozone to precursor species and source types across the United States, *Environmental science & technology*, 52, 4668-4675, 2018.
- Lui, K. H., Ho, S. S. H., Louie, P. K. K., Chan, C. S., Lee, S. C., Hu, D., Chan, P. W., Lee, J. C. W., and Ho, K. F.: Seasonal behavior of carbonyls and source characterization of formaldehyde (HCHO) in ambient air, *Atmospheric Environment*, 152, 51-60, <https://doi.org/10.1016/j.atmosenv.2016.12.004>, 2017.
- MacSween, K., Paton-Walsh, C., Roulston, C., Guérette, E.-A., Edwards, G., Reisen, F., Desservettaz, M., Cameron, M., Young, E., and Kubistin, D.: Cumulative firefighter exposure to multiple toxins emitted during prescribed burns in Australia, *Exposure and Health*, 12, 721-733, 2020.

- Manion, J. A., Huie, R. E., Levin, R. D., Burgess Jr, D. R., Orkin, V. L., Tsang, W., McGivern, W. S., Hudgens, J. W., Knyazev, V. D., Atkinson, D. B., Chai, E., Tereza, A. M., Lin, C. Y., Allison, T. C., Mallard, W. G., Westley, F., Herron, J. T., Hampson, R. F., Frizzell, D. H.: NIST Chemical Kinetics Database (2015.09) [dataset], 2015.
- Marais, E. A., Roberts, J. F., Ryan, R. G., Eskes, H., Boersma, K. F., Choi, S., Joiner, J., Abuhassan, N., Redondas, A., and Grutter, M.: New observations of NO<sub>2</sub> in the upper troposphere from TROPOMI, *Atmospheric Measurement Techniques*, 14, 2389-2408, 2021.
- Müller, M., Anderson, B. E., Beyersdorf, A. J., Crawford, J. H., Diskin, G. S., Eichler, P., Fried, A., Keutsch, F. N., Mikoviny, T., and Thornhill, K. L.: In situ measurements and modeling of reactive trace gases in a small biomass burning plume, *Atmospheric Chemistry and Physics*, 16, 3813-3824, 2016.
- O'Dell, K., Hornbrook, R. S., Permar, W., Levin, E. J., Garofalo, L. A., Apel, E. C., Blake, N. J., Jarnot, A., Pothier, M. A., and Farmer, D. K.: Hazardous air pollutants in fresh and aged western US wildfire smoke and implications for long-term exposure, *Environmental Science & Technology*, 54, 11838-11847, 2020.
- Oak, Y. J., Park, R. J., Schroeder, J. R., Crawford, J. H., Blake, D. R., Weinheimer, A. J., Woo, J.-H., Kim, S.-W., Yeo, H., and Fried, A.: Evaluation of simulated O<sub>3</sub> production efficiency during the KORUS-AQ campaign: Implications for anthropogenic NO<sub>x</sub> emissions in Korea, *Elem Sci Anth*, 7, 56, 2019.
- Pagonis, D., Sekimoto, K., and de Gouw, J.: A library of proton-transfer reactions of H<sub>3</sub>O<sup>+</sup> ions used for trace gas detection, *Journal of the American Society for Mass Spectrometry*, 30, 1330-1335, 2019.

- Palm, B. B., Peng, Q., Fredrickson, C. D., Lee, B. H., Garofalo, L. A., Pothier, M. A., Kreidenweis, S. M., Farmer, D. K., Pokhrel, R. P., and Shen, Y.: Quantification of organic aerosol and brown carbon evolution in fresh wildfire plumes, *Proceedings of the National Academy of Sciences*, 117, 29469-29477, 2020.
- Palmer, P. I., Abbot, D. S., Fu, T. M., Jacob, D. J., Chance, K., Kurosu, T. P., Guenther, A., Wiedinmyer, C., Stanton, J. C., and Pilling, M. J.: Quantifying the seasonal and interannual variability of North American isoprene emissions using satellite observations of the formaldehyde column, *Journal of Geophysical Research: Atmospheres*, 111, 2006.
- Palmer, P. I., Jacob, D. J., Chance, K., Martin, R. V., Spurr, R. J., Kurosu, T. P., Bey, I., Yantosca, R., Fiore, A., and Li, Q.: Air mass factor formulation for spectroscopic measurements from satellites: Application to formaldehyde retrievals from the Global Ozone Monitoring Experiment, *Journal of Geophysical Research: Atmospheres*, 106, 14539-14550, 2001.
- Park, H.-J., Park, J.-S., Kim, S.-W., Chong, H., Lee, H., Kim, H., Ahn, J.-Y., Kim, D.-G., Kim, J., and Park, S. S.: Retrieval of NO<sub>2</sub> column amounts from ground-based hyperspectral imaging sensor measurements, *Remote Sensing*, 11, 3005, 2019.
- Parrish, D., Ryerson, T., Mellqvist, J., Johansson, J., Fried, A., Richter, D., Walega, J., Washenfelder, R. d., De Gouw, J., and Peischl, J.: Primary and secondary sources of formaldehyde in urban atmospheres: Houston Texas region, *Atmospheric Chemistry and Physics*, 12, 3273-3288, 2012.
- Paton-Walsh, C., Smith, T., Young, E., Griffith, D. W., and Guérette, É.-A.: New emission factors for Australian vegetation fires measured using open-path Fourier transform infrared spectroscopy—Part 1: Methods and Australian temperate forest fires, *Atmospheric Chemistry and Physics*, 14, 11313-11333, 2014.

- Pei, J., Han, X., and Lu, Y.: Performance and kinetics of catalytic oxidation of formaldehyde over copper manganese oxide catalyst, *Building and Environment*, 84, 134-141, 2015.
- Permar, W., Wang, Q., Selimovic, V., Wielgasz, C., Yokelson, R. J., Hornbrook, R. S., Hills, A. J., Apel, E. C., Ku, I. T., and Zhou, Y.: Emissions of trace organic gases from Western US wildfires based on WE-CAN aircraft measurements, *Journal of Geophysical Research: Atmospheres*, 126, e2020JD033838, 2021a.
- Permar, W., Wang, Q., Selimovic, V., Wielgasz, C., Yokelson, R. J., Hornbrook, R. S., Hills, A. J., Apel, E. C., Ku, I.-T., Zhou, Y., Sive, B. C., Sullivan, A. P., Collett Jr, J. L., Campos, T. L., Palm, B. B., Peng, Q., Thornton, J. A., Garofalo, L. A., Farmer, D. K., Kreidenweis, S. M., Levin, E. J. T., DeMott, P. J., Flocke, F., Fischer, E. V., and Hu, L.: Emissions of Trace Organic Gases From Western U.S. Wildfires Based on WE-CAN Aircraft Measurements, *Journal of Geophysical Research: Atmospheres*, 126, e2020JD033838, <https://doi.org/10.1029/2020JD033838>, 2021b.
- Phaka, R. Y., Merlaud, A., Pinaridi, G., Friedrich, M. M., Van Roozendael, M., Müller, J.-F., Stavrou, T., De Smedt, I., Hendrick, F., and Dimitropoulou, E.: Ground-based Multi-AXis Differential Optical Absorption Spectroscopy (MAX-DOAS) observations of NO<sub>2</sub> and H<sub>2</sub>CO at Kinshasa and comparisons with TROPOMI observations, 2023.
- Pinaridi, G., Van Roozendael, M., Hendrick, F., Theys, N., Abuhassan, N., Bais, A., Boersma, F., Cede, A., Chong, J., and Donner, S.: Validation of tropospheric NO<sub>2</sub> column measurements of GOME-2A and OMI using MAX-DOAS and direct sun network observations, *Atmospheric Measurement Techniques*, 13, 6141-6174, 2020.

- Prichard, S. J., O'Neill, S. M., Eagle, P., Andreu, A. G., Drye, B., Dubow, J., Urbanski, S., and Strand, T. M.: Wildland fire emission factors in North America: synthesis of existing data, measurement needs and management applications, *International Journal of Wildland Fire*, 29, 132-147, 2020.
- Pseftogkas, A., Koukouli, M.-E., Segers, A., Manders, A., Geffen, J. v., Balis, D., Meleti, C., Stavrou, T., and Eskes, H.: Comparison of S5P/TROPOMI Inferred NO<sub>2</sub> Surface Concentrations with In Situ Measurements over Central Europe, *Remote Sensing*, 14, 4886, 2022.
- Quadros, F. D., Snellen, M., and Dedoussi, I. C.: Regional sensitivities of air quality and human health impacts to aviation emissions, *Environmental Research Letters*, 15, 105013, 2020.
- Radke, L. F., Hegg, D. A., Lyons, J. H., Brock, P. V., Weiss, R. E., and Rasmussen, R. A.: Airborne measurements on smokes from biomass burning, *Aerosols and climate*, 411-422, 1989.
- Riess, T. C. V. W., Boersma, K. F., Van Roy, W., De Laat, J., Dammers, E., and van Vliet, J.: To new heights by flying low: comparison of aircraft vertical NO<sub>2</sub> profiles to model simulations and implications for TROPOMI NO<sub>2</sub> retrievals, *Atmospheric Measurement Techniques*, 16, 5287-5304, 2023.
- Robinson, M. A., Decker, Z. C., Barsanti, K. C., Coggon, M. M., Flocke, F. M., Franchin, A., Fredrickson, C. D., Gilman, J. B., Gkatzelis, G. I., and Holmes, C. D.: Variability and time of day dependence of ozone photochemistry in western wildfire plumes, *Environmental Science & Technology*, 55, 10280-10290, 2021.

- Saunders, S. M., Jenkin, M. E., Derwent, R. G., and Pilling, M. J.: Protocol for the development of the Master Chemical Mechanism, MCM v3 (Part A): tropospheric degradation of non-aromatic volatile organic compounds, *Atmospheric Chemistry and Physics*, 3, 161-180, 2003.
- Scheffe, R. D., Strum, M., Phillips, S. B., Thurman, J., Eyth, A., Fudge, S., Morris, M., Palma, T., and Cook, R.: Hybrid modeling approach to estimate exposures of hazardous air pollutants (HAPs) for the national air toxics assessment (NATA), *Environmental Science & Technology*, 50, 12356-12364, 2016.
- Sekimoto, K., Li, S.-M., Yuan, B., Koss, A., Coggon, M., Warneke, C., and de Gouw, J.: Calculation of the sensitivity of proton-transfer-reaction mass spectrometry (PTR-MS) for organic trace gases using molecular properties, *International Journal of Mass Spectrometry*, 421, 71-94, 2017.
- Sekimoto, K., Koss, A. R., Gilman, J. B., Selimovic, V., Coggon, M. M., Zarzana, K. J., Yuan, B., Lerner, B. M., Brown, S. S., and Warneke, C.: High-and low-temperature pyrolysis profiles describe volatile organic compound emissions from western US wildfire fuels, *Atmospheric Chemistry and Physics*, 18, 9263-9281, 2018.
- Selimovic, V., Yokelson, R. J., Warneke, C., Roberts, J. M., De Gouw, J., Reardon, J., and Griffith, D. W.: Aerosol optical properties and trace gas emissions by PAX and OP-FTIR for laboratory-simulated western US wildfires during FIREX, *Atmospheric Chemistry and Physics*, 18, 2929-2948, 2018.

- Shah, V., Jacob, D. J., Dang, R., Lamsal, L. N., Strode, S. A., Steenrod, S. D., Boersma, K. F., Eastham, S. D., Fritz, T. M., and Thompson, C.: Nitrogen oxides in the free troposphere: implications for tropospheric oxidants and the interpretation of satellite NO<sub>2</sub> measurements, *Atmospheric Chemistry and Physics*, 23, 1227-1257, 2023.
- Shutter, J. D., Allen, N. T., Hanisco, T. F., Wolfe, G. M., St. Clair, J. M., and Keutsch, F. N.: A new laser-based and ultra-portable gas sensor for indoor and outdoor formaldehyde (HCHO) monitoring, *Atmos. Meas. Tech.*, 12, 6079-6089, 10.5194/amt-12-6079-2019, 2019.
- Silvern, R. F., Jacob, D. J., Mickley, L. J., Sulprizio, M. P., Travis, K. R., Marais, E. A., Cohen, R. C., Laughner, J. L., Choi, S., and Joiner, J.: Using satellite observations of tropospheric NO<sub>2</sub> columns to infer long-term trends in US NO<sub>x</sub> emissions: the importance of accounting for the free tropospheric NO<sub>2</sub> background, *Atmospheric Chemistry and Physics*, 19, 8863-8878, 2019.
- Simmons, J. B., Paton-Walsh, C., Mouat, A. P., Kaiser, J., Humphries, R. S., Keywood, M., Griffith, D. W., Sutresna, A., Naylor, T., and Ramirez-Gamboa, J.: Bushfire smoke plume composition and toxicological assessment from the 2019–2020 Australian Black Summer, *Air Quality, Atmosphere & Health*, 15, 2067-2089, 2022.
- Sinreich, R., Merten, A., Molina, L., and Volkamer, R.: Parameterizing radiative transfer to convert MAX-DOAS dSCDs into near-surface box-averaged mixing ratios, *Atmospheric Measurement Techniques*, 6, 1521-1532, 2013.
- Sokolik, I., Soja, A., DeMott, P., and Winker, D.: Progress and challenges in quantifying wildfire smoke emissions, their properties, transport, and atmospheric impacts, *Journal of Geophysical Research: Atmospheres*, 124, 13005-13025, 2019.

- Solomon, P. A., Chameides, W., Weber, R., Middlebrook, A., Kiang, C., Russell, A. G., Butler, A., Turpin, B., Mikel, D., and Scheffe, R.: Overview of the 1999 Atlanta supersite project, *Journal of Geophysical Research: Atmospheres*, 108, <https://doi.org/10.1029/2001JD001458>, 2003.
- Souza, M. d. O., Sánchez, B., Fuentes, M., Gilaranz, J., and Canela, M. C.: Analytical validation using a gas mixing system for the determination of gaseous formaldehyde, *Analytical Methods*, 12, 5247-5256, 2020.
- Spinei, E., Tiefengraber, M., Müller, M., Gebetsberger, M., Cede, A., Valin, L., Szykman, J., Whitehill, A., Kotsakis, A., Santos, F., Abbuhasan, N., Zhao, X., Fioletov, V., Lee, S. C., and Swap, R.: Effect of Polyoxymethylene (POM-H Delrin) offgassing within Pandora head sensor on direct sun and multi-axis formaldehyde column measurements in 2016-2019, *Atmos. Meas. Tech. Discuss.*, 2020, 1-24, [10.5194/amt-2020-158](https://doi.org/10.5194/amt-2020-158), 2020.
- Spinei, E., Whitehill, A., Fried, A., Tiefengraber, M., Knepp, T. N., Herndon, S., Herman, J. R., Müller, M., Abuhassan, N., Cede, A., Richter, D., Walega, J., Crawford, J., Szykman, J., Valin, L., Williams, D. J., Long, R., Swap, R. J., Lee, Y., Nowak, N., and Poche, B.: The first evaluation of formaldehyde column observations by improved Pandora spectrometers during the KORUS-AQ field study, *Atmos. Meas. Tech.*, 11, 4943-4961, [10.5194/amt-11-4943-2018](https://doi.org/10.5194/amt-11-4943-2018), 2018.
- St Clair, J. M., Swanson, A. K., Bailey, S. A., and Hanisco, T. F.: CAFE: A new, improved nonresonant laser-induced fluorescence instrument for airborne in situ measurement of formaldehyde, *Atmospheric Measurement Techniques*, 12, 4581-4590, 2019.

- Stein, A. F., Draxler, R. R., Rolph, G. D., Stunder, B. J., Cohen, M. D., and Ngan, F.: NOAA's HYSPLIT atmospheric transport and dispersion modeling system, *Bulletin of the American Meteorological Society*, 96, 2059-2077, 2015.
- Stockwell, C., Veres, P., Williams, J., and Yokelson, R.: Characterization of biomass burning emissions from cooking fires, peat, crop residue, and other fuels with high-resolution proton-transfer-reaction time-of-flight mass spectrometry, *Atmospheric Chemistry and Physics*, 15, 845-865, 2015a.
- Stockwell, C. E., Veres, P. R., Williams, J., and Yokelson, R. J.: Characterization of biomass burning emissions from cooking fires, peat, crop residue, and other fuels with high-resolution proton-transfer-reaction time-of-flight mass spectrometry, *Atmos. Chem. Phys.*, 15, 845-865, 10.5194/acp-15-845-2015, 2015b.
- Strum, M. and Scheffe, R.: National review of ambient air toxics observations, *Journal of the Air & Waste Management Association*, 66, 120-133, 2016.
- Sun, K., Zhu, L., Cady-Pereira, K., Chan Miller, C., Chance, K., Clarisse, L., Coheur, P. F., González Abad, G., Huang, G., Liu, X., Van Damme, M., Yang, K., and Zondlo, M.: A physics-based approach to oversample multi-satellite, multispecies observations to a common grid, *Atmos. Meas. Tech.*, 11, 6679-6701, 10.5194/amt-11-6679-2018, 2018.
- Tang, S., Graham, L., Shen, L., Zhou, X., and Lanni, T.: Simultaneous determination of carbonyls and NO<sub>2</sub> in exhausts of heavy-duty diesel trucks and transit buses by HPLC following 2,4-dinitrophenylhydrazine cartridge collection, *Environmental science & technology*, 38, 5968-5976, 2004.

- Tirpitz, J.-L., Frieß, U., Hendrick, F., Alberti, C., Allaart, M., Apituley, A., Bais, A., Beirle, S., Berkhout, S., and Bogner, K.: Intercomparison of MAX-DOAS vertical profile retrieval algorithms: studies on field data from the CINDI-2 campaign, *Atmospheric Measurement Techniques Discussions*, 2020, 1-49, 2020.
- Tonnesen, G. S. and Dennis, R. L.: Analysis of radical propagation efficiency to assess ozone sensitivity to hydrocarbons and NO<sub>x</sub>: 1. Local indicators of instantaneous odd oxygen production sensitivity, *Journal of Geophysical Research: Atmospheres*, 105, 9213-9225, <https://doi.org/10.1029/1999JD900371>, 2000.
- Travis, K. R., Jacob, D. J., Fisher, J. A., Kim, P. S., Marais, E. A., Zhu, L., Yu, K., Miller, C. C., Yantosca, R. M., and Sulprizio, M. P.: Why do models overestimate surface ozone in the Southeast United States?, *Atmospheric Chemistry and Physics*, 16, 13561-13577, 2016.
- U.S. EPA: Compendium of Methods for the Determination of Toxic Organic Compounds in Ambient Air, 1999.
- Uchiyama, S., Naito, S., Matsumoto, M., Inaba, Y., and Kunugita, N.: Improved measurement of ozone and carbonyls using a dual-bed sampling cartridge containing trans-1, 2-bis (2-pyridyl) ethylene and 2, 4-dinitrophenylhydrazine-impregnated silica, *Analytical chemistry*, 81, 6552-6557, 2009.
- Urbanski, S.: Combustion efficiency and emission factors for wildfire-season fires in mixed conifer forests of the northern Rocky Mountains, US, *Atmospheric Chemistry and Physics*, 13, 7241-7262, 2013.
- Vairavamurthy, A., Roberts, J. M., and Newman, L.: Methods for determination of low molecular weight carbonyl compounds in the atmosphere: a review, *Atmospheric Environment. Part A. General Topics*, 26, 1965-1993, 1992.

- Valin, L., Fiore, A., Chance, K., and González Abad, G.: The role of OH production in interpreting the variability of CH<sub>2</sub>O columns in the southeast US, *Journal of Geophysical Research: Atmospheres*, 121, 478-493, 2016.
- Van der Werf, G. R., Randerson, J. T., Giglio, L., Collatz, G., Mu, M., Kasibhatla, P. S., Morton, D. C., DeFries, R., Jin, Y. v., and van Leeuwen, T. T.: Global fire emissions and the contribution of deforestation, savanna, forest, agricultural, and peat fires (1997–2009), *Atmospheric chemistry and physics*, 10, 11707-11735, 2010.
- van Geffen, J. H. G. M., Eskes, H. J., Boersma, K. F., Maasackers, J. D., and Veefkind, J. P.: TROPOMI ATBD of the total and tropospheric NO<sub>2</sub> data products., 2022.
- Verhoelst, T., Compernelle, S., Pinardi, G., Lambert, J. C., Eskes, H. J., Eichmann, K. U., Fjæraa, A. M., Granville, J., Niemeijer, S., Cede, A., Tiefengraber, M., Hendrick, F., Pazmiño, A., Bais, A., Bazureau, A., Boersma, K. F., Bogner, K., Dehn, A., Donner, S., Elokhov, A., Gebetsberger, M., Goutail, F., Grutter de la Mora, M., Gruzdev, A., Gratsea, M., Hansen, G. H., Irie, H., Jepsen, N., Kanaya, Y., Karagiozidis, D., Kivi, R., Kreher, K., Levelt, P. F., Liu, C., Müller, M., Navarro Comas, M., PETERS, A. J. M., Pommereau, J. P., Portafaix, T., Prados-Roman, C., Puentedura, O., Querel, R., Remmers, J., Richter, A., Rimmer, J., Rivera Cárdenas, C., Saavedra de Miguel, L., Sinyakov, V. P., Stremme, W., Strong, K., Van Roozendaal, M., Veefkind, J. P., Wagner, T., Wittrock, F., Yela González, M., and Zehner, C.: Ground-based validation of the Copernicus Sentinel-5P TROPOMI NO<sub>2</sub> measurements with the NDACC ZSL-DOAS, MAX-DOAS and Pandonia global networks, *Atmos. Meas. Tech.*, 14, 481-510, 10.5194/amt-14-481-2021, 2021.

- Verma, S., Worden, J., Pierce, B., Jones, D. B., Al-Saadi, J., Boersma, F., Bowman, K., Eldering, A., Fisher, B., and Jourdain, L.: Ozone production in boreal fire smoke plumes using observations from the Tropospheric Emission Spectrometer and the Ozone Monitoring Instrument, *Journal of Geophysical Research: Atmospheres*, 114, 2009.
- Wagner, T., Apituley, A., Beirle, S., Dörner, S., Friess, U., Remmers, J., and Shaiganfar, R.: Cloud detection and classification based on MAX-DOAS observations, *Atmospheric Measurement Techniques*, 7, 1289-1320, 2014.
- Wang, P., Holloway, T., Bindl, M., Harkey, M., and De Smedt, I.: Ambient Formaldehyde over the United States from Ground-Based (AQS) and Satellite (OMI) Observations, *Remote Sensing*, 14, 2191, <https://doi.org/10.3390/rs14092191>, 2022.
- Warneke, C., de Gouw, J. A., Edwards, P. M., Holloway, J. S., Gilman, J. B., Kuster, W. C., Graus, M., Atlas, E., Blake, D., Gentner, D. R., Goldstein, A. H., Harley, R. A., Alvarez, S., Rappenglueck, B., Trainer, M., and Parrish, D. D.: Photochemical aging of volatile organic compounds in the Los Angeles basin: Weekday-weekend effect, *Journal of Geophysical Research: Atmospheres*, 118, 5018-5028, <https://doi.org/10.1002/jgrd.50423>, 2013.
- Wennberg, P. O., Bates, K. H., Crounse, J. D., Dodson, L. G., McVay, R. C., Mertens, L. A., Nguyen, T. B., Praske, E., Schwantes, R. H., and Smarte, M. D.: Gas-phase reactions of isoprene and its major oxidation products, *Chemical reviews*, 118, 3337-3390, 2018.
- Wentworth, G. R., Aklilu, Y.-a., Landis, M. S., and Hsu, Y.-M.: Impacts of a large boreal wildfire on ground level atmospheric concentrations of PAHs, VOCs and ozone, *Atmospheric Environment*, 178, 19-30, 2018.

- Whitehill, A. R., Long, R., Kaushik, S., Szykman, J., Williams, D., Valin, L., Furdyna, P., and Felton, D.: Evaluation of Continuous Formaldehyde Measurements in Ambient Air, AGU Fall Meeting Abstracts, A33G-3207,
- Wisthaler, A., Apel, E., Bossmeyer, J., Hansel, A., Junkermann, W., Koppmann, R., Meier, R., Müller, K., Solomon, S., and Steinbrecher, R.: Intercomparison of formaldehyde measurements at the atmosphere simulation chamber SAPHIR, *Atmospheric Chemistry and Physics*, 8, 2189-2200, 2008.
- Wolfe, G. M., Nicely, J. M., St. Clair, J. M., Hanisco, T. F., Liao, J., Oman, L. D., Brune, W. B., Miller, D., Thames, A., and González Abad, G.: Mapping hydroxyl variability throughout the global remote troposphere via synthesis of airborne and satellite formaldehyde observations, *Proceedings of the National Academy of Sciences*, 116, 11171-11180, 2019.
- Wu, C. and Yu, J. Z.: Evaluation of linear regression techniques for atmospheric applications: the importance of appropriate weighting, *Atmospheric Measurement Techniques*, 11, 1233-1250, 2018.
- Wu, Y., Nehrir, A. R., Ren, X., Dickerson, R. R., Huang, J., Stratton, P. R., Gronoff, G., Kooi, S. A., Collins, J. E., and Berkoff, T. A.: Synergistic aircraft and ground observations of transported wildfire smoke and its impact on air quality in New York City during the summer 2018 LISTOS campaign, *Science of The Total Environment*, 773, 145030, <https://doi.org/10.1016/j.scitotenv.2021.145030>, 2021.
- Xu, L., Crouse, J. D., Vasquez, K. T., Allen, H., Wennberg, P. O., Bourgeois, I., Brown, S. S., Campuzano-Jost, P., Coggon, M. M., and Crawford, J. H.: Ozone chemistry in western US wildfire plumes, *Science Advances*, 7, eabl3648, 2021.

- Yang, J., Wen, Y., Wang, Y., Zhang, S., Pinto, J. P., Pennington, E. A., Wang, Z., Wu, Y., Sander, S. P., Jiang, J. H., Hao, J., Yung, Y. L., and Seinfeld, J. H.: From COVID-19 to future electrification: Assessing traffic impacts on air quality by a machine-learning model, *Proceedings of the National Academy of Sciences*, 118, e2102705118, 10.1073/pnas.2102705118, 2021.
- Yang, L. H., Jacob, D. J., Colombi, N. K., Zhai, S., Bates, K. H., Shah, V., Beaudry, E., Yantosca, R. M., Lin, H., and Brewer, J. F.: Tropospheric NO<sub>2</sub> vertical profiles over South Korea and their relation to oxidant chemistry: implications for geostationary satellite retrievals and the observation of NO<sub>2</sub> diurnal variation from space, *Atmospheric Chemistry and Physics*, 23, 2465-2481, 2023.
- Yokelson, R. J., Christian, T. J., Karl, T., and Guenther, A.: The tropical forest and fire emissions experiment: laboratory fire measurements and synthesis of campaign data, *Atmospheric Chemistry and Physics*, 8, 3509-3527, 2008.
- Yokelson, R. J., Goode, J. G., Ward, D. E., Susott, R. A., Babbitt, R. E., Wade, D. D., Bertschi, I., Griffith, D. W., and Hao, W. M.: Emissions of formaldehyde, acetic acid, methanol, and other trace gases from biomass fires in North Carolina measured by airborne Fourier transform infrared spectroscopy, *Journal of Geophysical Research: Atmospheres*, 104, 30109-30125, 1999.
- York, D., Evensen, N. M., Martínez, M. L., and De Basabe Delgado, J.: Unified equations for the slope, intercept, and standard errors of the best straight line, *American journal of physics*, 72, 367-375, 2004.

- Young, P. J., Naik, V., Fiore, A. M., Gaudel, A., Guo, J., Lin, M., Neu, J., Parrish, D., Rieder, H., and Schnell, J.: Tropospheric Ozone Assessment Report: Assessment of global-scale model performance for global and regional ozone distributions, variability, and trends, *Elem Sci Anth*, 6, 10, 2018.
- Zeng, P., Lyu, X., Guo, H., Cheng, H., Wang, Z., Liu, X., and Zhang, W.: Spatial variation of sources and photochemistry of formaldehyde in Wuhan, Central China, *Atmospheric Environment*, 214, 116826, <https://doi.org/10.1016/j.atmosenv.2019.116826>, 2019.
- Zhang, H., Li, J., Ying, Q., Guven, B. B., and Olaguer, E. P.: Source apportionment of formaldehyde during TexAQS 2006 using a source-oriented chemical transport model, *Journal of Geophysical Research: Atmospheres*, 118, 1525-1535, 2013.
- Zhao, X., Griffin, D., Fioletov, V., McLinden, C., Cede, A., Tiefengraber, M., Müller, M., Bogner, K., Strong, K., Boersma, F., Eskes, H., Davies, J., Ogyu, A., and Lee, S. C.: Assessment of the quality of TROPOMI high-spatial-resolution NO<sub>2</sub> data products in the Greater Toronto Area, *Atmos. Meas. Tech.*, 13, 2131-2159, [10.5194/amt-13-2131-2020](https://doi.org/10.5194/amt-13-2131-2020), 2020.
- Zhu, L., Mickley, L. J., Jacob, D. J., Marais, E. A., Sheng, J., Hu, L., Abad, G. G., and Chance, K.: Long-term (2005–2014) trends in formaldehyde (HCHO) columns across North America as seen by the OMI satellite instrument: Evidence of changing emissions of volatile organic compounds, *Geophysical Research Letters*, 44, 7079-7086, <https://doi.org/10.1002/2017GL073859>, 2017a.

- Zhu, L., Jacob, D. J., Mickley, L. J., Marais, E. A., Cohan, D. S., Yoshida, Y., Duncan, B. N., Abad, G. G., and Chance, K. V.: Anthropogenic emissions of highly reactive volatile organic compounds in eastern Texas inferred from oversampling of satellite (OMI) measurements of HCHO columns, *Environmental Research Letters*, 9, 114004, 10.1088/1748-9326/9/11/114004, 2014.
- Zhu, L., Jacob, D. J., Keutsch, F. N., Mickley, L. J., Scheffe, R., Strum, M., González Abad, G., Chance, K., Yang, K., and Rappenglück, B.: Formaldehyde (HCHO) as a hazardous air pollutant: Mapping surface air concentrations from satellite and inferring cancer risks in the United States, *Environmental Science & Technology*, 51, 5650-5657, 2017b.
- Zoogman, P., Liu, X., Suleiman, R., Pennington, W., Flittner, D., Al-Saadi, J., Hilton, B., Nicks, D., Newchurch, M., and Carr, J.: Tropospheric emissions: Monitoring of pollution (TEMPO), *Journal of Quantitative Spectroscopy and Radiative Transfer*, 186, 17-39, 2017.